Stop-Flow Lithography for Complex Particle Synthesis and Application in Directed Assembly

by

Priyadarshi Panda

B.Tech Chemical Engineering, Indian Institute of Technology, Kanpur (2006).

Submitted to the Department of Chemical Engineering
in partial fulfillment of the requirements for the degree of

Doctor of Philosophy in Chemical Engineering

at the

MASSACHUSETTS INSTITUTE OF TECHNOLOGY

September 2011
[February 2012]

Author_____
Department of Chemical Engineering
September 7, 2011

Certified by_____
Patrick S. Doyle
Professor of Chemical Engineering
Thesis Supervisor

Certified by_____
T. Alan Hatton
Ralph Landau Professor of Chemical Engineering
Thesis Supervisor

Accepted by_____
William M. Deen
Chairman, Department Committee on Graduate Students

Stop-Flow Lithography for Complex Particle Synthesis and Application in Directed Assembly

by
Priyadarshi Panda

Submitted to the Department of Chemical Engineering
on September 7, 2011, in partial fulfillment of the
requirements for the degree of
Doctor of Philosophy in Chemical Engineering

Abstract

The synthesis of complex microparticles is an important objective. These particles can find use in a number of applications ranging from tissue engineering to ceramics and assembly. Tuned assembly of anisotropic particles can give rise to macrostructures with complex morphologies. Externally applied fields like electric or magnetic fields are useful ways to tune the assembly of anisotropic particles. This thesis begins with an understanding of the flow conditions in stop-flow lithography (SFL), the technique used for anisotropic microparticle synthesis, followed by the demonstration of the versatility of SFL by synthesizing soft cell-laden microgels, hard ceramic microcomponents and 3D curved microparticles. The thesis ends with the study of the assembly of anisotropic magnetic hydrogels synthesized using SFL.

In the first section of the thesis, we introduce SFL and identify optimal conditions for particle synthesis using SFL. We do so by analyzing the dynamic response of a retracting PDMS wall after the removal of an external stress. We realized that for small deformations the problem lends itself to a regular perturbation analysis that is analytically solvable at zeroth-order. We compared the zeroth-order solution to the numerically solved full solution and to trends seen in experiments.

In the second section we demonstrate the ability to synthesize complex particles using SFL. We generated anisotropic cell-laden microgels with reasonable cell viability. This work required the use of careful, benign conditions to ensure good cell viability and precise stop of the flow to ensure good resolution of cell-laden hydrogels. We determined an optimal cell density in a mixture of the cell suspension with the oligomer and photoinitiator. Then, we varied the concentrations of the oligomer and photoinitiator in the mixture to achieve reasonable polymerization times while simultaneously ensuring the desired cell viability. In a different work, we demonstrated the ability to make colloidal glass and silicon microcomponents using SFL. We flew a shear thinning colloidal silica suspension mixed with oligomer and photoinitiator through a microchannel and flashed UV light through a photomask to synthesize polymeric microcomponents of desired shape. In order to enhance their structural integrity, these colloidal microgears were transformed into fully dense, glassy silica microparticles by sintering at 1150 °C for 3 - 10 hours. SFL has traditionally been used to synthesize 2D extruded particles. We demonstrated the ability to synthesize 3D curved particles using SFL by introducing curvature in the direction orthogonal to the projection of UV light. We achieved this by co-flowing two streams which we called the polymerization and tuning fluid respectively, through a microchannel. On stopping the fluids, curvature developed at the interface of the fluids to minimize the surface energy. The quiescent fluids were exposed to a flash of UV

light through a photomask which resulted in the gelling of the region within the polymerization fluid. The resulting microparticle had a shape in the plane of projection of light dictated by the mask and curvature in the plane orthogonal to the projection of light determined by the surface properties of the fluids used. The chemical programmability of this technique was demonstrated by synthesizing Janus, patched and capped polymeric microparticles.

In the final part of this thesis we present a framework for the study of the directed assembly of H-shaped magnetic hydrogels. We synthesized non-Brownian H-shaped microparticles with encapsulated nanometer sized magnetic beads for assembly studies. Directed assembly at low surface coverage involves two time steps: i) rotation to attain an equilibrium orientation, followed by ii) translation to form assembled structures. Hence, as a first step to understanding the assembly of these particles, we studied their rotation. We developed a Finite Element Integration (FEI) method to identify the preferred particle orientation (relative to the applied field) at different values of the geometric parameters defining H shapes and constructed a phase diagram to generalize the results. We validated the theoretical predictions by comparing with experiments performed using magnetic hydrogels synthesized using SFL. These results aided in the choice of H-shaped particles for further assembly studies wherein we demonstrated the ability of these particles to widen chains and induce branching orthogonal to the applied field.

Thesis Supervisor: Patrick S. Doyle
Title: Professor of Chemical Engineering

Thesis Supervisor: T. Alan Hatton
Title: Ralph Landau Professor of Chemical Engineering

Acknowledgments

A PhD thesis is a great learning experience, both intellectual and personal. My first and foremost thanks, to my thesis advisors Pat Doyle and Alan Hatton for their persistent guidance through the last 5 years which enriched my experience. I would like to thank Pat for constantly encouraging me to think deeper and harder on problems and presenting my ideas in a clear, concise manner. I am sure the thought process instilled in me due to my innumerable meetings with Pat will stand me in good stead for the rest of my life. I would like to thank Alan for his unwavering support and constant encouragement specially at times when things weren't running smoothly. I learnt a lot both from Alan's scientific advice and positive outlook under all circumstances. I would also like to thank my committee members - Francesco Stellacci and specially Michael Strano for constant advice and helpful comments in all my meetings. In particular, I would like to thank Michael for his support and having an open door whenever I needed help.

I would like to thank both the Doyle and Hatton group members for their help in conducting scientific experiments and for useful discussions which helped in improving my research. In particular I would like to thank Dhananjay Dendukuri from the Doyle group for teaching me the basics of stop-flow lithography and for useful advice during my early years in the group. Anthony Balducci, Ramin Haghgooie and Daniel Trahan for always being there to answer my questions. Dan Pregibon for constantly coming up with creative solutions to many problems I sought help with. Ki Wan Bong for help with synthesis and cleaning of magnetic hydrogels, discussions on new projects and many memorable chats. Matt Helgeson for useful discussions on the field-directed assembly work.

Su Kyung Suh for useful discussions on magnetic particle cleaning. Steve Chapin, Jason Rich and William Uspal for making my time in the lab fun. Smeet Deshmukh and Saurabh Tejwani for help with experiments in the Hatton group and for introducing me to some delectable Indian food in Cambridge. Lev Bromberg for useful discussions on chemicals to be used in different projects and advice on surface tension experiments. Samsher Ali and Edward Lo from the Khademhosseini lab at the Harvard-MIT Division of Health Sciences and Technology for help with the cell encapsulation work. Rob Shepherd from the Lewis lab at the University of Illinois at Urbana-Champaign for help with the work on ceramic microcomponents. Murat Ocalan from the McKinley lab for helping me borrow his electromagnetic set-up and for useful discussions. Kai Yuet my UROP for help with two projects and willingness to work late nights when need be.

On a personal front, I would like to thank all my friends for their constant support during these long 5 years. My special thanks to Amit Soni, Abhinav Aggarwal and Sashi Mittal for being amazing suite-mates for my first few years and always being there for fun outings, be it food, movies or trips. Abhinav Akhoury and Diwakar Shukla for amazing lunch discussions and time spent at Indian events at MIT. Andres Abin-Fuentes for fun times spent playing tennis and soccer and watching the Celtics and for introducing me to good Mexican food around Cambridge and Boston.

Last but not the least; I would like to thank my family for constantly egging me on. Without the blessings of my parents (Baikunthnath Panda and Sabitri Panda), I would not have been able to get to this point. Finally, my brother (Sabyasachi Panda) for encouraging words, guidance and sense of humor through the last 5 years.

Table of Contents

List of Figures

List of Tables

CHAPTER 1

Introduction

1.1 Motivation

The stabilization of colloidal particles was observed in the early 1900s by Pickering [1]. Ever since that discovery, the assembly of colloidal particles, both at the interface of liquids and in the bulk of solvents has been widely researched. Most of the studies carried out involve spherical particles due to their ease of synthesis and the isotropic nature of the forces involved in their assembly. The assembly of spherical particles leads to simple geometries such as face-centered cubic, hexagonal closed-packed and body centered cubic and does not provide parameters to tune their assembly into desired packing configurations. The assembly of particles with different shapes and chemistries would give more parameters to tune and allow for complex structures to be formed from their packing. With the advent of new methods of generating complex particles of different shapes and anisotropies, the limiting factor has now shifted to the imagination of scientists to envision materials that can be built for different applications. A nice review on this topic has been written by Glotzer and Solomon [2]. Their work provides a conceptual framework, however the ideas presented have not been explored in depth. Furthermore, a basic understanding of the driving factors for the assembly of complex particles and hence the ability to predict the packing of these particles in any solvent is lacking. Dispersions of colloidal particles of different shapes are essential for the evaluation of the optical, magnetic, electrokinetic, or adsorptive properties of colloidal matter as well as the theoretical interpretation of the interactions that involve such particles. Moreover, colloidal crystals formed from the assembly of colloidal particles in bulk solutions, can be used to

explore diverse phenomena such as crystal growth and the glass transition behavior and have many interesting applications for sensors, in catalysis, in advanced coatings and for optical/electrooptical devices for information processing and storage. These diverse applications necessitate the high throughput synthesis of monodisperse particles.

1.2 Background

This section discusses the work that has been done for the generation of complex colloidal particles and their assembly into macrostructures. The development of microfluidics in general and stop-flow lithography (SFL) in particular for the generation of complex microparticles will also be discussed.

1.2.1 Microparticles: The Atoms and Molecules for Next Generation Material Synthsis

In recent years, the realization has set in that anisotropic shape and interactions through chemical patchiness are powerful tools for engineering the assembly of particular targeted structures. The anisotropy of new building blocks starkly contrasts with the isotropic spherical colloids that have been the focus of particle assembly for nearly a generation. The addition of shape and interaction anisotropy to particles extends the possible assemblies to motifs potentially as complex as those seen in molecular crystals. At present, a general predictable relationship between anisotropic building-block structure and the structure and symmetry of ordered arrays produced from these building blocks is not in hand, but colloidal assembly is governed by the same thermodynamics that produces ordered equilibrium structures in systems of atoms and molecules. In fact, molecular analogues such as liquid crystals, surfactant and block copolymers exhibit diverse building-block anisotropy and can act as model systems for the synthesis of complex colloidal particles. Thus, if non-idealities peculiar to the assembly of colloidal particles such as jamming and gelation are avoided, anisotropic colloidal particles ought to assemble into morphologies as diverse as those of molecules. Analogies can be drawn between the assembly of colloidal particles and atomic and molecular packings in crystals, assembly of surfactants and block copolymers and molecular liquid crystal mesogens in liquid crystals. First let us consider the analogy with crystallography. In the case of atomic packings, a suite of highly symmetric near-closed-packed structures that balance the constraints of atomic size and charge neutrality dominate. This motif seems to hold in the colloidal scale as well [3, 4, 5]. In addition, unlike atoms, colloidal particles have continuously tunable size and charge and thus, ionic crystals with no known atomic or molecular analogues have been discovered [3, 6, 7]. Addition of directionality to these colloidal particle assemblies can lead to the formation of more open structures such as diamond and anisotropic such as graphite. Directionality can be introduced into interactions between colloidal particle by patchiness [8] which can be achieved through selective sintering, hybridization by DNA oligomers, proteins or organic tethers, and other means. Second, similarities can be drawn between the assembly of Janus colloidal particles and that of amphiphilic particles like surfactants and block copolymers. Phase-diagram formalisms developed to understand surfactant and copolymer systems may be applied to colloids exploiting the particle colloid analogy. An interesting complication is the effect of structural rigidity (packing effects) in these particle-based amphiphiles and is probably a generic difference between molecular and colloidal systems. This difference probably requires modification of quantities used to characterize ordered phases. Simulations carried out recently have shown commonalities and

differences between copolymer and amphiphilic colloid diagrams [9], but as colloids become more complex in their anisotropy wholly new phases are expected. Further, as in molecular systems, anisotropic long range interactions between particles that extend over multiple particle diameters may be exploited to generate unique assemblies [10]. Third, anisotropic colloidal particles are similar to liquid crystal mesogens. Recent work has shown the existence of nematic- and smectic-type phases in colloids. Simulations carried out have shown the possibility of newer crystalline phases for instance nanocolloidal cubes are predicted to form a cubatic phase that has liquid-crystalline character [11]. The above ideas help us envision complex colloidal particles as the atoms and molecules for future material synthesis. These novel materials can find application in a wide variety of fields ranging from catalysis to photonic crystals and drug delivery systems.

1.2.2 Complexity in Available Particles and Characterization

The realization that complex particles can be used for engineering targeted structures fuelled the synthesis of an unprecedented diverse spectrum of particle anisotropy, including nanocolloidal cubes [12, 13] and icosahedra [14], triangle [15], tetrahedra [16], prisms [17, 18], Janus particles [19, 20], half shells [21], stripped particles [22], rods, arrows and tetrapods [23], tripods [24], stars [25] and polyvalent spheres and many other exotic shapes as shown in Figure 1.1.

In order to understand the assembly of these particles into complex structures, a theoretical description of these particles, i.e. a classification scheme, is necessary. At present, even a common language or general classification scheme is lacking for describing these building blocks or their assemblies though some attempts have been made recently. The development of terminologies and taxonomies will provide critical guidance for materials fabrication by establishing the common ground needed for consensus about architecture and phenomenology. Such a unifying language is lacking for colloidal particles yet their complexity demands a unifying description to exploit similarities and discern differences. Solomon and Glotzer at the University of Michigan have come up with a scheme wherein key parameters describing the various anisotropies of a building block are conceptualized as dimensions. Moving along an anisotropy axis leads to a continuous or discrete tuning of that property. Any particle can then be assigned a dimensionality corresponding to the orthogonal anisotropy dimensions needed for its description and maybe further classified by those dimensions. The complexity of a particle would then be given by the dimensionality of the particle in the anisotropy space and it can be characterized and predictions made about its assembly into macrostructures by the anisotropy dimensions. An example of dividing the anisotropy space into anisotropy axes is shown in Figure 1.2. This list is not exhaustive though.

The important question here is that could these commonalities indicate similar expected phase behavior? The claim made by Solomon and Glotzer is that virtually any particle may be resolved into a combination of a finite number of key orthogonal anisotropy dimensions relevant for its subsequent assembly into macrostructures. As an example, let us consider the two tetrapods in the top row in Figure 1.1. The key anisotropy dimension for the tetrapods is branching (axis E). The tetrapods can also be differentiated on the basis of aspect ratio (axis B) because the tetrapod on the left which resembles a plus sign can be roughly circumscribed by a disc, whereas the tetrapod on the right is circumscribed by a sphere. Thus, the two tetrapods have a dimensionality of 2 in anisotropy space. This analysis is simple but, can be extended to more refined descriptions of various types of anisotropy. The claim however, is that a limited set of key dimensions is sufficient to allow experiment, theory and simulation to fruitfully interact to explore the potential for anisotropic

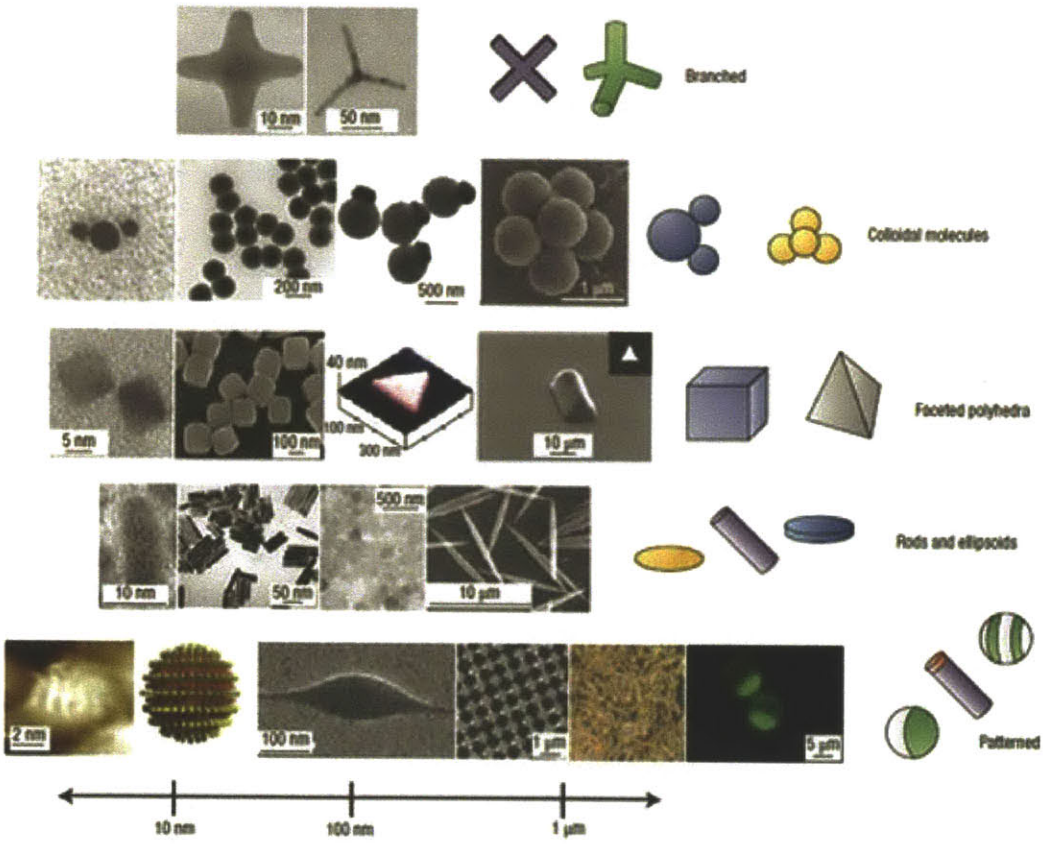

Fig. 1.1: *Representative examples of anisotropic particle building blocks, synthesized by the plethora of new techniques available. Particle size increases from left to right as per the approximate scale at bottom. From left to right, top to bottom: branched particles include gold and CdTe tetrapods. DNA linked gold nanocrystals and silica dumbbells are some examples of colloidal molecules. Gold and polymer triangular prisms are some examples of faceted particles. Similarly, striped spheres, biphasic rods and Janus spheres are some examples of patterned particles. Figure adapted from* **Glotzer et al.**, *Nat. Mater., 2007.*

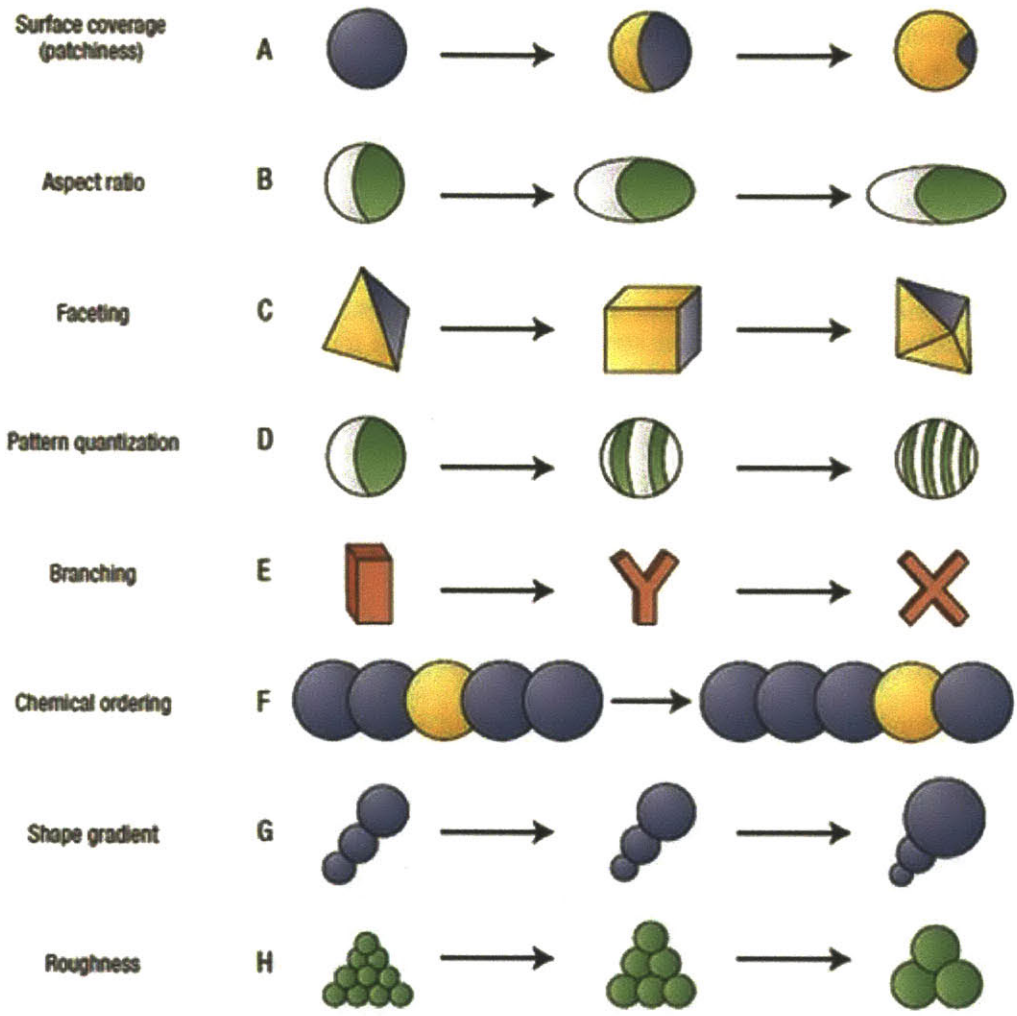

Fig. 1.2: *Anisotropy axes used to characterize particles. Particles corresponding to the changes in anisotropy axis. (A) Interaction patchiness via surface coverage; (B) Aspect ratio; (C) Faceting; (D) Interaction patchiness via surface pattern quantization; (E) Branching; (F) Chemical ordering; (G) Shape gradient; (H) Roughness. Figure adapted from* **Glotzer et al.**, *Nat. Mater., 2007.*

particles design and assembly.

1.2.3 Approach to Materials Design from Complex Particles

The development of complex particles, their characterization into anisotropic axes and their subsequent study to determine the interplay between the various sets of anisotropy dimensions will help us carry out a systematic investigation of how symmetries of the bulk assembly vary as we move along each of the axes independently. This would benefit the rational design of materials. The ultimate aim is to generate phase diagrams which would predict the self assembled structures possible from building blocks of any given anisotropy. These diagrams would demonstrate explicitly how combinations of anisotropy attributes affect bulk structure for a given set of thermodynamic conditions. The aforementioned approach is a forward approach to the synthesis of assembled structures from complex colloidal particles. There is a different approach possible which is referred to as reverse engineering wherein a target structure is envisioned for some application and a prediction of the particle shape and size required to assemble into the target structure is made based on the phase diagrams. For example, imagine a crystal structure, the diamond lattice ordering for optical applications for instance. One way to think about generating this structure is via particles which mimic a carbon atom in its bonding arrangement. Mohwald and co-workers [26] made colloidal spheres with valence four achieved through the judicious placement of four sticky patches [27]. A combination of forward and reverse engineering would eventually lead to the ability to generate materials of complex architecture.

1.2.4 Existing Technologies for Complex Particle Synthesis

The need to generate complex particles which would act as the atoms and molecules for future materials fuelled the discovery of new chemical, physical and biosynthetic methods for the purpose. Chemical methods developed include selective crystallization and deposition [12, 13, 23, 28]. Physical methods include electrified jetting, microcontact printing, emulsion drying, selective deposition, surface templating, direct writing and lithography [19, 29, 30, 31, 32, 33, 34]. Biologically inspired methods include the use of plant extracts [18], fungi [35] and viruses [36] to synthesize building blocks of various shapes. Lithography is a physical method for the generation of colloidal particles which has been used extensively in the past. It is however a batch process which limits the throughput. Microfluidic techniques for particle synthesis were developed for the continuous synthesis of colloidal particles [37, 38, 39, 40, 41, 42, 43, 44, 45, 46, 47]. Several groups have used multi-phase microflows to produce microparticles and capsules. Surface tension limits these particles to be spheroids. The Doyle group recently showed that more complex shapes and also patterned chemistries within a particle can be attained by coupling microfluidics to photolithography. The technique was called CFL [30] which was refined to develop SFL [48] to increase the throughput and attain greater control over shape and size. SFL essentially consists of three steps, stop (stopping the flow of polymer solution), polymerize (flash of UV light through a photomask) and flow (flowing out of microparticles using a pressure pulse). A schematic of SFL for the generation of Janus particles is shown in Figure 1.3. The system for generation of single chemistry particles would involve the flow of a single stream in place of the co-flow. The above techniques (CFL and SFL) allow the synthesis of 2-D extruded particles of any desired shape as shown in Figure 1.3 at high enough throughputs to envision a study on the characteristics of their assembly.

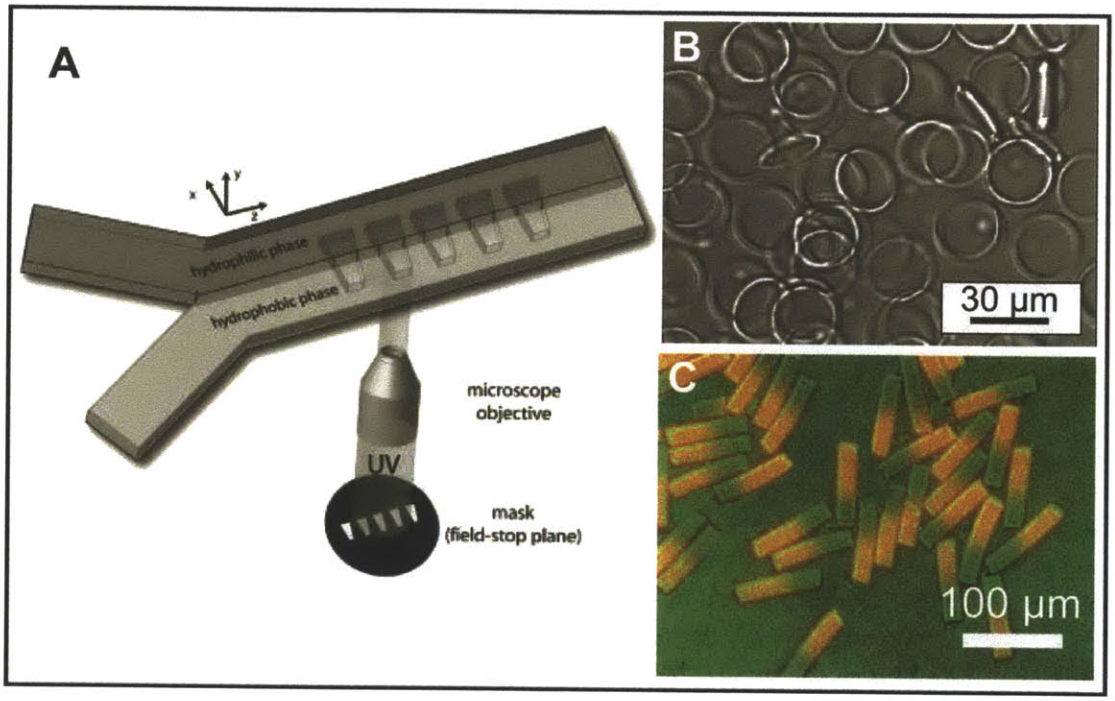

Fig. 1.3: *A) Co-flow of streams in a microchannel for Janus particle synthesis using SFL. Collection of particles generated using CFL. B) Single chemistry and C) Janus. Figure adapted from* **Dendukuri et al.**, *Nat. Mater., 2006 and* **Dendukuri et al.**, *Langmuir, 2007.*

1.3 Objectives

The goal of this research is to obtain an understanding of the flow conditions in SFL (polymeric microparticle synthesis platform used in this thesis) and to demonstrate its versatility as a particle synthesis technique in both the kind of oligomeric fluids that can be used as well as the conditions of synthesis. Further, we want to demonstrate the use of monodisperse particles synthesized using SFL for assembly into complex morphologies. The following studies will be presented:

- Temporal response of an initially deflected PDMS microchannel (**Panda et al.**, New J. Phys., 2009);
- Synthesis of soft cell-laden microgels (**Panda et al.**, Lab Chip, 2008);
- Synthesis of hard ceramic microcomponents (**Shepherd and Panda et al.**, Adv. Mater., 2008);
- Synthesis of curved microparticles with curvature in a direction orthogonal to the UV light (**Panda et al.**, Langmuir, 2009);
- Synthesis and assembly of H-shaped magnetic microgels (**Panda et al.**, Langmuir, submitted);

1.4 Overview of Results

In Chapter 2, we analyze the dynamic behavior of a retracting PDMS wall after removal of an external stress. This chapter helps understand the flow in PDMS microchannels used in SFL. In Chapter 3 we demostrate the ability to generate soft cell-laden microgels using SFL. This chapter demonstrates the ability to provide benign polymerization conditions using SFL which helps ensure good cell viability. In Chapter 4 we demonstrate the flexibility of SFL in handling non-Newtonian solutions to generate hard particles. We use index matched shear thinning colloidal silica solution mixed with oligomer and photoinitiator to generate silica encapsulated polymeric microcomponents. These particles are then sintered to generate porous and dense silica and silicon particles. In Chapter 5 we demostrate the ability to make 3D curved particles having curvature orthogonal to UV light, using SFL. This capability enhances the range of particles that can be synthesized using SFL. We demonstrate the programmability of this added feature by synthesizing Janus, patched and capped microparticles. In Chapeter 6, we study the rotation and assembly of non-Brownian H-shaped magnetic particles in a uniform magnetic field. We develop a Finite Element Integration (FEI) method to identify the preferred particle orientation (relative to the applied magnetic field) at different values of the geometric parameters defining H shapes, and compare the results with experiements performed using magnetic H-shaped microparticles synthesized using SFL. Furthermore, we study the assembly of H-shaped particles chosen so as to have a high propensity to form wide networks orthogonal to the directon of the apllied field. The assembly of these particles is compared to the assembly of rods and to a mixture of these particles with rods at a low surface coverage. Finally in Chapter 7 the results of our research are briefly summarized and their impact assessed. We also discuss future work that can build on the studies presented in this thesis in this chapter.

CHAPTER 2

Temporal Response of an Initially Deflected PDMS Channel

This chapter presents the study carried out to understand the flow conditions in stop-flow lithography (SFL), the microparticle synthesis platform used for this reserach. Specifically, we investigated the dynamic response of a PDMS channel after the removal of an external stress through both theoretical and experimental methods. We were able to derive analytical expressions for a priori predictions for the time required for the flow to stop. We verified that at low deflections, the analytical solution is a close match to the numerically solved full solution. Through new and previously published experiments, we were able to verify the validity of the analytical solution. My sincere thanks to Kai P. Yuet, the undergraduate student working with me on this project, for help with experiments and coding using MATLAB.

2.1 Overview

Microfluidics is used in a wide array of applications including photonics, catalysis, optoelectronics, particle synthesis, bio-diagnosis and tissue engineering. Poly(dimethyl) siloxane (PDMS) is one of the most widely used materials for the fabrication of microfluidic devices. In many applications, applied flow gives rise to pressure variations along the length of the channel and a commensurate spatially varying channel height. We have previously performed a scaling analysis of the dynamics of PDMS deformation for small deformations (Reference: [48]). The prior study did not consider the dynamic evolution of the initially deflected channel and, being a scaling theory, required a fitting parameter for *a priori* predictions. In this chapter, we analyze the dynamic behavior of a retracting PDMS wall after the removal of an external stress. For small deflections, the problem lends itself to a regular perturbation analysis that is analytically solvable at zeroth-order. We find that the zeroth-order solution is very close to the numerically solved full solution for most situations of experimental interest. We further demonstrate that our model captures both qualitative and quantitative trends seen in the prior [48] and newly performed experiments.

2.2 Introduction

The field of microfluidics has grown exponentially over the past decade, driven by the notion that miniaturization of processes leads to distinct advantages in diverse fields such as biological separations, synthetic chemistry and combinatorial screening. While devices on the micron scale can be constructed using 'hard' materials like silicon, the rapid growth of microfluidics has been driven by replica molding technologies which enable the cheap and fast fabrication of disposable plastic devices. Poly(dimethyl) siloxane (PDMS) has become one of the most widely used materials in such technologies because of its high fidelity, low surface energy, transparency, porosity and conductivity among other qualities.

Among the properties of PDMS which may or may not be useful, depending on the intended application, is its low bulk modulus (in the range of 0.5 - 4 MPa) [49, 50] which leads to deformation under external pressure. This deformation has been cleverly exploited to synthesize valves [51] and microlenses [52]. Flow in deforming channels has also been used to model cardiovascular flow behavior [53, 54, 55]. PDMS deformation is, however, undesirable in applications where wall rigidity is essential, causing sagging of channels [56], increasing Taylor dispersion and diverging from predictions of flow profiles and mass transfer that have been made for rectangular cross-sections. In pressure-driven flows, low aspect ratio channels will have a tendency to bulge and thus any microfluidic application that requires a precise knowledge of the flow profile, pressure and channel geometry [57] will be compromised if the actual channel deformation cannot be quantified and taken into account. Some common microfluidic applications which are dependent upon the channel deformation are shear-flow assays (cellular or protein) [58, 59] and surface plasmon resonance (SPR) sensing technology [60, 61]. Deformation of PDMS channels can also affect fluorescence intensity signals, which depend on the absorption path length across the channel, thus biasing measurements if deformation is not taken into account. The synthesis of monodisperse particles using microfluidic devices [62] also depends on an accurate prediction of the deformation profile of PDMS.

In a previous work [48], we have analyzed the dynamic behavior of PDMS under external pressure by using a simple scaling argument. While this prior work gives insight into how the relaxation of the system scales with the fluid properties and channel dimensions, it does not give *a priori* pre-

dictions for the absolute values for the relaxation times nor does it provide information about the local temporal response of the system. For example, the scaling theory does not show that transient flow reversal occurs in a portion of the channel. Moreover, previous work on the deformation of PDMS channels has depended on simulations to make predictions of channel deformations, pressure distribution and flow profiles. The purpose of the current work is to develop a more comprehensive analysis of the dynamics of a deforming PDMS microfluidic channel and use a perturbation analysis to provide analytical expressions to describe the dynamic response. The theory will be compared to existing and new experimental data.

2.3 Theory

We begin with the equation for channel height as a function of time and space which has been derived earlier [48]

$$\frac{\partial h}{\partial t} = \frac{h^2 E}{4\mu W}\left[\left(\frac{\partial h}{\partial x}\right)^2 + \frac{h}{3}\frac{\partial^2 h}{\partial x^2}\right]. \tag{2.1}$$

In the above equation, x represents the direction of flow, t is the time, h is the height of the channel at any position and time, E is the Young's modulus of PDMS, W is the width of the channel and μ is the viscosity of the Newtonian fluid flowing through the channel. This equation is valid for small deformations in the range where the linear stress-strain relation of PDMS is valid i.e., $\varepsilon < 0.25$. ε is the maximum deformation scaled by the relaxed channel height. An illustration of the initial deformation on application of the pressure pulse is shown in Figure 2.1a. We now rewrite this equation in terms of the deformation of the channel ($\Delta h(x,t)$) using $h(x,t) = H + \Delta h(x,t)$ where H is the undeformed height of the channel and $\Delta h(x,t)$ is the deformation of the channel

$$\frac{\partial(\Delta h)}{\partial t} = \frac{(H+\Delta h)^2 E}{4\mu W}\left[\left(\frac{\partial(\Delta h)}{\partial x}\right)^2 + \frac{(H+\Delta h)}{3}\frac{\partial^2(\Delta h)}{\partial x^2}\right]. \tag{2.2}$$

The dependent variable in the problem is now the extent of deformation of the channel, $\Delta h(x,t)$. The initial condition for the problem is the steady state value of channel deformation and can be calculated from earlier work [50]

$$\Delta h(x, t=0) = H\left\{\left[\left(\left(\frac{L-x}{L}\right)\left[\left(1+\frac{P_{in}W}{EH}\right)^4 - 1\right]\right) + 1\right]^{1/4} - 1\right\}. \tag{2.3}$$

Here P_{in} is the gauge pressure (pressure above the atmospheric pressure) at the inlet of the device where the channel deformation is initially at its highest value ($H + \Delta h_{max}$ where $\Delta h_{max} = P_{in}W/E$) and L is the length of the channel. The boundary conditions are given by

$$\Delta h(x=0,t) = 0, \quad \Delta h(x=L,t) = 0. \tag{2.4}$$

Nondimensionalizing Equations 6.2, A.4 and 2.4 using

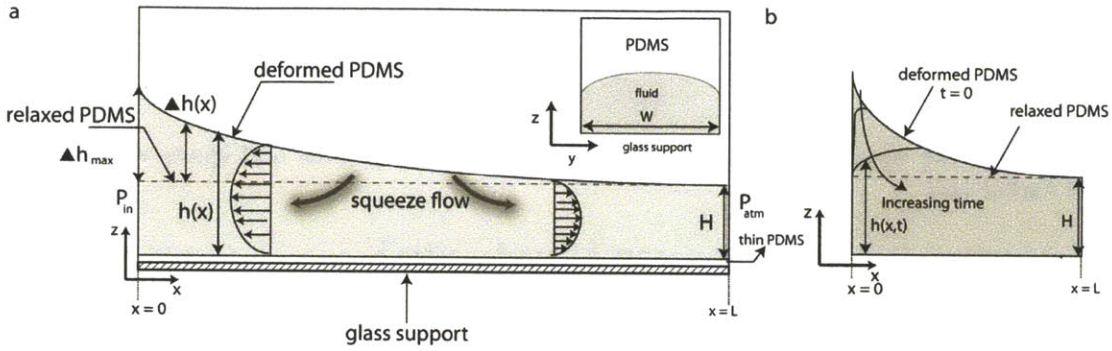

Fig. 2.1: *(a) Schematic showing the deformation of the PDMS microchannel (shown in white) at initial times ($t = 0$). The flow of the monomer (grey) is initially from left to right, the pressure being highest at the entrance (maximum PDMS deformation) and reaching atmospheric pressure at the outlet (minimum PDMS deformation). The figure is a 2-dimensional representation of the channel where the height shown at any point, $h(x)$, has been averaged across the width of the channel (the y-dimension). The inset on the top right of the figure, shows a cross-sectional view of the channel which depicts the variation in height across the width of the channel. The deformed PDMS channel relaxes back to its original state, shown as a dashed line (original height of the channel), when the pressure is turned off. This relaxation causes an asymmetric squeeze flow that drives monomer out to the left and the right. The bottom of the device is undeformed because rigid glass slide that supports it has a high Young's modulus. (b) The temporal evolution of the profile is shown for three different values of time.*

$$\theta = \frac{\Delta h}{P_{in}W/E}$$
$$\tau = \frac{t}{4\mu W L^2/EH^3}$$
$$\eta = \frac{x}{L}$$

we arrive at

$$\frac{\partial \theta}{\partial \tau} = (1+\varepsilon\theta)^2 \left[\varepsilon \left(\frac{\partial \theta}{\partial \eta} \right)^2 + \frac{(1+\varepsilon\theta)}{3} \frac{\partial^2 \theta}{\partial \eta^2} \right] \tag{2.5}$$

with the boundary and initial conditions given by

$$\theta(\eta = 0, \tau) = 0 \tag{2.6}$$
$$\theta(\eta = 1, \tau) = 0 \tag{2.7}$$
$$\theta(\eta, \tau = 0) = \frac{1}{\varepsilon} \left\{ \left[\left((1-\eta) \left[(1+\varepsilon)^4 - 1 \right] \right) + 1 \right]^{1/4} - 1 \right\} \tag{2.8}$$

where ε is defined as

$$\varepsilon = \frac{P_{in}W}{EH} = \frac{\Delta h_{max}}{H} \tag{2.9}$$

and is the maximum deformation in the channel scaled by the channel height. For deformations which are small compared to the channel height, $\varepsilon \ll 1$ we can solve Equation A.6 using a regular perturbation approach by expanding

$$\theta = \theta_0 + \varepsilon\theta_1 + O(\varepsilon^2). \tag{2.10}$$

The zeroth order problem governing θ_0 is obtained by setting $\varepsilon = 0$ in the original equations to give

$$\frac{\partial \theta_0}{\partial \tau} = \frac{1}{3} \frac{\partial^2 \theta_0}{\partial \eta^2} \tag{2.11}$$

$$\theta_0(0, \tau) = 0, \quad \theta_0(1, \tau) = 0, \quad \theta_0(\eta, 0) = 1 - \eta. \tag{2.12}$$

The solution to Equation 2.11 with boundary conditions specified in Equation 2.12 is obtained using finite fourier transforms (FFT) [63] and is given by

$$\theta = \sum_{n=1}^{\infty} \frac{2(e^{-n^2\pi^2\tau/3}) sin(n\pi\eta)}{n\pi}. \tag{2.13}$$

The higher order perturbation equations can not be solved analytically and thus we stop here with

the zero order solution and will present a full numerical solution later in the chapter.

The nondimensionalized pressure ($\P = P/P_{in}$) is related to the deformation of the channel by [48]

$$\frac{\partial \P}{\partial \eta} = \frac{\partial \theta}{\partial \eta}. \tag{2.14}$$

The zeroth-order solution for the nondimensionalized pressure is given by

$$\P = \frac{P_{atm}}{P_{in}} + \sum_{n=1}^{\infty} \frac{2(e^{-n^2\pi^2\tau/3})sin(n\pi\eta)}{n\pi}. \tag{2.15}$$

From our previous work [48], the velocity in the x direction is given by

$$v_x = \frac{E}{2\mu W}\frac{\partial h}{\partial x}(z^2 - zh(x)). \tag{2.16}$$

The velocity at $z=H/2$ is given by

$$v_x(H/2) = \frac{-EH^2}{8\mu W}\frac{\partial \Delta h}{\partial x}\left[1 + 2\frac{\Delta h}{H}\right]. \tag{2.17}$$

Nondimensionalising Equation 2.17 using

$$V_x(H/2) = \frac{v_x(H/2)}{P_{in}H^2/8\mu L} \tag{2.18}$$

we obtain

$$V_x(H/2) = \frac{-\partial \theta}{\partial \eta}[1 + 2\theta\varepsilon]. \tag{2.19}$$

At small deformations, the second term in the bracket in Equation 2.19 can be neglected and the nondimensionalized centerline velocity using Equations 2.13 and 2.19 is given by

$$V_x(H/2) = \frac{-\partial \theta}{\partial \eta} = -\sum_{n=1}^{\infty} 2(e^{-n^2\pi^2\tau/3})cos(n\pi\eta). \tag{2.20}$$

Now, using Equations 2.12 and 2.20, the initial steady state nondimensionalized velocity is 1 for the zeroth order solution. For the velocity predictions from the full solution, we are only concerned with the intial centerline velocity at the exit, which was derived in an earlier work [48] and can be nondimensionalized to obtain

$$V_x(H/2, L, \tau = 0) = \frac{(1+\varepsilon)^4 - 1}{4\varepsilon}. \tag{2.21}$$

The above expression can also be derived using Equations 1.7, 1.8 and 2.19. We have a squeeze flow problem wherein, at all $\eta < 0.5$, the velocity changes direction from towards the exit (positive) to towards the inlet (negative). Therefore, the response time (κ) is defined as the time required for the velocity to reduce to 0.01 (1 % of the initial steady state value), for $\eta > 0.5$ and -0.01, for $\eta < 0.5$. The nondimensionalized response time (λ) is given by

$$\lambda = \frac{\kappa}{4\mu WL^2/EH^3}. \tag{2.22}$$

For large values of η and τ, $n = 1$ is the dominating term in the FFT. Using the expression for $V_x(H/2)$ in Equation 2.20, the time required for the deformation to reduce to c % of its initial value as $\eta \rightarrow 1$ is given by

$$\lambda = -3\frac{ln(c/200)}{\pi^2}. \tag{2.23}$$

Finally, the position of the stagnation point (η_s) can be found by solving $\partial\theta/\partial\eta(\eta_s) = 0$. The stagnation point is the position along the length in the channel where the velocity of the fluid in the x direction is zero. For experimental validation, the nondimensionalized time (α) for the stagnation point to reach any $\eta < 0.5$ is used. α at any η is defined as the nondimensionalized time at which $\partial\theta/\partial\eta = 0.01$, to be consistent with the

2.4 Modeling and Experimental Methods

2.4.1 Zeroth-order and Full Solution

The zeroth-order problem (Equation 2.11) is solved analytically using Finite Fourier Transform (FFT). The solution to the zeroth-order problem given in Equation 2.13 and for the velocity given in Equation 2.20 was truncated at five terms (the contribution of the sixth term is less than 1 % of the sum of five terms). We solved the ful problem (Equation A.6) using the PDE solver in MATLAB, to obtain θ as a function of η and τ. This solution for θ was used to obtain the velocity from the full solution.

2.4.2 Microfluidic Devices

Microfluidic devices were made by pouring poly(dimethyl) siloxane (PDMS, Sylgard 184, Dow Corning) on a silicon wafer containing positive-relief channels patterned in SU-8 photoresist (Microchem) using polymer and curing agent in a ratio 10:1. The thickness of the PDMS devices was always maintained to be 5 mm. Straight channels with a rectangular cross-section and variable widths, lengths and heights were used as reported in Table 2.1. Video recordings of bead flow were recorded at 30 frames/s onto a videotape recorder (DSR-25, Sony) for processing.

2.4.3 Materials

In all experiments involving PEG-DA, a 1 % solution of 1.57 μm PMMA beads in poly(ethylene glycol) (400) diacrylate (PEG-DA, Sigma Aldrich) was used. In experiments involving TMPTA and TMPTA esters, a 1 % solution of 1.5 μm Fluoresbrite carboxylate beads (Polysciences) in tri(methylol propane) triacrylate (TMPTA, Polysciences) or ethoxylated trimethylolpropane triacryalte esters (TMPTA esters, Sartomer) was used. PEG-DA, TMPTA and TMPTA esters have been reported by the manufacturers to have viscosities of 56, 106 and 230 cP respectively, at 25 °C. The linear stress-strain regime of PDMS was found to be valid for $\varepsilon < 0.25$ using dynamic mechanical analysis carried out using a DMA Q800 from TA instruments. The elastic modulus of PDMS, in the linear stress-strain regime was found to be 2 MPa by the same experiment.

L (μm)	W (μm)	H (μm)	ε
10000	50	20	0.026
10000	200	40	0.052
10000	200	20	0.103
2300	200	10	0.207
5000	200	10	0.207
10000	200	10	0.207
10000	500	20	0.259

Table 2.1: *Table showing the dimensions of the microfluidic devices used for the bead tracking experiments using PEG-DA, TMPTA and TMPTA esters. For experiments using PEG-DA all channel dimensions in the table were used whereas for TMPTA and TMPTA esters, 200 μm wide channels with two different lengths (L = 5000 μm and 10000 μm) and two different heights (H = 10 μm and 20 μm) were used. The value of ε for each of the conditions using E = 2.0 MPa and P_{in} = 3 psi is also shown. The experimental response times at the exit of the channel for PEG-DA, have been taken from previously published results (***Dendukuri et al.**, Lab Chip, 2007).*

2.4.4 Bead Tracking

A dilute solution of beads (see Materials section) was used to track the squeeze flow in the PDMS device [48]. A repeating square wave pressure profile comprising two parts - 1 s of applied pressure and 2 s of turning the pressure off was applied to the system. The beads in the mid-plane of the channel ($z = H/2$) were followed with a 20× or 40× microscope objective (Zeiss) with an optivar setting of 2.5× leading to effective magnifications of 50× and 100× respectively. Movies of the beads were recorded using a video tape recorder (DSR-25, Sony) using a CCD camera that captured images at the rate of 30 frames/s using an exposure of 1/1500 s. The frame-to-frame position of beads was measured as they moved across the screen using macros set up in NIH image. The displacement of the beads, evaluated using the forward difference approximation gave the velocity. All bead tracking experiments were performed at a pressure of 3 psi. The bead tracking experiments at the exit of the channel were performed using PEG-DA, TMPTA and TMPTA esters for the channel dimensions reported in Table 2.1. The bead tracking experiments at different positions along the channel were performed for channels having a height of 10 μm or 20 μm and length and width of 1 cm and 200 μm respectively. Wall effects were avoided by choosing beads close to the center of the channel ($y = W/2$).

2.5 Results and Discussion

The PDMS channel deforms on the application of a pressure pulse as shown in Figure 2.1a. The deflected PDMS channel then relaxes back to its undeformed state after the pressure pulse has been turned off as shown in Figure 2.1b. In microfluidic devices fluid flows are commonly driven using

syringe pumps. These devices compress the fluid in the tubing external to the microfluidic device, causing transients that can be several minutes or longer for micron-scale systems [64]. A rapid dynamic response is desired [64, 65]. Therefore, we use air driven flows in our experiments using the SFL setup, which lead to finite transients associated with the deformation of the PDMS device. The channel dimensions used for this work lead to deformations ranging from $\sim$ 300 nm to 3 μm. Measuring these deformations accurately using our SFL setup is difficult. An easily measurable quantity, which was used in our previous work [48] is the response time. Therefore, we used the response time at a given position along the channel length to capture the deformation dynamics of the PDMS wall.

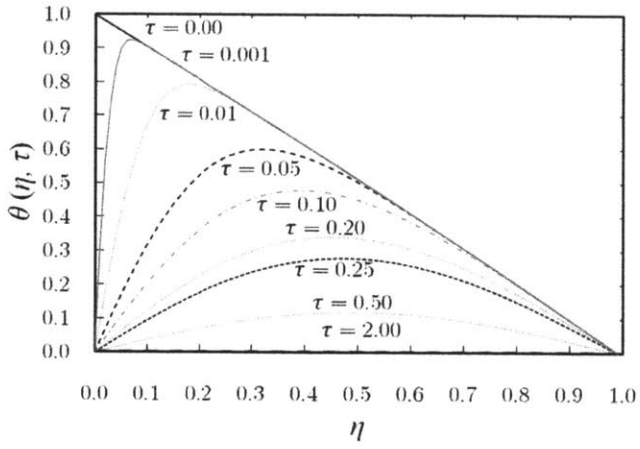

Fig. 2.2: *The deformation profile for a PDMS channel after the application of a pressure pulse for a small deformation (ε = 0.05) as predicted by the full solution, obtained from Equation A.6.*

We begin by numerically solving for the deformation profile using the full solution (Equation A.6) presented in Figure 2.2. The time when the pressure pulse is turned off is taken as $t = 0$. It can be seen from Figure 2.2 that at initial times, the relaxation is rapid followed by a more gradual change. Also, for values of $\tau > 0.2$, the deformation is almost symmetric about the center of the channel. Past studies on flow in deforming channels have depended on solving complicated equations numerically [50, 53, 54, 55]. The ability to make accurate predictions using an analytical solution would be useful. Hence, we studied the applicability of the analytical zeroth-order solution by studying the effect of increasing η on: (i) the response times at the exit of the channel as shown in Figure 2.3a and (ii) the deformation profile of a PDMS channel for an early time ($\tau = 0.1$) as shown in Figure 2.3b. It can be seen that the deviation of the full solution from the zeroth-order solution increases systematically on increasing ϵ. The maximum relative deviation of the zeroth-order solution from the full solution for response times at the exit of the channel is 5.8 % (Figure 2.3a). For profile predictions the maximum relative deviation of the zeroth-order solution from the full solution is as high as 40 % for values of $\eta \simeq 1$ (Figure 2.3b). This high relative deviation is

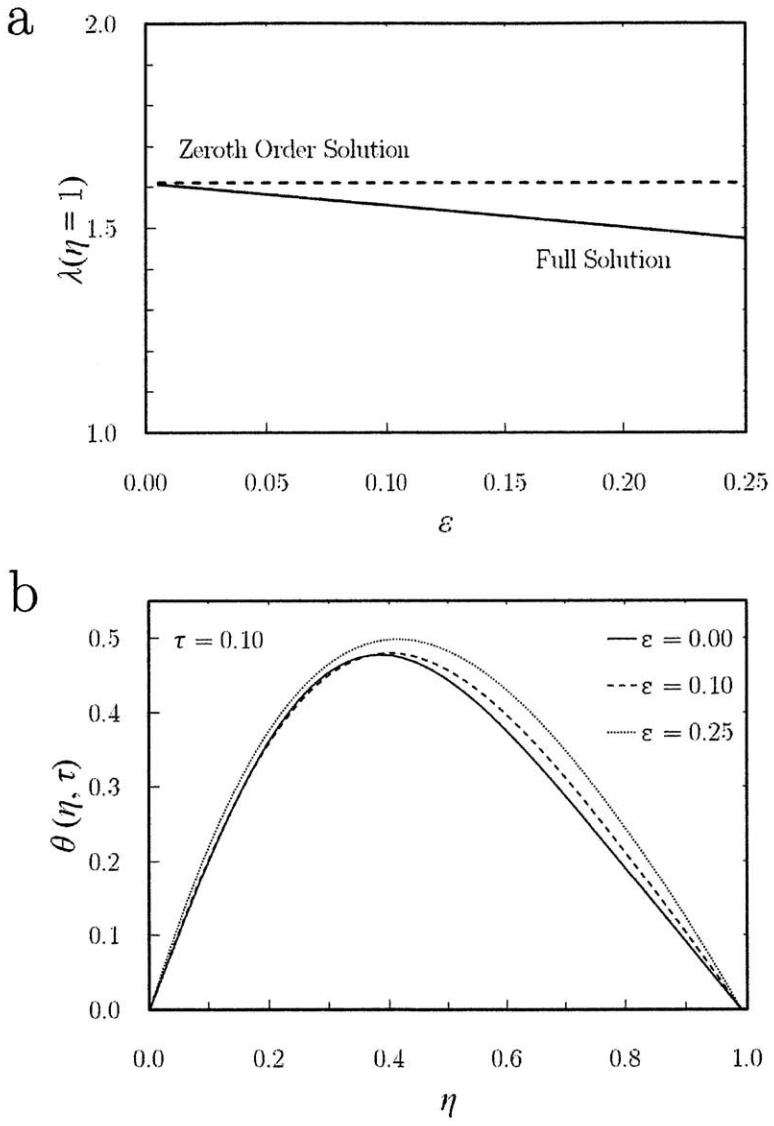

Fig. 2.3: *(a) The effect of changing ε on the nondimensionalized response times at the exit predicted by the full solution obtained using Equations A.6 and 2.21. $\varepsilon = 0$ has been used for the zeroth-order solution. (b) Comparison of the deformation profiles for a PDMS channel after the application of a pressure pulse predicted by the analytical zeroth-order and numerical full solution for ($\varepsilon = 0.1$, and 0.25) obtained using Equation A.6 for an early time ($\tau = 0.1$).*

primarily because of small channel deformations. The relative deviation is less than 15 % for large channel deformations i.e. for $0.4 < \eta < 0.6$. Further, we can see from the zeroth-order solution (Equation 2.13) that at large values of τ, the profile can be approximated by a sine curve with decreasing amplitude which agress with prediction from solving the full solution in Figure 2.2. The above analysis indicates that the zeroth-order solution is a good match to the full solution and can be used to predict the dynamics of the PDMS channel retraction at small deformations.

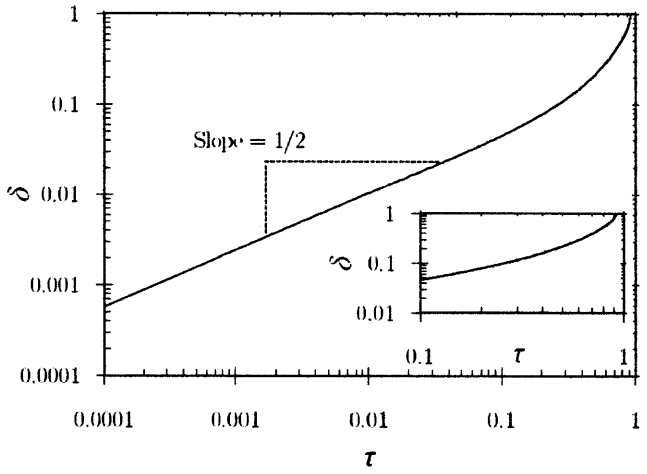

Fig. 2.4: *The penetration depth plotted against the nondimensionalized time on a log-log plot obtained using Equation 2.13. The dashed line shows the square root dependence of the penetration depth on time.*

A penetration depth analysis on the zeroth-order solution which is the solution to a simple diffusion equation, suggests a square root dependence of the penetration depth (δ) on τ (see Figure 2.4). For a plot of penetration depth and time, the penetration depth at a time was defined as scaled distance from the inlet along the x direction at which the profile has reduced by an order of magnitude i.e., to 10 % of the initial profile. Mathematically, $\theta_o(\delta, \tau) = 0.1$ (1-η). This behavior is typical of many similar simple diffusion processes. Further it can be seen from Equation 2.15 that the pressure profile for small deformations is the same as the deformation profile with an added constant. The predictions by the zeroth-order solution were compared with experimental data for: (i) the time required for the stagnation point to reach different values of η as shown in Figure 2.5a, (ii) the velocity profile as shown in the inset of Figure 2.5a and (iii) the response times along the length of the channel as shown in Figure 2.5b. From the deformation profile shown in Figure 2.2 (full solution) we would expect the velocity to decay from 1 to 0, reach a negative minimum, and then adcay back to 0 for $\eta < 0.5$ and to decay gradually from 1 to 0 over time for $\eta > 0.5$. This behavior is also predicted by the zeroth-order solution as shown in the inset of Figure 2.5b. Further, velocity predictions from the zeroth-order solution match experimental observations as shown in the inset of Figure 2.5a. In the inset of Figure 2.5a, the velocity monotonically reduces from positive to

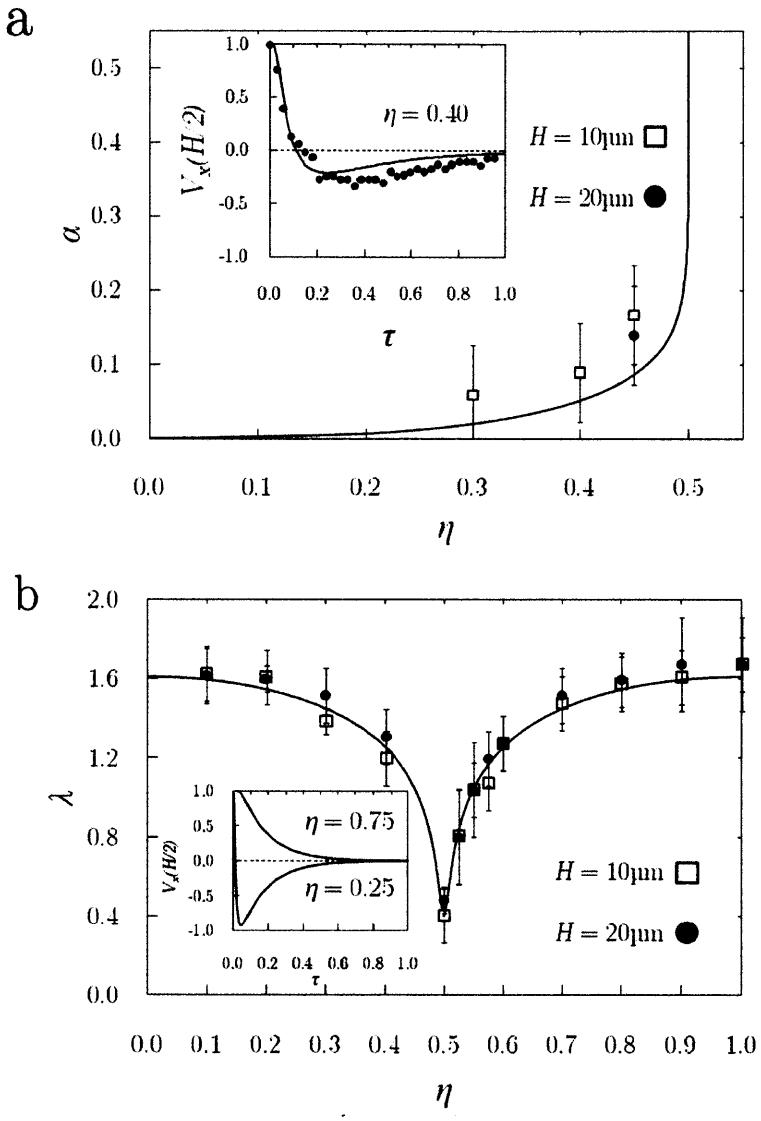

Fig. 2.5: *(a) Comparison of the nondimensionalized times for the stagnation point to move to different values of η predicted by the zeroth-order solution (solid curve) with experimental values for two different channel heights (H = 10 μm and 20 μm) and length and width of 1 cm and 20 μm, respectively. The inset compares the velocity prediction using the zeroth-order solution (solid curve) with experimental data for η = 0.4. (b) Comparison of nondimensionalized response times predicted by the zeroth-order solution (solid curve) with experimentally obtained values for same channel dimensions as in a. The inset contrasts the predictions of the decay of velocity for one value each of $\eta > 0.5$ and $\eta < 0.5$, by the zeroth order solution. The response times for the zeroth-order solution are obtained using Equation 2.20. PEG-DA is the fluid used in all the above experiments.*

negative values before reaching a negative minimum and gradually attaining a value of 0. This time for the velocity to crossover from positive to negative values at any $\eta < 0.5$ is the time required for the stagnation point to reach the corresponding η. The predictions by the zeroth-order solution for the time required for the stagnation point to reach a certain η match experimetal observations as shown in Figure 2.5a. It can also be seen from Figure 2.5 that the stagnation point approaches $\eta = 0.5$ asymptotically. We could not obtain times for the stagnation point to reach $\eta < 0.3$ due to the limitations in the frame rate of the camera. Further, the predictions by the zeroth-order solution for response times at all η are in good agreement with experimentally observed values as shown in Figure 2.5b. The V-shaped curve, almost symmetric about $\eta = 0.5$, is expected since the initial velocity is 1 for all η and the profile is almost symmetric about $\eta = 0.5$ for large values of τ (Figure 2.2). We observe that the response time converges to a value ~ 1.6 at the exit of the channel ($\eta = 1$). This value of λ is also predicted from Equation 2.23 by setting $c = 1$ (velocity reduces to 1 % of initial value).

The measured value of the elastic modulus, 2 MPa, which is within previously measured limits (0.5 to 4 MPa) [49, 50], was used to obtain the *dimensional* zeroth-order solution. The zeroth-order solution predicts a linear dependence of κ with $(4\mu WL^2)/(H^3E)$. The difference between this and our prior work is that the coefficient is explicitly calculated in the current work and hence can provide *a priori* predictions. The response times obtained experimentally are a good match to the response times predicted by the zeroth-order solution (solid black line in Figure 2.6).

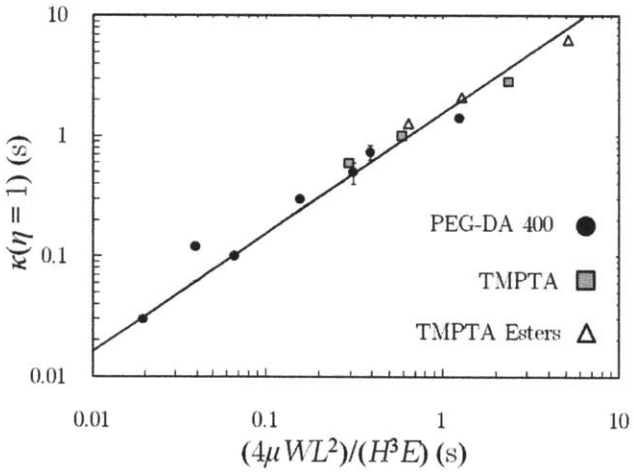

Fig. 2.6: *Plot showing the dependence of the response times at the exit of the channel versus the characeteristic time constant of the system. The solid black line is the prediction of the response times at the exit of the channel using Equation 2.20. The error bars are smaller than the size of the markers when they are not visible.*

2.6 Conclusion

In conclusion, we have presented a comprehensive analysis of the temporally complex squeeze flow which occurs in a relaxing PDMS channel. Using a regular perturbation approach, we found an analytical solution to the problem which agrees with experiments for small channel deformations. The simple form of the resulting governing zeroth-order equation (a diffusion equation) both lends itself to closed-form analytic solutions and simple physical arguments to predict system trends such as the migration of the stagnation point toward the channel center or the dependence of the relaxation (response) time on channel dimensions and material properties. This analysis lends insight into many microfluidic processes which exploit channel deformation or, conversely, try to mitigate it.

Acknowledgments

We gratefully acknowledge the support of the Singapore-MIT Alliance (SMA-2, CPE Program). We thank Dr. Anthony Balducci, Dr. Daniel Trahan and Dr. Ramin Haghgooie for useful discussions. We thank Yin Fan from the Edwin L Thomas group at MIT for help with the dynamic mechanical analysis experiment.

CHAPTER 3

Stop-Flow Lithography to Generate Cell-Laden Microgel Particles

This chapter is a part of a broader set of studies carried out to demonstrate the versatility of stop-flow lithography (SFL) as a microparticle synthesis platform. Specifically, we have tried to demonstrate the ability to generate soft cell-laden microgels with good cell viability using SFL. This work required the use of benign and careful working conditions in SFL, to maximize the cell viability. Furthermore, we used an oligomeric solution with cells suspended in it, which was different from all our prior work with SFL.

We begin the chapter by explaining the optimization of the oligomeric solution with cells suspended in it. The optimization process involved obtaining a solution which would give reasonable polymerization times in our SFL set-up as well as ensure reasonable cell viability. The optimized oligomeric solution was used to generate cell-laden 2D extruded microgels of desired shapes with good cell viability. Further, we discuss methods to improve the cell viability obtained using SFL.

This work was carried out in collaboration with the Khademhosseini lab at the Harvard-MIT Division of Health Sciences and Technology. I worked with Dr. Samsher Ali, a post doctoral candidate and Edward Lo, a visiting undergraduate student.

3.1 Overview

Encapsulating cells within hydrogels is important for generating three-dimensional (3D) tissue constructs for drug delivery and tissue engineering. This chapter describes, the fabrication of large numbers of soft particles (cell-laden microgel particles) using a continuous microfluidic process called stop-flow lithography (SFL). Prepolymer solution containing cells was flowed through a microfluidic device and arrays of individual particles were repeatedly defined using pulses of UV light through a transparency mask. Unlike photolithography, SFL can be used to synthesize microgel particles continuously while maintaining control over particle size, shape and anisotropy.Therefore, SFL may become a useful tool for generating cell-laden microgels for various biomedical applications.

3.2 Introduction

The use of polymeric biomaterials in tissue engineering has grown tremendously over the past few decades due both to their physical and chemical properties and to their biocompatibility [66]. Polymeric hydrogels, which are highly hydrated cross-linked polymer chains, are particularly attractive for engineering 3D tissue constructs due to their high water content [67, 68, 69, 70]. Cells can be encapsulated directly in hydrogels, which can be synthesized from both natural and synthetic polymers, and thus the cell seeding limitations associated with non-hydrogel tissue scaffolds can be circumvented. Microengineered hydrogels can potentially be applied in tissue engineering to recreate the complexities of in vivo tissue constructs either by engineering the microvasculature and cellular organization in large microscale scaffolds, or by assembling the building blocks in the shape of microgel tissue units to generate larger structures [70, 71]. A number of microfabrication techniques have been developed both for micropatterning hydrogels for cell encapsulation [67, 72, 73, 74, 75, 76, 77, 78, 79, 80, 81, 82, 83, 84] and for creating cell-laden microgel particles with controlled sizes and shapes [68, 85, 86]. Micropatterning of hydrogels is typically carried out using either soft lithography or photolithography, and suffers from the limitation that the resulting hydrogels are usually stuck to the glass surfaces on which they are fabricated. Microgel particles which are free floating and can be assembled to generate tissue structures [68, 86] would provide a more desirable system for these constructs. We present here an approach to achieve this goal.

Poly(ethylene glycol) (PEG) is an inert biomaterial, which has been used extensively for the encapsulation of a diverse array of cell types such as chrondocytes [87], vascular smooth muscle cells [88], osteoblasts [89] and mesenchymal stem cells [90], in addition to its many uses in a broad array of biomedical applications [67, 68, 70, 74, 75, 76, 91, 92]. When PEG macromers are terminated with methacrylate or acrylate groups, they undergo rapid crosslinking on exposure to UV light in the presence of appropriate photoinitiators [91, 93, 94], and as such, can be used with standard photolithographic processes. This method has been used widely to control cellmicroenvironment interactions in generating tissue engineered constructs that mimic native tissue architecture and direct cellular differentiation and organization [68, 70]. A shortcoming of photolithography is that it is a batch process which usually limits it to have low yields. Further, with standard photolithography it is difficult to pattern high resolution features using low viscosity prepolymer solutions.

Another lithography system, called continuous flow lithography (CFL), has recently been developed that can produce microengineered hydrogels continuously and work on a variety of different materials [30]. However, CFL is not suitable for tissue engineering applications, since it requires

a short polymerization time or slow flow-rate, in order to avoid smearing of the patterned feature in the hydrogel. Therefore, highly concentrated (either monomer or photoinitiator) prepolymer solutions are required which would be toxic to cells [95].

To overcome the limitations of CFL, SFL has been developed [48]. In the current work, we use SFL to synthesize large numbers of cell encapsulated hydrogels in a continuous manner. SFL provides distinct advantages over CFL in both throughput and control over shape and size [96]. We use SFL with photocrosslinkable prepolymer solutions containing cells, which are flowed through microfluidic channels. Cells are permanently encapsulated within PEG microgel particles by exposure to UV light and then flowed out of the device. Compared to standard lithography, SFL provides more flexibility in the type of materials and allows the use of co-flowing streams to generate particles with several adjacent functionalities [30, 48, 96]. This technique has previously been used for the synthesis of multi-functional encoded particles for bimolecular analysis [97]. In this work, we demonstrate the use of this technique for the encapsulation of cells in polymeric particles of desired shapes. We also characterize the viability of cells in hydrogels created using SFL.

3.3 Experimental Methods

3.3.1 Cell Culture

Cells were manipulated under sterile tissue culture hoods and maintained in a 95 % air/5 % CO_2 humidified incubator at 37 °C. NIH-3T3 mouse fibroblast cells were maintained in cell culture media composed of Dulbeccos Modified Eagle Media (DMEM) supplemented with 10 % Fetal Bovine Serum (FBS) and 1 % penicillin-streptomycin. Confluent dishes of NIH-3T3 fibroblast cells were passaged and fed every 2 - 3 days.

3.3.2 Photolithography

Materials

Solutions containing 10 - 40 % (w/v) poly(ethylene glycol) diacrylate (PEGDA, 700 MW, Sigma) in culture media were prepared for the experiments. Prior to UV photopolymerization, 1 - 5 % photoinitiator (w/v), 2-hydroxy-1-(4-(hydroxyethoxy) phenyl)-2-methyl-1-propanone (Irgacure 2959, CIBA Chemicals) was added to the prepolymer solution. 0.3 % (w/v) n-vinyl pyrrolidone (NVP) was also added to accelerate the photoinitiation reaction in selected samples.

Microgel Batch Polymerization

A NIH-3T3 fibroblast cell pellet was suspended in a photocrosslinkable PEGDA prepolymer solution (1.5 million cells mL^{-1}). After mixing, 8 - 10 μL of this solution was placed on top of a cover glass slide (Figure 3.1a) and exposed to 12.4 mW/cm^2 UV light (360480 nm) for various periods of time (Figure 3.1a). Following UV exposure, the cover slide was removed carefully, placed into culture media, and incubated at 37 °C for 60 minutes. Hydrogel microblocks were made from 10-40 % PEGDA, 1-5 % Irgacure 2959 (I2959), and 0 - 0.3 % NVP. The shape and size of these hydrogels were controlled using photomasks. In addition, the thickness (150 μm) of the hydrogels was controlled by the height of the spacers that were placed on two edges of the glass slide.

3.3.3 *Stop-flow Lithography*

Materials

In the SFL experiments (Figure 3.1b), the prepolymer was a mixture of 20 % (w/v) PEGDA (700 MW), 4 % (w/v) I2959, 75.7 % culture media, and 0.3 % (w/v) NVP.

Microfluidic Devices

Microfluidic devices were fabricated by pouring polydimethylsiloxane (PDMS, Sylgard 184, Dow Corning) on patterned silicon wafers (SU-8 photoresist, Microchem) containing positive-relief channels [48]. In all our experiments, we used straight channels with a height of 35 μm and a width of 500 μm. The PDMS-based microfluidic device was peeled off from the wafer and an inlet port was punched into the device to enable the prepolymer solution to be introduced to the channel. An outlet reservoir for collection of the hydrogel particles with their encapsulated cells after polymerization was cut out from the device at the other end of the channel. The PDMS microfluidic devices were bonded to PDMS coated glass slides using oxygen plasma. These assemblies were mounted on an inverted microscope (Axiovert 200, Zeiss) and the formation of cell-encapsulated hydrogels was visualized using a CCD camera (KP-M1A, Hitachi). Images were analyzed and processed using NIH Image software.

Cell Encapsulation using SFL

The prepolymer solution containing cells (6×10^6 cells per mL) was passed through a microfluidic channel using the SFL setup (Figure 3.1b). The SFL process essentially involves the three steps of stopping the liquid flow, polymerizing the patterned solution, and flowing of the particles out of the device [48]. The composition of the prepolymer solution used in the SFL hydrogel syntheses was determined from the optimal conditions obtained for the traditional photolithography process. This prepolymer solution with cells was polymerized by a flash of UV light from a 100 W HBO mercury lamp through a photomask. The photomask was designed using AutoCAD and was printed on a high-resolution printer at CAD/ART Services (Bandon, OR). A filter set that provides wide UV excitation (11000v2: UV, Chroma) was used to filter out the undesired wavelengths. A typical exposure time of 800 ms and a pressure of 1.2 psi were used for all experiments. The microgels with encapsulated cells were collected in the outlet reservoir, which was filled with the culture media to avoid aggregation of the microgel particles and to ensure that the microgels with encapsulated cells were not exposed to a high concentration of the cytotoxic monomer solution in the reservoir.

3.3.4 *Cell Viability Measurements*

Cell viability was determined using a live/dead assay (Invitrogen, CA) containing calcein AM (live cells, green) and ethidium homodimer (dead cells, red). Cell-laden microgels were incubated for 1 hour after fabrication following which they were stained by incubation with the live/dead assay agents for 10 minutes to allow the stain to diffuse into the hydrogels. The stain was removed by washing the hydrogels with culture media before the hydrogels were imaged. Cell viability was analyzed five times for the photolithography system, and three times for SFL. The fraction of viable cells in 400 μm square hydrogels prepared by photolithography (Figure 3.2) and in 120 μm diameter circular hydrogels prepared by SFL (Figure 3.5) was quantified.

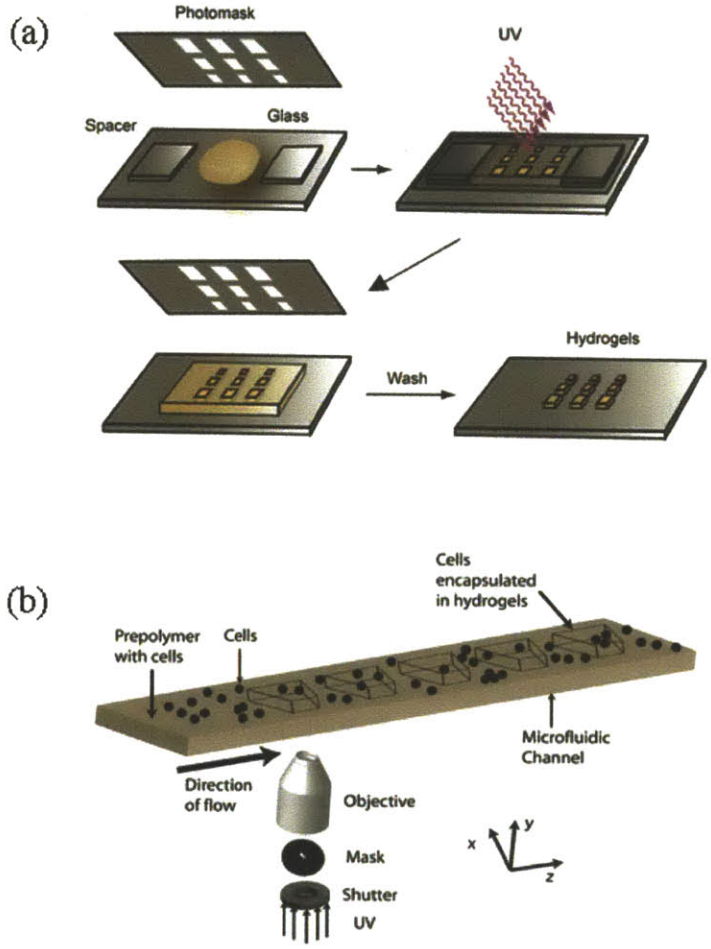

Fig. 3.1: *Schematic of the photolithography and SFL processes. (a) Schematic drawing of the formation of hydrogels using photolithography. Cells were encapsulated in hydrogels by exposing the prepolymer to UV light through a photomask. (b) Schematic diagram for the formation of cell-laden microgels using SFL. A prepolymer solution containing cells is flowed through a microchannel and polymerized by UV light through a photomask and a microscope objective.*

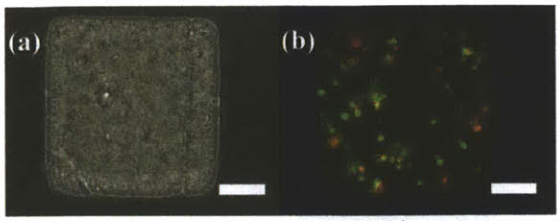

Fig. 3.2: *Cells encapsulated within a PEGDA hydrogel unit fabricated by using photolithography. (a) Phase contrast image of a hydrogel microblock. This microgel unit was made by using a prepolymer solution of 20 % PEGDA, 4 % Irgacure, and 0.3 % NVP. (b) Corresponding fluorescent image for the cell viability expressed by calcein AM (live cells, green) and ethidium homodimer (dead cells, red). Scale bars are 100 μm.*

3.4 Results and Discussion

Hydrogel microblocks were fabricated via both traditional photolithography and SFL. Standard photolithography was performed first in order to quickly screen for conditions that are both suitable for SFL and yield high cell viabilities. Monomer and photoinitiator concentrations, and polymerization time were systematically varied. These parameters have been shown in previous studies to influence cell viability inside photocrosslinked hydrogels significantly [93, 94, 30, 95, 48, 96, 97, 98]. Our goal was to maximize cell viability in the hydrogels by determining the optimized prepolymer composition and crosslinking parameters using photolithography.

The synthesis of microgels from photocrosslinkable monomers requires UV light, photoinitiator, and PEGDA, each of which is known to influence the viability of cells negatively when used at concentrations higher than a threshold, the threshold being different for different polymers and photoinitiators which needs to be determined experimentally. Thus, to maximize cell viability, it is desirable to minimize the UV exposure for a specific concentration of PEGDA and photoinitiator and yet still ensure a fully formed hydrogel, i.e., to maintain microgel pattern fidelity. The minimum exposure time required to fabricate hydrogels with controlled features was determined for a range of prepolymer solutions by systematically varying the PEGDA and I2959 concentrations. Overexposure of the prepolymer solutions to UV radiation resulted in the formation of hydrogels larger than the mask features while under exposure produced gels that were smaller than these features. The optimum UV exposure time was deemed to be the time to produce microgels with no distortion in their shapes. These times have been reported above the corresponding combinations of polymer, photoinitiator and NVP in the histograms in Figure 3.3.

The maximum allowable UV exposure in SFL is limited by the stability of the masks themselves. An exposure time of 1.5 - 2 s can burn the standard polymeric photomasks used in SFL and is typically avoided. Further, at long exposure times, there is the possibility of free-radical diffusion outside the intended polymerization region that compromises pattern fidelity in the hydrogels formed. To avoid damage to our masks and to ensure perfect control over shape and size, exposure times of less than 1 s were used in the SFL system. An exposure time of 1 s for SFL in a 35 μm tall channel corresponds to a time of about 5.5 s for creating extruded square shaped hydrogels (400

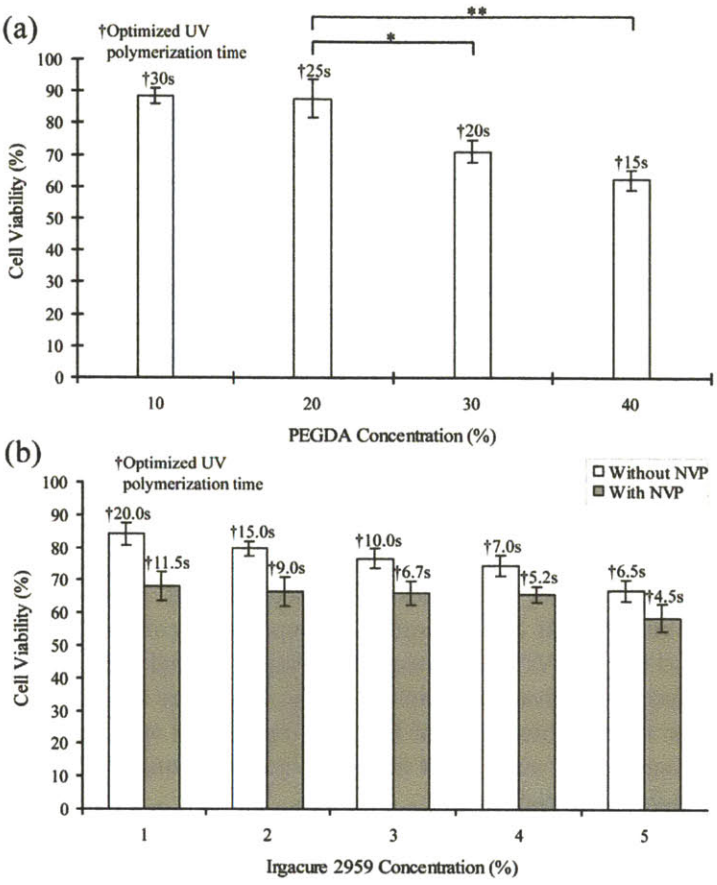

Fig. 3.3: *(a) Cell viability at different PEGDA concentrations with 0.5 % I2959 using the photolithography system. The viability was high at 10 % and 20 % PEGDA, although long UV exposure times (> 25 s) were required. The unpaired Students t-test was performed to ascertain the statistical significance of the variations in cell viability for the data sets obtained at different PEGDA concentrations. The data sets for 20 % and 30 % PEGDA (*) gave a p-value < 0.05 and the data sets for 20 % and 40 % PEGDA (**) gave a p-value < 0.01, indicating that the variation in cell viability was statistically significant in both cases and thus, an increase in PEGDA concentration from 20 % to 30 % and subsequently 40 %, results in decreasing cell viability. Therefore, a PEGDA concentration of 20 % was used in subsequent studies that varied photoinitiator concentration. (b) Viability at different I2959 concentrations with 20 % PEGDA in a photolithography system. A linear decrease was observed for samples without NVP treatment, while the cell viability of samples treated with NVP was similar at different I2959 concentrations (1 - 4 %). The optimized exposure times are marked above the corresponding conditions in the histogram.*

$\times$ 400 $\times$ 150 μm) using photolithography as determined experimentally. This difference in time is due to the difference in light intensity of the UV lamps used and thickness of particles formed in each system.

The cell viabilities obtained in the photolithography experiments at different concentrations of PEGDA (10 - 40 %) and at a constant I2959 concentration of 0.5 %, are shown in Figure 3.3a. Cell viabilities at PEGDA concentrations of 10 % and 20 % were found to be high (> 80 %), but decreased with increasing concentration beyond 20 %. Although cell viabilities at 10 % and 20 % PEGDA were high, the exposure times required to crosslink the gels were not suitable for use in SFL. The concentration of I2959 was, therefore, increased while keeping the PEGDA concentration at 20 %. The cell viabilities decreased with increasing I2959 concentrations at a PEGDA concentration of 20 % as shown in Figure 3.3b. The minimum UV exposure time also decreased with increasing I2959 concentration (6.5 s at a concentration of 5 %), but again not sufficiently to be of use in SFL.

The UV exposure time was further decreased without increasing the concentrations of PEGDA or I2959 by adding NVP to the prepolymer solution. NVP has been shown to accelerate reactions involving acrylate groups [99], with a high cell viability retention when used at low concentrations [100]. Hydrogels formed from prepolymer treated with 0.3 % NVP (w/v) showed similar viabilities at different I2959 concentrations (1 - 4 %) as indicated in Figure 3.3b. The exposure times obtained using NVP are significantly lower than those obtained without NVP and are suitable for use in SFL at an I2959 concentration of 4 %. A suitable prepolymer composition for use in SFL is 20 % PEGDA, 4 % I2959 and 0.3 % NVP, as the exposure time required for pattern fidelity is low enough for use in SFL while ensuring reasonable cell viability. In Figure 3.3 we reported the cell viability and exposure times for the combinations of PEGDA and I2959 with or without NVP analyzed in this work. The screening can be carried out for other combinations of polymers and photoinitiators and may result in a higher cell viability.

We analyzed the suitability of the proposed prepolymer solution in the SFL polymerization of hydrogels of different shapes using appropriate photomasks as shown in Figure 3.4. SFL cycles through three states which each have associated times: the time to stop the flow (t_{stop}), polymerization time ($t_{polymerize}$), and a time required to flush particles out of view (t_{flow}). The typical values for t_{stop}, $t_{polymerize}$ and t_{flow} in SFL were 200 ms, 800 ms and 100 ms, respectively, resulting in a throughput of 10^3 particles per hour using a mask which patterns one particle per exposure. For microgel particles with dimensions of 100 μm in a 35 μm tall channel, as synthesized here, the rate of particle generation by SFL can by increased by an order of magnitude by using photomasks which pattern multiple particles per exposure [48]. Further, several microfluidic channels can be combined in parallel, making the fabrication potential of SFL greater than that of photolithography, while maintaining precise control over the shape and size of each gel microparticle. A high rate of hydrogel production is essential to be able to produce sufficient quantities of particles for applications such as the self-assembly of these hydrogels into tissue structures. A circular hydrogel generated using SFL and its corresponding live/dead image is shown in Figure 3.5. The cell viability measured in hydrogels generated using SFL (68 +/- 3 %) correlated well with our values predicted using information from the photolithography system. Therefore, SFL holds great promise for the high-throughput generation of cell-laden microgels which can be used for a variety of diagnostic tools in drug delivery, DNA sequencing, and tissue engineered constructs [68, 101, 102, 103].

The viability can likely be further optimized if necessary for different biomedical applications. The decreased viability was caused by the unfavorable conditions of the prepolymer solution, particularly, the high concentration of I2959. This high photoinitiator concentration was required due

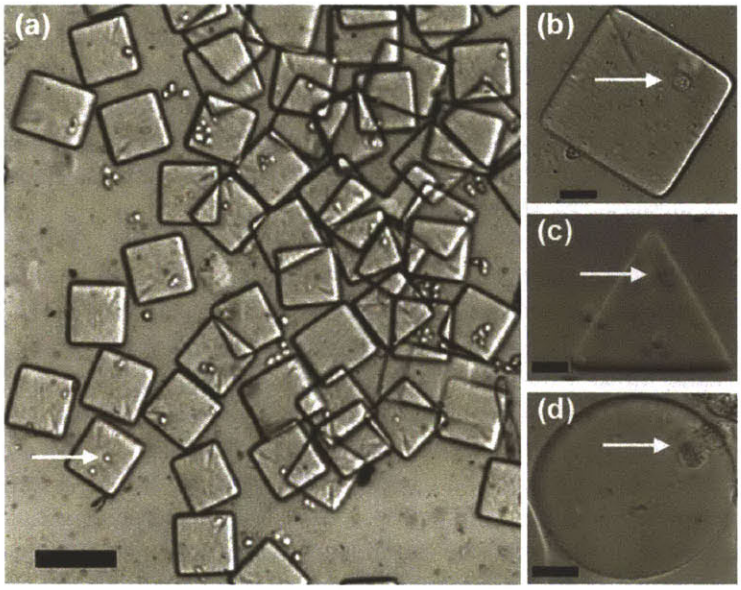

Fig. 3.4: *Cells encapsulated within hydrogels using SFL. (a) Cell-laden hydrogel micro-blocks at the outlet reservoir. (b-d) Cells trapped within hydrogels of different shapes. Scale bar in (a) is 100 μm. Scale bars in (b), (c), and (d) are 20 μm.*

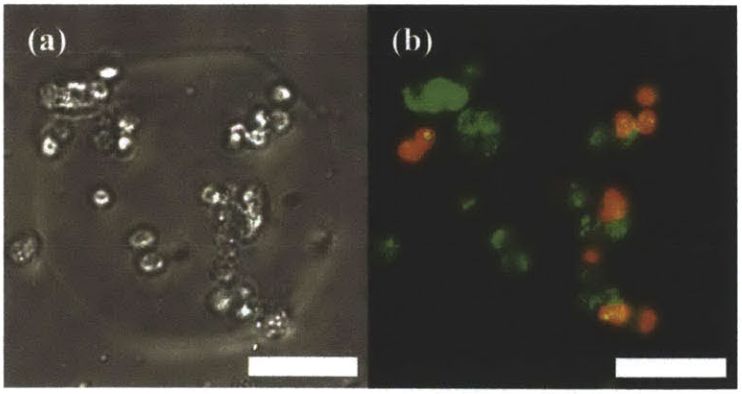

Fig. 3.5: *Cells encapsulated within PEGDA hydrogel units fabricated by using SFL. (a) Phase contrast image of a hydrogel microblock. This microblock unit was made by using a prepolymer solution of 20 % PEGDA, 4 % I2959 and 0.3 % NVP. (b) Fluorescent image for the cell viability expressed by calcein AM (live cells, green) and ethidium homodimer (dead cells, red). Scale bars are 50 μm.*

to the time constraint imposed by the masks used. To eliminate the necessity of a prepolymer that crosslinks rapidly, glass or chrome masks can be used which can withstand longer exposure times. Further, other more potent combinations of polymers and photoinitiators which require lower polymerization times while ensuring high cell viability can be investigated. These combinations of polymers and photoinitiators can be screened using photolithography to minimize exposure times before being used in SFL. Shorter exposure times would alleviate diffusion limitations to maintaining shape fidelity and increase the throughput.

The SFL system can potentially be used for cells other than the NIH - 3T3 mouse fibroblast cells used in this work. The hydrogel particles synthesized in this study could be assembled into ordered meso-structures using various methods such as evaporation driven assembly [31], DNA hybridization [104, 105, 106], or using selective wetting at a liquid-liquid interface [107, 108]. Furthermore, SFL can be used for creating multicomponent hydrogels [30, 48, 96, 97] by co-flowing more than one stream containing either different cells and the same prepolymer or the same cells but different prepolymers or a combination of both. These anisotropic particles can be assembled, exploiting the difference in surface energies of different regions of a particle, finding potential application for generating tissue constructs. Another application of anisotropic microgel particles is multi-cell drug assays, reducing the cost and time involved significantly. The hydrogels formed using SFL can also be used for immuno-isolation of cells for implantation [79, 80, 81, 82, 83, 84].

3.5 Conclusion

We demonstrated the use of SFL to generate high-throughput cell-laden hydrogel microblocks in a continuous manner. The viability of cells encapsulated within hydrogels, for different experimental parameters (i.e. monomer and photoinitiator concentrations), was analyzed using a photolithography setup to obtain an optimized prepolymer solution for SFL. The majority of cells encapsulated within hydrogels generated by SFL using the optimized solution remained viable. The potential of SFL to create shape-controlled microgels continuously makes it a fertile field for further studies. Further studies should be carried out to characterize nutrient transfer to cells which is important for the fabrication of 3D tissue constructs.

Acknowledgments

This work was partly supported by the Coulter Foundation, National Institutes of Health (NIH), the Center for Integration of Medicine and Innovative Technology (CIMIT), US Army Core of Engineer, the Charles Stark Draper Laboratory and the NSF NIRT Grant No. CTS-0304128. S. Ali thanks the Higher Education Commission (HEC) of Pakistan for financial support and we thank Dhananjay Dendukuri and Daniel C. Pregibon for useful discussions.

CHAPTER 4

Stop-Flow Lithography of Colloidal, Glass and Silicon Microcomponents

In this chapter we present results which achieve in part, our broader goal of demonstrating the versatility of stop-flow lithography (SFL) as a microparticle synthesis platform. We demonstrate the ability to synthesize hard ceramic microcomponents using SFL. We used a non-Newtonian oligomeric solution containing 500 nm silica core-shell particles suspended in it. We had to ensure the silica solution was index matched before mixing with the oligomeric solution to avoid loss in resolution of synthesized microparticles due to scattering of light. We also used high presures to ensure the flow of the shear thinning silica solution we used for this work. We synthesized polymeric microcomponents with encapsulated silica to begin with. We then converted these to both dense and porous silica and silicon microcomponents by sintering at a high temperature.

We collaborated with the Lewis lab at the University of Illinois, Urbana-Champaign and the Sandhage lab at the Georgia Institute of Technology. I worked with Dr. Robert Shepherd from the University of Illinois, Urbana-Champaign to optimize the conditions in SFL to synthesize polymeric microcomponents. The porous silica microcomponents obtained after sintering the polymeric microparticles, were converted to silicon microcomponents by magnesiothermic reduction by Dr. Zhihao Bao from the Georgia Institute of Technology.

4.1 Overview

The assembly of oxide and non-oxide microcomponents from colloidal building blocks is central to a broad array of applications, including sensors, optical devices, and microelectromechanical systems (MEMS), as well as to fundamental studies of granular materials. Progress in these areas has been hindered by the availability of colloidal microcomponents of precisely tailored size, shape, and composition. In this chapter, we report a method for patterning colloidal building blocks into controlled structures via stop-flow lithography (SFL). Microcomponents are created at rates that exceed 10^3 min^{-1} using an index-matched system composed of silica microspheres suspended in a photocurable acrylamide solution. Upon drying, the resulting colloidal structures are akin to non-spherical granular media. These structures are then transformed at elevated temperatures into microcomponents composed of porous or glassy silicon oxide or porous silicon via magnesiothermic reduction. The SFL method provides exquisite control over component size, shape, and composition required for advancing a wide variety of fields.

4.2 Introduction

There is tremendous interest in developing new patterning methods for creating precisely tailored microcomponents composed of colloidal building blocks, amorphous or polycrystalline oxides, and silicon. For example, colloidal-based microcomponents produced in simple non-spherical shapes, such as discoid, triangular, cuboid, and rectangular, may serve as novel granular feedstock for ceramics [109, 110], optical display technologies [111] and pharmaceuticals [112, 113]. Traditional methods for producing colloidal granules, such as fluid bed granulation [114], high shear mixer granulation [115] and spray drying [110], do not provide adequate control over granule size, shape, or composition. Equally important is the need to create porous and dense oxide and non-oxide microcomponents for functional devices ranging from micro-mixers and heat exchangers [116, 117] to MEMS [118, 119, 120, 121, 122]. Although several fabrication methods have been recently introduced, including LIGA [123, 124], micro-extrusion [125], micro-injection molding [126, 127], micro-stereolithography [128, 129] and micro-electro-discharge machining [130], each lacks the materials flexibility and rapid assembly times desired for many applications.

Microfluidic assembly techniques provide a new platform for creating novel polymer particles from photopolymerizable resins [39, 40, 131, 132], hydrogels [133, 41] and colloidal granules [134]. In most cases, the particles (or granules) are produced by co-flowing immiscible liquids through a microfluidic device that induces droplet break off yielding one particle at a time [135, 136]. Due to surface-tension effects, only spherical shapes or deformations thereof are readily produced. Another technique for the production of polymeric microparticles, forms polystyrene microbeads into higher order assemblies via microfluidic patterning and thermal fusion [137]. By contrast, stop-flow lithography (SFL) [48] enables a rich array of simple and complex shapes to be produced in parallel. This technique employs microscope projection photolithography [138] to create patterned structures within a microfluidic device, eliminating the need for clean room conditions. To date, SFL has been used for applications like biomolecular analysis [97], assembly of Janus particles [96] and interference lithography [139]. Here, for the first time, we report the assembly of colloidal granules and microcomponents in the form of microgear, triangular, discoid, cuboid, and rectangular shapes using SFL as well as demonstrate pathways by which they can be transformed into both porous and dense oxide and non-oxide structures.

4.3 Experimental

4.3.1 Materials System

Colloidal suspensions are prepared by first adding an appropriate amount of polyethyleneimine (PEI; 1800 g mol^{-1}; Aldrich Chemical Co to deionized water. The solution pH is then adjusted to 6 by adding aliquots of a 1M HNO_3 solution (Fisher Scientific). Following this, silica microspheres (ϕ^v_{silica} = 0.5, 500 nm +/- 25 nm diameter, FUSO, Japan) are added to the solution and allowed to stir overnight to allow the desired adsorption of 0.5 mg PEI/m^2 silica [140]. This opaque suspension is then index-matched by the addition of dimethyl sulfoxide (DMSO; Fisher Scientific) to achieve a volumetric ratio of 65:35 v/v DMSO to water. The suspension is then concentrated by centrifuging at 3000 rpm. After the supernatant is decanted, a photoinitiator, ϕ^v_{init} = 0.03 (Darocur 1173, Ciba), acrylamide monomer, a ϕ^w_{acryl} = 0.09 (Acros Organics), and crosslinking agent N,N methylene bisacrylamide (Aldrich Chemical Co.) at an 8:2 w/w ratio of monomer to crosslinking agent is added to the dense sediment. The index-matching is finely tuned by adding deionized water to yield a final composition of ϕ^v_{silica} = 0.50, 62:38 v/v of DMSO:water, and $\phi^w_{acrylamide}$ = 0.08. Note, to facilitate direct visualization of representative patterned microcomponents, silica microspheres (ca. 700 nm in diameter) are synthesized with a fluorescent, rhodamine isothiocyanate (RITC) core-shell architecture following the procedure described in Reference [141]. A 1:9 number ratio of fluorescent to non-fluorescent silica is utilized in suspension.

4.3.2 Suspension Rheology

Viscometry measurements are carried out on suspensions of varying colloid volume using a controlled-stress rheometer (CVOR, Bohlin) equipped with a cup and bob geometry (C15 cell). Prior to taking measurements, a preshear of 50 s^{-1} is applied for 10 seconds and allowed to rest for 300 seconds before starting each experiment. We start with the 50 v/o suspension used in microcomponent formation, and measure the viscosity from a shear rate of 0.01 to 300 s^{-1}. After the measurement, the suspension is diluted with the acrylamide solution, and the measurement is subsequently repeated for 45, 40, and 35 v/o suspensions.

4.3.3 Device Fabrication

Microfluidic devices are produced via soft lithography [142] by pouring PDMS (Sylgard 184; Dow Corning) onto a silicon wafer patterned with SU-8 photoresist features (SU-8 50; Microchem). After curing the PDMS, the mold is cut out and treated via UVO [143] with an accompanying PDMS coated coverslip. After treatment, the mold and coverslip is brought into conformal contact and allowed to bond, forming a monolithic structure. Though we did not find it necessary, in most cases, to protect the microchannel surface during UVO, we still followed the protection procedures developed in Reference [109]. The microchannel dimensions used in these experiments are 1 mm in diameter with channel heights of either 30 μm, 40 μm or 55 μm, by spin-coating at either 3000, 2500, or 2000 rpm, though channel heights as low as 10 μm have been successfully used in this system. Photomasks are rendered with CAD (Autocad 2005) and printed via a high-resolution laser printer (5080 dpi; CAD/Art Services, Inc.).

4.3.4 Stop-flow Lithography

The transparent colloidal suspension is flowed into the microfluidic device in a pulsed sequence, synchronized with flashes of UV exposure as described in Reference [48]. For this material system, by applying a voltage to a solenoid valve through homemade Labview software, the suspension is flowed at 2 psi for 400 ms, the pressure is then stopped by removal of the applied voltage. After the pressure is released, the system is allowed to relax for 300 ms, where the motion of the fluid comes to a full stop. Immediately after the flow is stopped, UV light is projected through a photomask into an objective lens (20X, N.A. 0.46; Zeiss) that focuses the negative mask image onto the microchannel for a periods of 200 ms or 400 ms, depending on the reaction extent desired for polymerization and crosslinking of the acrylamide monomers. This process is repeated until the desired number of microcomponents are formed.

4.3.5 Particle Tracking

A concentrated colloidal suspension ($\phi_{silica} = 0.5$) that contains a dilute amount ($\phi = 0.001$) of 1.6 μm latex beads (Sulfate modified; A37297; Invitrogen) is flowed through representative microchannels that are 1 mm wide, 1 cm long, and 40 μm thick. A pressure of 2 psi is applied for 1 s and turned off for 2 s, before repeating the cycle. A high-speed camera (Phantom V7.1) is used to record video at a frame rate of 700 fps through an objective lens (60$\times$ oil immersion; Olympus). Particle tracking algorithms developed by Crocker and Grier for IDL are used to track a single particle at the center of the microchannel, 20 μm into the channel depth, near the output to determine the particle position within each frame. The particle velocity is determined using the forward difference method between frames.

4.3.6 Thermal Processing

Representative colloidal microcomponents are harvested from the SFL device, dried, and then densified on a sapphire window (Edmunds Optics) by heating at 1 °C min^{-1} to 1150 °C for varying hold times of 1, 3, or 10 h before cooling to ambient temperature at a rate of 1 °C min^{-1}. Porous and dense glass (silica) microgears are produced depending on the hold time employed.

4.3.7 Silicon Replication

Porous glass microgears are transformed into silicon replicas by a magnesiothermic reduction proces [144]. Each microgear is placed on a silicon substrate within a low carbon (1010) steel boat. The source of magnesium vapor, 0.3 g of Mg_2Si powder (99.5 % purity, Alfa Aesar), is placed at the other end of the steel boat at a distance of 1 cm from the microgear. The steel boat is placed within a steel ampoule (2.5 cm in diameter, 15.2 cm in length) that is then welded shut in an argon atmosphere. The ampoule is heated at a rate of 7 °C min^{-1} to 850 °C and held at this temperature for 2.5 h to allow the magnesium vapor to fully react with the porous silica microgear to yield a mixture of magnesium oxide and silicon. After cooling to room temperature, the reacted gear is removed from the ampoule and then immersed in an hydrochloric acid (HCl) solution (HCl:H2O:EtOH molar ratio of 0.7:4.7:8.9) for 4 h at room temperature to selectively dissolve MgO yielding the desired nanoporous silicon microcomponents.

4.3.8 Microcomponent Characterization

Representative colloidal microcomponents that contain fluorescent-core silica microspheres are harvested from the SFL device, dried, and then immersed in a 65:35 DMSO:water solution prior to imaging with a confocal scanning fluorescence microscope (SP2 Multiphoton, Leica) equipped with an Argon laser (excitation wavelength of 514 nm). Confocal x-y scans are acquired at 0.765 μm intervals in the z-direction through a given microcomponent. The images are then compiled into a 3D rendering using Amira imaging software and the x, y, and z values given from the confocal images. Representative colloidal, glass, and nanoporous silicon microcomponents are imaged using scanning electron microscopy (SEM) (6060 LV, JEOL). Energy dispersive x-ray analysis (EDX) (ISIS, Oxford Instruments) is performed on replicated silicon microgears to verify complete reaction and MgO dissolution conversion. In addition, surface roughness measurements are carried out using atomic force microscopy (AFM) (MFP - 3D; Asylum Research). These data are acquired by probing three 25 μm^2 areas selected randomly. The root-mean-squared, RMS, roughness values are calculated by taking an average of each data set after applying a 3^{rd} degree polynomial flatness convolution algorithm.

4.4 Results and Discussion

We demonstrate this novel assembly method by first designing a model colloidal suspension capable of being rapidly polymerized via projection lithography within a microfluidic device. The system is composed of silica microspheres suspended in a mixture of dimethyl sulfoxide (DMSO) and water at a volume fraction, ϕ_{silica}, of 0.5. The suspension also contains acrylamide monomer ($\phi_{acrylamide}$ = 0.08), a cross-linking agent (monomer:crosslinking agent ratio of 4:1 by weight) and photoinitiator ($\phi_{initiator}$ = 0.03). This photopolymerizable colloidal suspension must exhibit limited scattering and absorption of the incident ultraviolet light to ensure high resolution of the as-patterned features. Aqueous silica suspensions are opaque due to the refractive index difference between silica (n = 1.46) and water (n = 1.33). By adding an appropriate amount of DMSO (n = 1.48), the colloid and fluid phases are index-matched thereby minimizing scattering from the suspended particles.

The SFL setup utilized in the present work is illustrated in Figure 4.1a. Patterned microcomponent(s) are formed by projecting ultraviolet light through a photomask inserted into the field stop of an inverted microscope. Microcomponent fabrication involves the stop-polymerize-flow sequence [48] captured in optical images shown in Figure 4.1b-d. Figure 4.1b shows an image of a suspension-filled microchannel prior to UV polymerization. The suspension is transparent due to its index-matched state. Figure 4.1c is acquired immediately after photopolymerization and shows a colloidal microgear that consists of a polyacrylamide network filled with silica microspheres and the solvent mixture. The modest change in refractive index upon polymerization enables one to visualize the as-patterned structure within the microchannel. Finally, Figure 4.1d shows the microgear as it accelerates in response to the onset of an applied pressure within the microchannel.

To minimize microcomponent shrinkage during drying, we utilized suspensions with high solids loading (ϕ_{silica} = 0.5) that are capable of flowing through the SFL device without clogging. The photopolymerizable suspensions exhibit Newtonian flow behavior when $\phi_{silica} < 0.35$ (data not shown). At $\phi_{silica} \sim 0.35$, there is a transition to shear thinning behavior, which becomes more pronounced with increasing ϕ_{silica} (see Figure 4.2a). This behavior facilitates their flow through the SFL device at modest applied pressures.

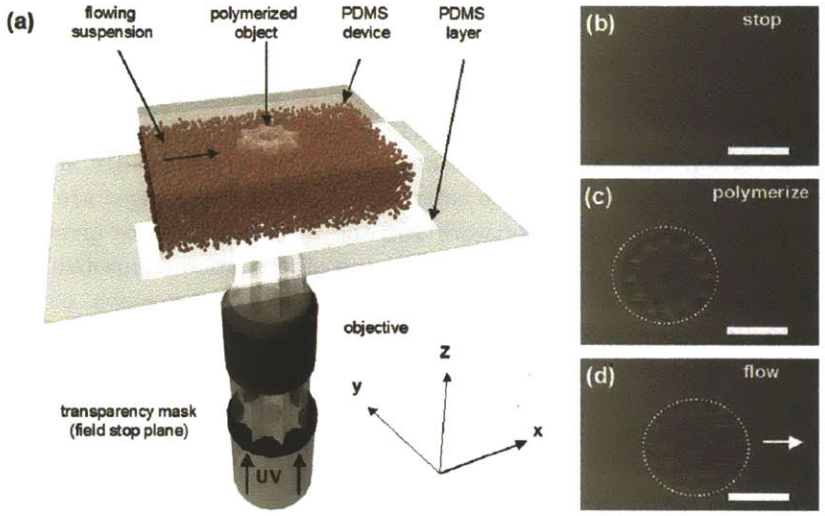

Fig. 4.1: *(a) Schematic illustration of stop flow lithography (SFL) system, where a photocurable, index-matched silica-acrylamide suspension is flowed through a PDMS microchannel. Microcomponents are patterned by (b) bringing the suspension to a complete stop within the microchannel, then (c) illuminating a defined volume of the suspension with UV light to induce photopolymerization, followed by (d) ejection of the as-patterned component through re-initiation of suspension flow. This process is repeated until the desired number of microcomponents is formed, at rates exceeding* 10^3 min^{-1}. *[Scalebars (b-d) are 100* μm*].*

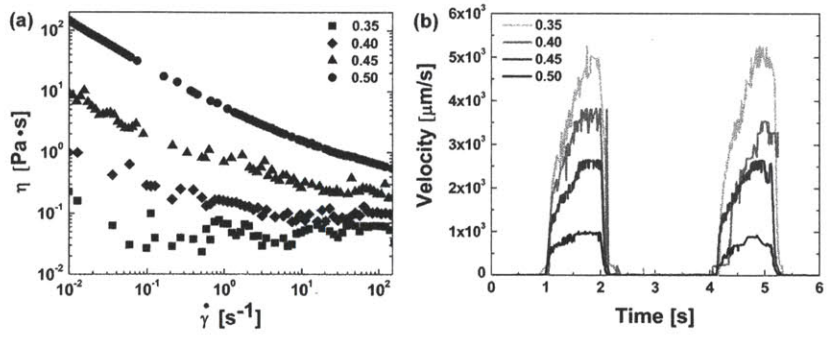

Fig. 4.2: *(a) Steady shear viscosity as a function of shear rate for index-matched, silica-acrylamide suspensions of varying colloid volume fraction. (b) Centerline velocities for increasing solids loadings of colloidal silica within a 40* μm *microchannel.*

Table 4.1: *Comparison between estimated centerline velocities using Equation 4.1 and experimentally obtained centerline velocities for the colloidal suspensions.*

ϕ_{silica}	Maximum Centerline Velocity (μm / s)	Characteristic Shear Rate (s^{-1}) (= $2VH^{-1}$)	Viscosity (Pa.s)	Estimated Centerline Velocity (μm / s)
0.35	5245	262	0.08	2675
0.40	3822	191	0.10	4540
0.45	2649	132	0.20	2270
0.50	1000	50	0.75	605

We carried out particle tracking measurements for index-matched suspensions of varying colloidal volume fraction to obtain centerline velocities (Figure 4.2b). We estimate characteristic shear rates, which range from 50 to 262 s^{-1}, for colloidal suspensions of $\phi_{silica} = 0.5$ to 0.35, respectively, by dividing the maximum centerline velocity by half the microchannel height. Over this shear rate range, each suspension can be approximated to first order as a Newtonian fluid (see Figure 4.2a). The centerline velocity at the exit of a low aspect ratio ($H/W < 1$) deformable PDMS microchannel is estimated by [48, 50]:

$$V(L) = \frac{H^3 E}{32 W \eta L}\left[\left(1 + \frac{PW}{EH}\right)^4 - 1\right] \tag{4.1}$$

where η is the viscosity, L is the microchannel length, W is the microchannel width, E is the Youngs modulus of PDMS (1MPa), and H is the microchannel height. These estimated velocities are in good agreement with the measured maximum centerline velocities (Table 4.1).

SFL consists of three distinct steps stop, polymerize, and flow repeated in a cyclical fashion [48]; hence, the times required to stop flow (t_{stop}), polymerize ($t_{polymerize}$), and expel the patterned components (t_{flow}) are key experimental parameters. We determine the values for t_{stop}, which range from 100 to 300 ms for colloidal suspensions of $\phi_{silica} = 0.5$ to 0.35, respectively, from the particle tracking data shown in Figure 4.2b. In our experiments, we utilize a value of 300 ms for t_{stop}, which is sufficient to ensure complete cessation of suspension flow prior to polymerization. We employ values of $t_{polymerize}$ that vary from $\sim$ 200 to 400 ms depending on the mask design, which enable microcomponents to be patterned with precise control over shape and size. Finally, a t_{flow} value of 400 ms is used, which is sufficient to expel the patterned microcomponent from the field of view thereby preventing its double exposure.

To demonstrate the flexibility of this patterning technique, we produce colloidal microcomponents in both simple and complex shapes (see Figure 4.3). Specifically, we assemble microcomponents with geometries that vary from triangular, cuboid, discoid and rectangular shapes to more complicated geometries, such as microgears, with uniform sizes that range from 20 μm to 300 μm in maximum dimension. Microcomponents composed of simple geometric forms are polymerized for shorter times, because they are able to withstand the modest deformation that occurs during ejection from the microchannel. By contrast, the complex microgears require the longest tpolymerize (400 ms) to produce rigid structures that maintain their shape during ejection. Because the

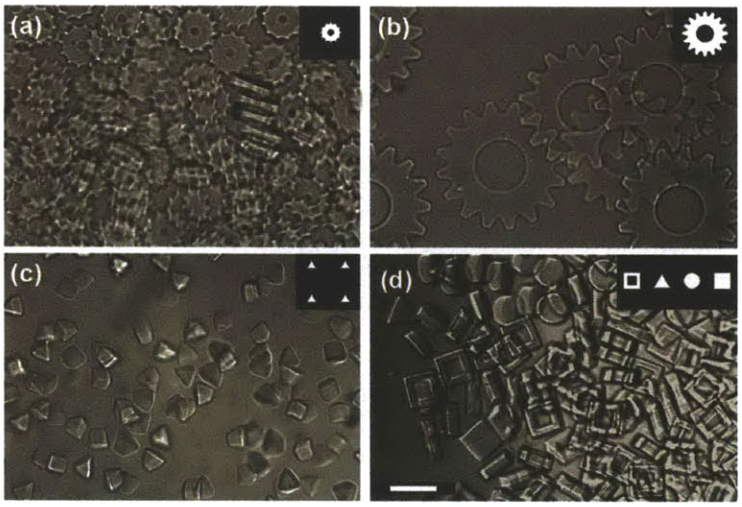

Fig. 4.3: *Optical images of colloidal microcomponents formed via SFL using the corresponding mask shown in each inset: (a) small microgears formed in a 30 μm thick microchannel, (b) large microgears formed in a 55 μm thick microchannel, (c) equilateral triangles formed in a 60 μm thick microchannel, and (d) an array of disk, cube, triangular, and rectangular microcomponents formed in a 40 μm thick microchannel. [Scalebar is 100 μm].*

microcomponents remain immersed in an index-matched solution, they appear translucent in the optical images depicted in Figure 4.3. The microcomponent production rates for the 2×2 and 4×1 photomask arrays are approximately 240 min^{-1} for simple shapes and 200 min^{-1} for gears. This rate can be enhanced by more than an order of magnitude using a photomask with a larger array.

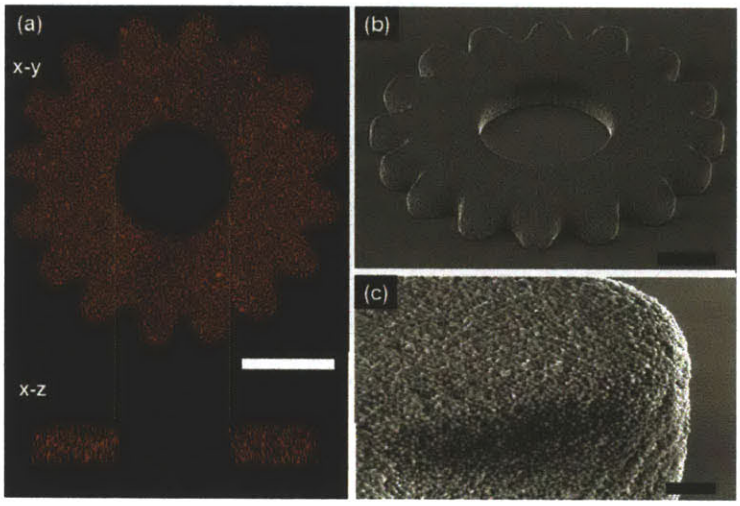

Fig. 4.4: *(a) Confocal image (top, x-y plane and bottom, x-z plane) of patterned colloidal microgear (x-y scan acquired at z = 20 μm) in an index-matched solution. (b) SEM image of a dried colloidal microgear composed of (c) densely packed silica microparticles. [Scalebars for (a)-(c) are 100 μm, 50 μm and 5 μm, respectively].*

We investigate the distribution of colloidal microspheres within the polymerized microcomponents using a combination of confocal scanning microscopy, CLSM [145] and scanning electron microscopy (SEM). Figure 4.4a shows a confocal image (x-y scan) acquired at depth of 20 μm into a representative microgear in which 10 % of the silica microspheres contain fluorescent cores. Both the x-y and x-z scans reveal that the microspheres are randomly distributed throughout the microcomponent. A full 3D reconstruction of this microgear, consisting of a series of x-y slices stacked together, is presented as supplemental information. From this data, we find that the microgear thickness is approximately 50 μm. Since, in this case, photopolymerization occurred within a 55 μm deep microchannel; we believe that inhibition layers no more than a few microns thick form at the suspension-microchannel interfaces. Their presence facilitates microcomponent ejection once suspension flow is reinitiated. Importantly, the colloidal microgears maintain their shape after being harvested from the microfluidic device and dried, as shown in the SEM images provided in Figure 4.4b-c. The tilted image (Figure 4.4b) clearly demonstrates that the photomask features can be replicated with a high degree of precision, while the corresponding high magnification view reveals that the colloidal microspheres are densely packed together with a final solids volume fraction of 0.62 based on optical micrographs and assuming isotropic shrinkage. We have determined the dried inner and outer gear radii to be 95 +/- 3 μm and 225 +/- 3 μm, respectively. Additionally, through the formation of an array of microcomponents of decreasing size, we find that the minimum

microcomponent size is approximately 8 μm (Figure 4.5).

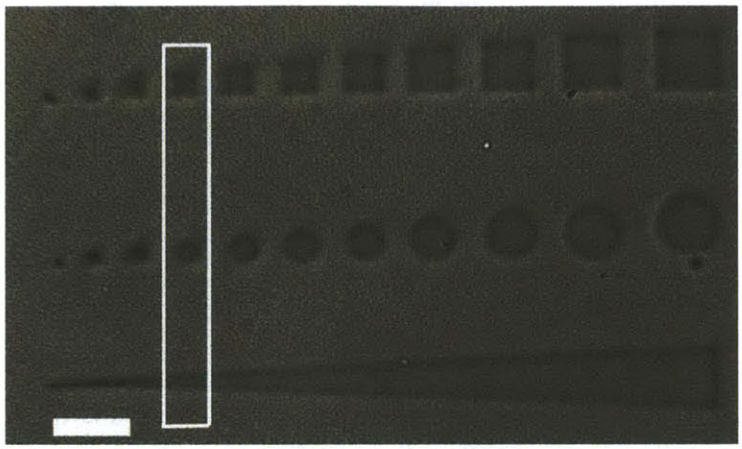

Fig. 4.5: *Patterns used to find minimum reproducible feature size. Solid line shows the minimum feature size that can be replicated with high precision. [Scalebar is 30 μm].*

To enhance their structural integrity, the colloidal microgears are transformed into fully dense, glassy silica microgears by sintering at 1150 °C for 3 - 10 h. SEM images of a sintered glass microgear are shown in Figure 4.6a-b. During densification, the microgear undergoes significant radial shrinkage ($\sim$ 25 %) resulting in the final dimensions of 71 +/- 1 μm (inner radius) and 164 +/- 4 μm (outer radius). Because the microcomponents are sintered on a transparent sapphire window, we can also image them via transmitted light microscopy. After sintering at 1150 °C for 3 h, the microgears are translucent. However, their surface remains rough on the size scale of the individual microsphere building blocks. At longer hold times ($\sim$ 10 h), the surface of the microgears becomes smooth. Their root-mean-squared (rms) surface roughness is approximately 6 nm, as determined by atomic force microscopy (see Figure 4.6c).

Porous silica microgears are produced by partial sintering at 1150 °C for 1 h, as shown in Figures 4.6d-e. These microcomponents are mechanically stable and can be readily handled. Their rms surface roughness is $\sim$ 130 nm (see Figure 4.6f) due to the significant amount of interconnected porosity, 23 volume %, that is retained after heat treatment. This porosity aids their transformation to porous silicon microcomponents via magnesiothermic reduction [144]. In this process, the silica microgears are heated to 850 °C for 2.5 h in the presence of magnesium gas volatilized from Mg_2Si powder to promote the following reaction:

$$2Mg(g) + SiO_2(s) \rightarrow 2MgO(s) + Si(s) \tag{4.2}$$

The MgO/Si composite generated by this reaction retains its 3D shape and porous features. The MgO/Si composite replicas are then immersed in a hydrochloric acid solution for 4 h to selectively dissolve the oxide phase yielding the desired porous silicon microgear replicas shown in Figure 4.6g-h. Energy dispersive x-ray analysis, EDX, reveals the presence of a strong silicon peak with a minimal oxygen peak (see Figure 4.6i). The resulting silicon replicas contain two distinct pore size

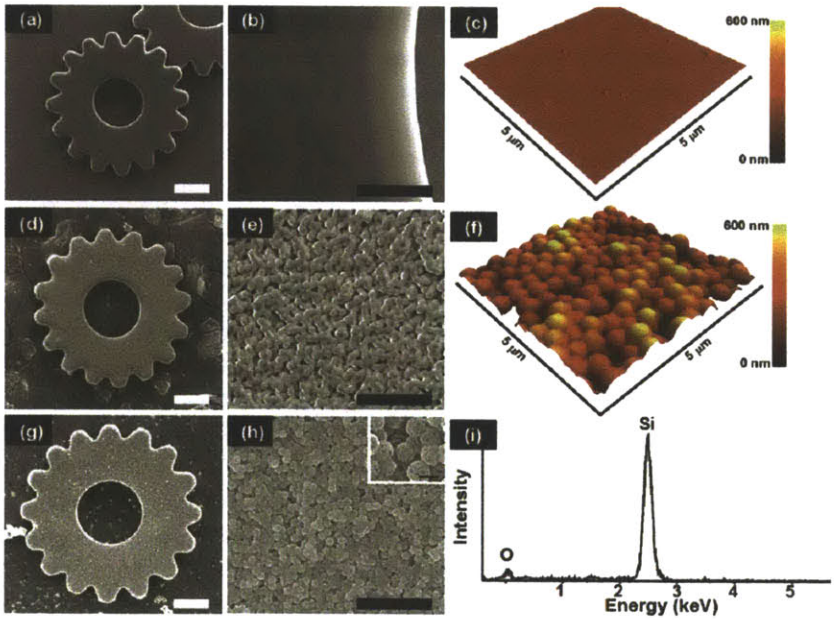

Fig. 4.6: *(a) SEM micrographs of a glassy silica microgear fully densified at 1150 °C for 10 h, which is composed of (b) a smooth surface and dense interior (not shown), as demonstrated by (c) AFM surface reconstruction, (d) SEM micrographs of a porous silica microgear partially densified at 1150 °C for 1 h, which is composed of (e) a porous network of fused silica microspheres, with (f) AFM surface reconstruction demonstrating roughness on the order of colloid size, and (g) SEM micrographs of a silicon microgear converted by a magnesiothermic reduction of the porous silica microgear shown in (d). This conversion reaction yields the nanoporous silicon replica shown at higher magnification in (h) with (i) EDX revealing a large silicon peak. [Scalebars are 50 μm for (a,d,g), 5μm for (b,e,h), and 500 nm for the inset in (h)].*

distributions, one associated with the interstices between the partially sintered silica microspheres and the other associated with the ghost microspheres on a finer scale, where each microsphere contains 65 v/o interior porosity based on the assumption of complete conversion to silicon and removal of MgO. These porosities, combined with the 5 % volumetric increase observed during the microcomponent conversion process, result in a final silicon volume fraction of 0.27. Note, the silicon content could be enhanced significantly through an additional process, such as chemical vapor deposition [118]. The rms surface roughness of the porous silicon microgears is 118 nm, in good agreement with the surface roughness of the porous silica structures from which they are replicated. These values scale with the colloid size; hence, further improvements are possible by simply reducing the mean diameter of the colloidal building blocks utilized in suspension.

Using the SFL technique, we can pattern microcomponents with a diverse array of geometric shapes, compositions, and physical properties with overall dimensions that range from approximately 10 μm to 1 mm. Colloidal microcomponents may be used as novel granular media for fundamental studies of flow, packing, and compaction behavior. Recent efforts have shown that significant packing enhancements are observed simply by changing granule shape from spherical to ellipsoidal granules [146]. Now, the possibility exists to explore such effects over a much broader range of granular shapes. Moreover, one can create granular building blocks with increasing chemical complexity by coflowing multiple suspensions of varying composition within the microfluidic device. For example, utilization of granular feedstock with Janus [134, 147] or other patchy motifs [2, 148] would enable the fabrication of more sophisticated bulk ceramics with nearly periodic compositional variations. We also demonstrated that the patterned colloidal microcomponents can be converted to functional structures by densifying them at elevated temperature or via novel chemical conversion and replication schemes. As one example, porous silicon microcomponents may find potential application as gas sensors [144], photoluminescent materials [145, 149] or MEMS devices. In related work, porous silicon structures replicated from biologically engineered silica granules, or diatom frustules, have been shown to exhibit both rapid response times and high sensitivity to gases, such as nitrous oxide [144]. Finally, given their reduced contact area and weight, they should exhibit reduced in-use stiction [150] and require less power for actuation in MEMS applications.

4.5 Conclusion

We have patterned colloidal, glass, and silicon-based microcomponents via stop-flow lithography. Microcomponents have been created at rates that exceed 10^3 min^{-1} from an index-matched system composed of silica microspheres suspended in a photocurable acrylamide solution. Representative colloidal microgears were fused together at elevated temperatures to yield a dense silica glass or transformed into porous silicon via magnesiothermic reduction. This facile approach offers a new method for micropatterning colloidal, silica, and silicon-based structures for myriad applications, including novel granular media, advanced ceramics, sensors, optical displays, and MEMs devices.

Acknowledgments

This material is based on work supported by the National Science Foundation (DMR-0652424, CTS-0120978 and CTS-0304128). The authors thank A. Deconinck for software development, A. Deconinck, K. Erickson, S. M. Menke, A. Cote and A. Balducci for useful discussions, and M. McConney and S. MacLaren for assistance with AFM.

CHAPTER 5

Tuning Curvature in Flow Lithpgraphy: A New Class of Concave/Convex Particles

This is the final chapter which presents the versatility of stop-flow lithography (SFL) as a platform for the synthesis of complex microparticles. In this chapter our focus is on demonstrating the ability of SFL to add complexity to synthesized microparticles by modifying the shape as opposed to the chemistry which was the goal of Chapters 3 and 4.

One of the biggest limitations of photolithography in general and SFL in particular is the inability to generate 3D particles. The particles synthesized using SFL are 2D extruded particles having straight walls in a direction orthogonal to the projected UV light. In this chapter we present the ability to add curvature in the direction orthogonal to the projected UV light, using SFL. We demonstrate the chemical programmability of this added capability by synthesizing patchy and capped microparticles which can find use in a number of applications such as directed self-assembly.

5.1 Overview

Polymeric particles of complex shapes and chemistry have been used for a wide variety of applications in the materials and bio-engineering fields. An interesting means of introducing complexity is through curvature. In this chapter, stop-flow lithography (SFL) is used to generate concave/convex particles at high-throughputs of 3×10^4 particles per hour. These particles have finely tuned curvature in the plane orthogonal to the plane of projection of light. The shape in the plane of projection of light is determined by the mask shape. The chemical programmability of this technique is further demonstrated by creating multi functional particles i.e., patchy and capped particles. The directed assembly of these particles can find potential application in a variety of fields like biology, photonics and liquid crystals.

5.2 Introduction

Polymeric particles of complex architecture are widely used for applications such as photonic materials [151], MEMS [152], biomaterials [153] and self-assembly [148]. Introducing complexity in particle design is important since particle shape can significantly influence particle function [154]. An important facet of shape complexity is the introduction of curvature. It has been shown by molecular simulations that the curvature of particles can be tuned to regulate assembly as demonstrated by viral assembly [155]. Experimental evidence has also been provided for the preferential standing positions of concavo-convex particles with clear analogy to brachiopod or pelecypod shell orientation in moderately turbulent water [156]. Curvature, both convex and concave, can thus be used to tune assembly of particles [155, 156], leading to breaking of point symmetries (lower symmetries than spherical particles) for photonic materials [157], generation of scaffolds of desired curvature for directing cell internal organization [158] and improved osteoblast performance for significant bone tissue formation [159]. Particles with finely tuned curvature can also be used for facilitating or hindering phagocytosis [160], studying scattering functions of aerosols [161] and acquiring experimental evidence on scattering dependence on concavity for polyhedral ice-crystals for atmospheric science [162]. Furthermore, curved non-spherical particles have applications in cosmetics [163] and can be used for fundamental studies in microfluidics [164] and generation of diverse crystal structures [165]. The synthesis of nonspherical particles and the role of shape anisotropy has been demonstrated by Stroock et al. [166]. Further, work has also been done to demonstrate the synthesis and assembly of structured colloidal particles with control over size, shape and structure and their application in photonics [167, 168, 169]. Lastly, non-spherical particles may also open new applications in advanced materials due to their unique scattering properties [170].

Current approaches to particle synthesis are either nonmicrofluidic batch [171, 138, 93, 172, 173, 34, 33] or continuous [33] processes or microfluidic schemes which are based on two-phase flow [38, 39, 174, 175, 176] or continuous flow-lithography (CFL) [30] and its variant stop-flow lithography (SFL) [48]. SFL is a versatile technique which has been used to generate cell-encapsulated hydrogels [177], ceramic microcomponents [178] and barcoded particles for biomolecular analysis [97]. Another noteworthy microfluidic-based technique for generating complex microparticles forms polystyrene microbeads into higher order assemblies via microfluidic arrangement and thermal fusion [137].

The limitations of batch processes like traditional photolithography include low throughput and the inability to pattern high-resolution features using low-viscosity oligomers. Flow-through microfluidic schemes based on tow-phase flow can be used to generate spherical particles or modifi-

cations thereof, e.g., disks due to surface tension restrictions [39, 40]. These structures are therefore inherently convex. Convex particles have also been generated recently by several groups using non-microfluidic schemes [154, 179]. Traditional photolithpgraphy and CFL/SFL can be used together to create concave architecture using suitably designed masks; however, the structures formed are essentially 2D extruded structures, having straight walls in the direction orthogonal to the projection of light. Techniques for generating truly 3D nonconvex (concave) particles with precise control over particle curvature are therefore needed. The Thomas group recently introduced concave curvature in polymeric particles using holographic interference lithography (HIL) which to the best of our knowledge is the only work of its kind. However, at present, their technique is only capable of creating single chemistry particles [180].

The purpose of this chapter is to tune the curvature (concavity/convexity) in flow lithography and generate a new class of microparticles. The introduction of curvature in the direction orthogonal to the incident light in conjunction with curvilinear photomask geometry gives rise to a new class of microparticles. The importance of introducing curvature in particles can be explained by a simple example related to assembly of these particles: a flat surface generated via photolithography using a mask with a rectangular feature has flat sides with line or point valence of zero. The introduction of concavity of radius R_1 in the plane of UV light on one side or two opposite sides of the rectangular mask introduces a line valence of two and four, respectively. The introduction of concavity with a radius R_2 in the plane orthogonal to the direction of projection of light in addition to R_1 in the plane of light, leads to a point valence of 4 and line valence of 2 or a point valence of 8 and line valence of 0 depending on curvature being introduced on a single side or both sides in the plane orthogonal to projection of light [180]. These three different classes of particles would assemble differently [180], giving entirely unique photonic structures, liquid crystals or scaffolds.

A new class of particles which we call dual curvature in a plane particle can be synthesized by this technique. These are particles which have two radii of curvature (R_1, R_2) cut out from a plane. The addition of this second radius of curvature can be used to modulate the strength of specific interactions. It has been shown that the adhesive strength of non-spherical particles mediated by specific interactions is greater than spherical particles under a linear shear flow [181]. The presence of curvature in 2 orthogonal axes R_1 and R_2 ($R_1 > R_2$) for instance can also be used to selectively isolate particles of a certain size range ($R_2 <$ particle size $< R_1$) from a polydisperse group of particles. This kind of tuning wherein a maximum and a minimum (curvatures in orthogonal axes) can be controlled independently has not been demonstrated in hitherto known particles.

The chemical programmability of this technique is demonstrated by synthesizing Janus, patched and capped polymeric particles. The presence of patches on particles is analogous to valence in atoms and can be used to tune the relative strength and direction of interactions between particles, leading to tuning of the final assembled structures [2]. Capped particles (particles having a cap/brush of a different chemistry) are another interesting addition to the existing class of curved particles that we introduce in this work. Capped particles have potential applications for directed assembly and selective adhesion for example. The ability to pattern curved surfaces can be used to select and isolate molecules of different chemistries from a mixture by putting markers on the patterning or capping fluid.

Table 5.1: *The list of polymerization (P) and tuning (T) fluids used in this chapter.*

Fluid Code	Composition
P1	TMPTA (95 %) + Darocur 1173 (5 %)
P2	PEG-DA (55 %) + Water (40 %) + Darocur 1173 (5 %)
P3	PEG-DA (55 %) + Water (40 %) + Darocur 1173 (5 %) + M-acryl-rhodamine B (0.01 %)
P4	TMPTA (95 %) + Darocur 1173 (5 %) + M-acryl-rhodamine B (0.01 %)
T1	PEG-DA (68 %) + Water (32 %)
T2	Glycerol (85 %) + Water (15 %)
T3	Silicone Oil
C1	PEG-acrylate (65 %) + Water (35 %) + M-acryl-rhodamine B (0.01 %)

5.3 Experimental

5.3.1 Materials

All the particles synthesized in this work are either made from tri(methylol propane) triacrylate (TMPTA, Polysciences) or poly(ethylene glycol) (700) diacrylate (PEG-DA, Sigma Aldrich). The capping fluid (C), contained poly(ethylene glycol) (375) acrylate (PEG-acrylate, Sigma Aldrich). For the experiments involving fluorescence, a solution containing 0.01

5.3.2 Microfluidic Devices and Photopolymerization Setup

Photomasks were designed using AUTOCAD 2005 and sent to CAD Art Services (Poway, California) where they were printed using a high resolution printer. The appropriate mask was then inserted into the field-stop of the microscope and UV light flashed through it from a 100W HBO mercury lamp once the flow was stopped. A filter set that allowed wide UV excitation (11000v2: UV Chroma) was used to filter out light of undesired wavelengths. The devices used in this work were fabricated by pouring polydimethylsiloxane (PDMS, Sylgard 184, Dow Corning) on a silicon wafer containing positive-relief channels patterned in SU-8 photoresist (Microchem). The devices were rectangular channels of two different heights (30 μm or 60 μm) and had a width of 200 μm for the experiments wherein two streams were co-flown, single height (60 μm) and a width of 300 μm for the experiments wherein three streams were co-flown and a single height (50 μm) and a width of 300 μm for the experiments wherein four streams were co-flown. The PDMS devices were sealed to glass slides spin-coated with PDMS to ensure that all four walls of the channel were PDMS. The devices were mounted on an inverted microscope (Axiovert 200, Zeiss) and the formation of microparticles was visualized using a CCD camera (KPM1A, Hitachi). Fluorescent and bright-field images of particles were obtained using a digital camera (Nikon, D-200).

5.3.3 Surface Tension Measurements

Surface tension measurements were carried out using the pendant drop method and a DSA 10 tensiometer (Kruss). Contact angle measurements were carried out using the sessile drop method and the same tensiometer. Advancing contact angle was measured for a drop of liquid on a clean PDMS slab.

5.3.4 Particle Recovery and Characterization

The particles were collected in the reservoir of the microchannel and washed three times using ethanol. For fluorescent experiments the particles in the reservoir were washed with ethanol ten times, pipetting ethanol in and out and thus mixing the contents of the reservoir, in each wash. Images of the polymeric particles were saved at different points in the reservoir and 35 particles from these images were used for calculating the COV. These particles were then pipetted out using ethanol solution and collected in an eppendorf tube. The eppendorf tube was centrifuged to allow the particles to settle down, the supernatant removed, new ethanol added and the contents vortex mixed. This procedure of centrifugation, removing supernatant (ethanol), adding new ethanol and vortex mixing the contents was repeated three times to obtain a collection of the particles suspended in clean (oligomer free) ethanol.

5.4 Results and Discussion

A schematic diagram of the setup is shown in Figure 5.1A. A photocurable solution which we call the polymerization fluid (P) and a non-photocurable solution, named tuning fluid (T), are co-flowed and then stopped. Curvature develops at the interface of the two fluids which depends on the surface energies of the P, T and the walls of the microchannel. The quiescent fluids are exposed to a flash of UV light through a photomask. The region of the P exposed to the UV light is polymerized while T is an inert (non-polymerizing) fluid. This leads to the generation of a polymeric particle having a shape in the plane of projection of light determined by the mask and a curvature in the plane orthogonal to the plane of light determined by three parameters: a) the surface energies of the P and T, b) the surface energies of the bottom and top wall of the microchannel and c) the height of the channel. The particles are then flushed out of the channel and collected in a reservoir at the end of the channel.

The curvature is illustrated in Figure 5.1B. The radius of curvature (R) and the maximum deformation (D_{max}) for a channel of height H are given by:

$$R = \frac{H}{2cos(\beta)} \tag{5.1}$$

$$D_{max} = \frac{H\,[1 - sin(\beta)]}{2cos(\beta)} \tag{5.2}$$

A simple force balance can be used to evaluate $cos(\beta)$ using the equation

$$\gamma_{PT} cos(\beta) = \gamma_{TS} - \gamma_{PS} \tag{5.3}$$

where γ_{PT} is the interfacial tension between the T and P and γ_{TS} and γ_{PS} are the solid-liquid interfacial tensions between PDMS (S) and the T and P respectively. The right-hand side of Equation 5.3 can be evaluated by conventionally measurable properties like the contact angle of the T and P on a PDMS surface surrounded by air and the surface tensions of pure T and P

$$\gamma_{TS} = \gamma_{AS} - \gamma_{TA} cos(\theta_T) \tag{5.4}$$

$$\gamma_{PS} = \gamma_{AS} - \gamma_{PA} cos(\theta_P) \tag{5.5}$$

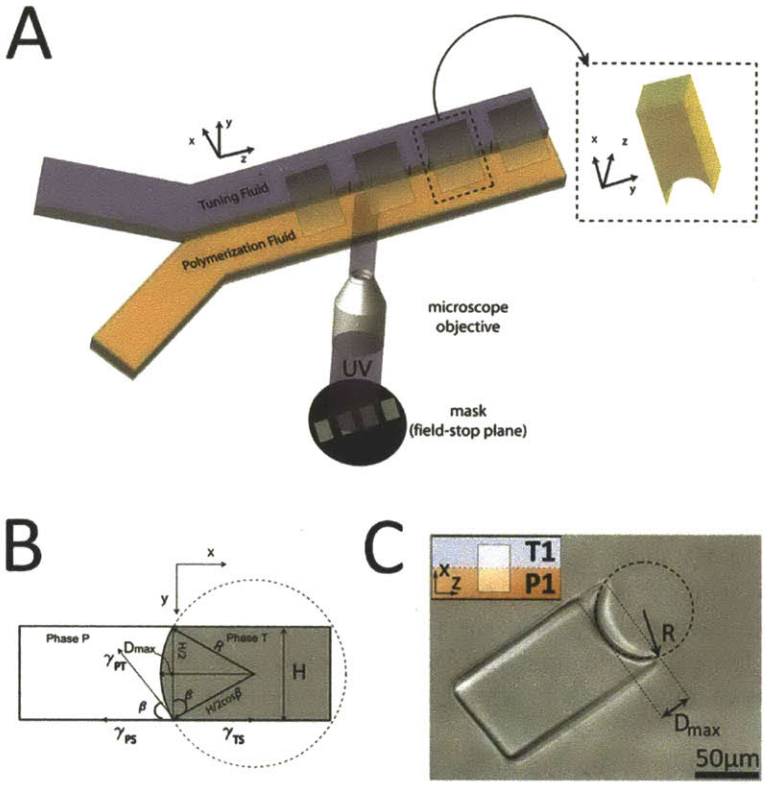

Fig. 5.1: *(A) Schematic illustration of concave particle synthesis using stop flow lithography (SFL) system. Photocurable solution (polymerization fluid) and tuning fluid are co-flowed and then stopped. Depending on the relative surface energies, curvature develops at the interface between the immiscible fluids (inset). Ultraviolet light is then projected through a mask, solidifying polymeric particles having the shape on the x-z plane determined by the mask and the shape in the x-y plane determined by the equilibrium curvature. The section of the tuning fluid exposed to UV light does not get polymerized. (B) A schematic showing the cross section of the microfluidic device and the radius of curvature (R) and maximum deformation (D_{max}) of the particles on the x-y plane. (C) Differential interference contrast (DIC) image of the cross-sectional view of the curvature of a TMPTA particle. The particle was synthesized in a 60 μm tall channel.*

Table 5.2: *Experimentally obtained values of the parameters used in Equations 5.7 and 5.8.*

Polymerization Fluid	Tuning Fluid	γ_{PA}	γ_{TA}	γ_{PT}	θ_{PA}	θ_{TA}
TMPTA	T1	32.59 +/- 0.26	40.91 +/- 0.02	7.35 +/- 0.02	51.0^o	70.4^o
TMPTA	T2	32.59 +/- 0.26	50.46 +/- 0.08	14.20 +/- 0.07	51.0^o	82.3^o

Table 5.3: *Comparison between estimated and experimentally obtained curvatures. [a] Height of the channel (μm). [b] Measured radius of curvature (μm). [c] Estimated radius of curvature (μm). [d] Measured maximum deformation (μm). [e] Estimated maximum deformation (μm).*

Polymerization Fluid	Tuning Fluid	$H[a]$	$R_m[b]$	$R_e[c]$	$D_{max,m}[d]$	$D_{max,e}[e]$
TMPTA	T1	60	32.5 +/- 1.3	32.6	19.7 +/- 2.2	19.9
TPMTA	T2	60	31.5 +/- 1.2	31.0	23.0 +/- 1.3	23.1
TMPTA	T1	30	16.9 +/- 0.9	16.3	9.2 +/- 0.2	10.0

where γ_{AS} is the surface tension of the PDMS surface and γ_{TA} and γ_{PA} are the surface tensions of T and P respectively. θ_T and θ_P are the contact angles of the T and P respectively. Subtracting Equation 5.5 from Equation 5.4 we attain

$$\gamma_{TS} - \gamma_{PS} = \gamma_{PA}cos(\theta_P) - \gamma_{TA}cos(\theta_T) \tag{5.6}$$

Using Equations 5.1, 5.3 and 5.6, we get

$$R = \frac{H\gamma_{PT}}{2\left[\gamma_{PA}cos(\theta_P) - \gamma_{TA}cos(\theta_T)\right]} \tag{5.7}$$

$$D_{max} = R\left[1 - sin(\beta)\right] = \frac{H\gamma_{PT}\left[1 - sin(\beta)\right]}{2\left[\gamma_{PA}cos(\theta_P) - \gamma_{TA}cos(\theta_T)\right]} \tag{5.8}$$

We investigated the predictability of the curvature (R and D_{max}) by varying two of the three tuning parameters i.e. the tuning fluid and the height of the channel. The values for the different parameters used in Equations 5.7 and 5.8 for the two Ts used are reported in Table 5.2 and the comparison between the experimentally measured (using 35 particles) and theoretically estimated R and D_{max} are reported in Table 5.3. Figure 5.1C shows an example of particle R and D_{max} measured experimentally. It can be seen from Table 5.3 that the theoretically predicted curvatures are in excellent agreement with experimentally obtained values with the maximum deviation in R and D_{max} being 3.7

We quantified the monodispersity of the particles obtained with respect to the curvature in the plane orthogonal to the direction of projection of light, using the batch of particles obtained for Figure 5.1C. The coefficient of variation (COV) in the radial direction was found to be 4 % using a sample of 35 particles. We have previously ascertained that the COV for our particles along the plane of projection of light is less than 2.5 % [96]. We can therefore conclude that the particles generated by this technique are monodisperse since the COV < 5 % [182]. We were able to obtain a throughput of $\sim 3 \times 10^4$ particles per hour for these particles, using a mask having 7

rectangular features in a row, using typical stop, polymerization and flow times of 100, 60 and 600 ms respectively.

5.4.1 Choosing the Tuning and Polymerization Fluids

Having established the physical parameters for the tuning of curvature, we ascertained the pair of Ts and Ps to be used for synthesizing curved polymeric particles to demonstrate both the materials flexibility and the tuning of curvature. The materials flexibility is demonstrated by making TMPTA (hydrophobic) and PEG-DA (hydrophilic) particles. When selecting a T we ensured that it was inert and the T and P do not flip over. Flipping over is the process in which a gravity-induced pressure mismatch at the interface gradually drives the denser fluid to occupy the lower portion of the microchannel. The rate of this process depends on the interplay between the viscous forces which tend to dominate at the microscale and the gravitational forces [183]. While density mismatch favors the flipping over of the fluids, viscous forces favor co-flow and dampen the propensity to flip over. In our case, since the T and P are immiscible, in addition to the viscous and gravity forces, the surface forces need to be accounted for. For channels of aspect ratio 1, interfacial force attenuates the effect of gravity [184]. A glycerol-water mixture, 85 % (v/v) glycerol (ρ = 1.22 g/cc), was chosen as the T for generating concave TMPTA (ρ = 1.12 g/cc) particles. Due to the high viscosity of these solutions ($\sim$ 106 cP), the interface does not flip over in spite of the density mismatch. Mineral oil (ρ = 0.8 g/cc), corn oil (ρ = 0.9 g/cc), PDMS (ρ = 0.98 g/cc) and silicone oil (ρ = 1.05 g/cc) were tried as potential Ts for generating PEG-DA particles. For mineral oil, corn oil and PDMS, the density mismatch with PEG-DA (ρ = 1.12 g/cc) and low viscosities led to distorted interfaces. Silicone oil was chosen as the T due to closer density to PEG-DA. A diluted PEG-DA solution (40 % water) was used as the P. The increased hydrophilicity due to the dilution by water accentuated the convex curvature. The Ps and Ts used in this article are listed in Table 5.1.

5.4.2 Classification Scheme

Concave/convex particles were synthesized using different masks as shown in Figure 5.2. The simplest classification scheme for these particles is based on the number of faces, line valences and point valences present in the particle in the planes orthogonal to the plane of projection of light [180]. The illustration in Figure 5.3 demonstrates the transition from a flat surface (Figure 5.3A) to a two line valence (Figure 5.3B) and four point valence (Figure 5.3C) structures by the successive addition of one and two curvatures respectively.

5.4.3 Concave Particles

Figure 5.2A demonstrates the generation of a structure with two line valences from a triangular mask feature. Traditional photolithography would generate a structure with a line valence of zero. A circular mask feature is of considerable interest as a circle is a closed figure with zero corners. Figure 5.2B demonstrates the use of a circular mask feature which forms a structure with two line valences, along the edge parallel to the interface of the co-flowing fluids and having concavity and convexity in orthogonal planes. Figure 5.2C demonstrates the generation of a structure with one line valence and four point valences by using a mask feature with three curved edges, one of them, aligned parallel to the interface between the co-flowing fluids. It also shows the generation of a

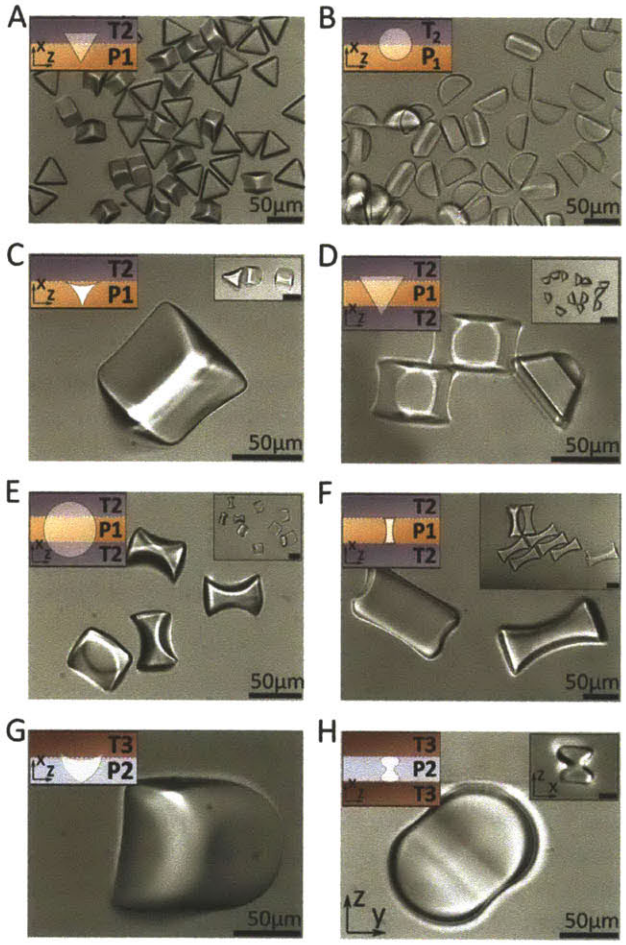

Fig. 5.2: *DIC images of curved particles of single chemistry. The particles have curvature in the direction orthogonal to the direction of projection of light. The schematic at the top left hand corner of the images, shows the mask feature and the fluids used (Table 5.1). (A) Concave triangles generated in a 60 µm tall channel, (B) concave half-discs generated in a 30 µm tall channel, (C) particles with three concave edges in the plane of projection of light and a concave edge in the plane orthogonal to the plane of projection of light (dual curvature in a plane structure). (D, E and F) Concavo-concave particles generated using a 60 µm tall channel and a triangular, circular and distorted rectangle mask feature respectively. (G) Convex particles generated using a 60 µm tall channel demonstrating the same duo curvature along a plane structure but the curvatures being concave-convex. The image shows the convex curvature imposed on the concave curvature which is visible only at the center of that edge where the radius of concavity in the plane of projection of light is greater than the convexity in the plane orthogonal to the plane of projection of light. (H) Convexo-convex particles generated in a 60 µm tall channel using a distorted rectangular mask feature having opposite edges defined by the Chebyshev polynomial of first kind and fourth order. (A-F) are TMPTA particles while (G-H) are PEG-DA particles.*

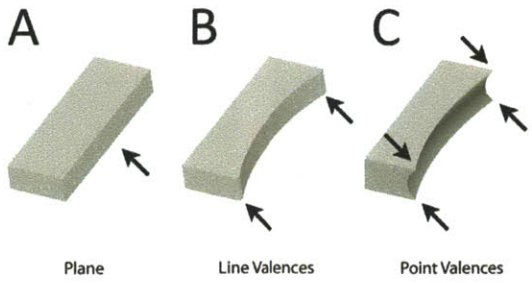

Fig. 5.3: *Illustration demonstrating the transition from a flat surface (A) to two line valence (B) and four point valence (C) structures by the successive addition of one and two curvatures respectively.*

hollow structure with two radii of curvature along orthogonal directions (dual curvature in a plane particle).

5.4.4 Concavo-concave Particles

Figure 5.2D shows the formation of a concavo-concave structure with four line valences using a triangular mask feature. Figure 5.2E shows the generation of a particle with four line valences having convexo-convex and concavo-concave structures on orthogonal planes. Figure 5.2F demonstrates the use of a four cornered mask feature aligned with two opposite edges parallel to the two interfaces of the P and the Ts. The particle has concavo-concave curvatures on orthogonal planes. Furthermore, due the alignment of the straight edges along the interface, it gives rise to a particle with four line valences. The alignment of the curved edges along the interface of the P and the Ts would have given rise to a structure with eight point valences and two faces.

5.4.5 Convex and Convexo-convex Particles

The materials flexibility is demonstrated by generating convex and convexo-convex PEG-DA particles as shown in Figure 5.2G and 5.2H respectively. The particles in Figure 5.2G had the concave edge aligned along the interface of the two fluids (illustration Figure 5.2G) and thus a polymeric particle with one line valence and 4 point valences was generated. This particle has a concave and convex edge along orthogonal planes cut out from a plane i.e. demonstrates a dual curvature in a plane particle. Figure 5.2G shows the convex curvature superimposed on the concave curvature, which is visible only at the center of that edge, where the radius of concavity in the plane of projection of light is greater than the convexity in the plane orthogonal to the plane of projection of light. The structures generated until this point demonstrated the use of straight lines or simple curvatures (concave or convex) along the edge of the n-cornered mask feature. Figure 5.2H shows the use of a polynomial (Chebyshev polynomial of the first kind and fourth order) [185] as two opposite edges in a distorted rectangular mask feature. The mask had two straight edges which were aligned along the two interfaces of the Ts and the P and two curved edges (defined by the

Chebyshev polynomial) along the other opposite edges. The polymeric particle thus formed is a Chebyshev particle with four line valences.

5.4.6 Multifunctional Particles

Janus particles with convexity in the polymerization plane on the PEG-DA part and concavity in the plane orthogonal to the projection of light on the TMPTA part are shown in Figure 5.4A. These particles have alternate curvatures in perpendicular plains on two different chemistries. Similarly, Figure 5.4B demonstrates the ability to create concave and convex architecture in a plane orthogonal to the direction of projection of light in the same particle, the curvatures being on different chemistries, PEG-DA (convex) - TMPTA (concave). These particles can be synthesized using SFL (shown only for easy imaging and visualization). A triangular feature on a mask was used to generate convexo-concave particles shown in Figure 5.4C.

5.4.7 Patterned Chemistries

The chemical programmability of this technique was demonstrated by making patchy and capped particles. The essential difference between patchy and capped particles lies in the properties of the fluid used for generating the pattern. The P used for creating a patch is a cross-linkable oligomeric fluid (multi-functional, diacrylate for instance) with photoinitiator. On exposure to UV light, free radicals are generated due to the presence of the photoinitiator and the diacrylate cross-links to form a gel. The capping fluid (C) on the other hand is a polymerizable but non-cross-linkable oligomeric fluid (mono-functional, mono-acrylate for instance) with no photoinitiator. When C is exposed to UV light, free radicals are not generated in the bulk fluid due to the absence of photoinitiator. However, the co-flowing P undergoes gelation on exposure to UV light. Free radicals at the $P - C$ interface can lead to polymerization of the oligomer in C which results in a linear polymer that is attached by one end to the particle created in the P solution. The resulting structure will be a thin polymer brush on the curved face of the particle.

We generated patchy particles having PEG-DA patches on TMPTA particles and the inverse TMPTA patches on PEG-DA particles as shown in Figures 5.4D and 5.4E respectively. The TMPTA particles have four TMPTA faces and two opposite faces having a curved PEG-DA patch as shown in Figure 5.4D while, PEG-DA particles have two opposite PEG-DA faces, two opposite PEG-DA faces with a thin TMPTA region having a straight interface with PEG-DA and two opposite PEG-DA faces having TMPTA corners as shown in Figure 5.4E. These patchy particles are unique to our technique.

We generated capped/polymer brush TMPTA particles by co-flowing a mixture of TMPTA-Darocur 1173 with PEG-acrylate solution and exposing to a flash of UV light through a rectangular mask feature as shown in Figure 5.4F. The polymeric caps/brushes can either act as a facilitator for directed assembly of particles containing dissimilar chemistry or as a barrier for some specific molecules. The shape concavity can also allow particles with a radius smaller than the radius of the concave curvature to interact with the capped surface, sequestering particles of bigger radius of curvature. Further, two different capping fluids can be used to pattern the two concave curvatures along the plane orthogonal to the plane of projection of light. These particles can be used to selectively adhere to specific sites using one of the caps/patterns and to selectively repel specific molecules using the other cap/pattern. This might be important in avoiding phagocytosis of directed drug delivery systems [160].

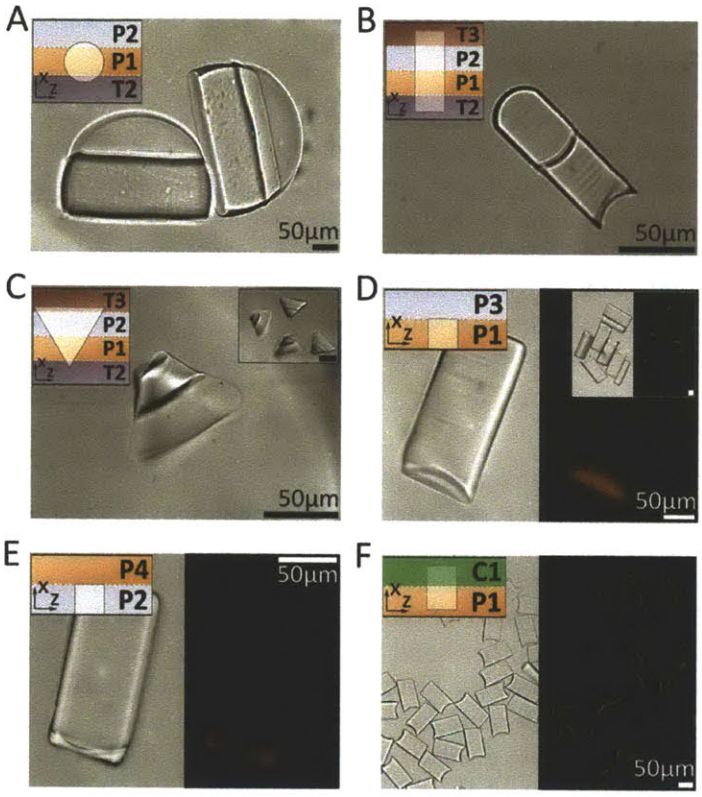

Fig. 5.4: *DIC images of curved particles containing multiple chemistries. The particles have curvature in the direction orthogonal to the direction of projection of light. The schematic at the top left hand corner of the images, shows the mask feature and the fluids used (Table 5.1). (A) Concave Janus half-discs made from PEG-DA and TMPTA depicting curvature in two different chemistries in orthogonal axis. (B and C) Concavo-convex particles containing two chemistries (PEG-DA and TMPTA). (D) Bright field and fluorescence image of patchy particles having PEG-DA patch on TMPTA particles. The PEG-DA region contains rhodamine acrylate and hence glows red in the fluorescence image while the TMPTA part is not fluorescent. (E) Bright field and fluorescence image of patchy particles having TMPTA patch on PEG-DA particles. The TMPTA region contains rhodamine acrylate and hence glows red in the fluorescence image while the PEG-DA part is not fluorescent. (H) Bright field and fluorescence image of capped particles containing PEG acrylate cap on concave TMPTA particles. The PEG-acrylate caps contain rhodamine acrylate.*

5.4.8 Defining the Phase Space of Particles Generated using this Technique

Theoretical description of a new class of particles is a daunting task. A plausible route to classifying a new class of particles is the division of the phase space of synthesized particles into anisotropy axis [2]. We divided the phase space of particles generated in this work into 5 anisotropy axis, i.e. non-rectangular feature on mask, concave, convex, chemistry and patch. The coordinates along the non-rectangular feature on mask axis are 0 or 1, depending on the presence or absence of a rectangular feature on the mask respectively. Similarly, the coordinates on the concave and convex axis are 0, 1 or 2 depending on the absence or presence on one side or both sides of curvature along the axis orthogonal to the projection of light. The coordinates on the chemistry axis are natural numbers depending on single, double or multiple chemistries used in the particle. Finally, coordinates on the patchy axis are 0, 1 or 2 depending on the absence or presence of patch on one or both sides of the particle on the axis orthogonal to the plane of projection of light. Capped particles are a special variant of patchy particles with the presence of a layer instead of patch on one or both sides of the polymeric particle. For illustrative purposes, the particle in Figure 5.1C would have a coordinate of (0,1,0,1,0), i.e. rectangular feature on mask, concave curvature created in the plane orthogonal to the projection of light on one side, convex curvature in the plane orthogonal to the projection of light on no sides, single chemistry and patchiness on no sides. Similarly, the particles in parts A, E and H of Figure 5.2 would have coordinates of (1,1,0,1,0), (1,2,0,1,0) and (1,0,2,1,0) respectively. Some particles in Figure 5.4 for instance parts A, C, E and F would have coordinates of (1,1,0,2,0), (1,1,1,2,0), (0,0,0,2,1) and (0,1,0,2,1) respectively. Having thus divided the phase space of the particles generated by this technique, we can say that particles having 1 as the first coordinate, i.e. particles generated by non-rectangular mask feature, and anything else on the other 4 coordinates are novel and unique to this technique. Furthermore, not all particles having the first coordinate 0 are synthesizable by traditional photolithography or SFL. The presence of patchiness, i.e. 1 or 2 in the fifth coordinate gives rise to a class of particles which are novel and unique to this technique.

5.5 Conclusion

In conclusion, we have demonstrated a facile process for the synthesis of polymeric particles of different chemistries (both hydrophobic and hydrophilic) with finely tuned curvature along the plane orthogonal to the plane of projection of UV light. The fluid interfacial properties and channel height are used to tune the curvature. The dependence of the curvature on these parameters has been mathematically derived and experimentally verified. We have further demonstrated the chemical programmability of this process by the synthesis of patchy and capped particles. Curvature can be used to tune the assembly of these particles giving rise to macrostructures suitable for applications in biology; for instance for the generation of scaffolds of desired curvature for directing cell internal organization [158] and for improving osteoblast performance to aid tissue formation in bones [159]. Furthermore, the tuned assembly of these particles can be exploited for novel material synthesis for applications in a variety of other fields like photonics, liquid crystals and optics. Particles with curvature can be used to model the wealth of microscale shapes in nature, be it bacteria, platelets or erythrocytes. They can also be used in new applications in advanced materials, which take advantage of their unique scattering properties as well as precise control over shape and size.

Acknowledgments

This material is based on work supported by the Singapore-MIT Alliance (SMA-2, CPE Program). The authors thank A. Balducci and D. C. Pregibon for useful discussions.

CHAPTER 6

Tuning Rotation of Anisotropic Particles in a Uniform Magnetic Field

In this chapter, we present a framework for the study of field-directed assembly of magnetic hydrogels. We begin by demonstrating the ability to synthesize magnetic hydrogels with encapsulated 800 nm beads using stop-flow lithography (SFL). We realized that the assembly of magnetic microparticles, at low to moderate surface coverages, involves two time steps: i) rotation to attain an equilibrium orientation, and ii) translation to attain the final assmbled structure. Therefore, as a first step to understanding the assembly of H-shaped microparticles, we investigate the dependence of the equilibrium orientation of these particles on geometric parameters intrinsic to the shape. We use the results obtained to design H-shaped particles which would have a higher propensity to assemble into macrostructures with branched networks and study their assembly.

It has been demonstrated that the properties of magnetorheological (MR) fluids can be tuned by using anisotropic particles. However, only simple shapes like rods and plate-like, have been used till date. We present results for the assembly of complex (H-shaped) particles which might be useful in tuning the microstructure and hence the macroscopic properties of MR fluids. I collaborated with Ki Wan Bong and Matt Helgeson, from the Doyle group for this work.

6.1 Overview

The directed assembly of shape anisotropic magnetic particles into targeted macrostructures requires judicious particle design. H-shaped particles are an intriguing class of shapes to study since they should give rise to branched networks. In this work, we present a framework to understand the self-assembly of non-Brownian H-shaped particles. As a first step towards understanding the self-assembly of these particles, we study their field-directed rotation. We develop a Finite Element Integration (FEI) method to identify the preferred particle orientation (relative to the applied field) at different values of the geometric parameters defining H shapes, and construct a phase diagram to generalize the results. Theoretical predictions are validated by comparing with experiments performed using magnetic hydrogels synthesized using stop-flow lithography (SFL). We use the results obtained from the rotation study to select one subset of H-shaped hydrogels for assembly. We demonstrate the ability of H-shaped particles to induce chain growth orthogonal to the field, and branching. The assembly of a suspension containing H-shaped particles, rods, or a combination of both is also investigated.

6.2 Introduction

Colloids used in electrorheological (ER) and magnetorheological (MR) fluids have primarily been spherical in shape due to ease of synthesis and ready availability. The macroscopic properties of MR fluids depends on the microstructure formed on applying a magnetic field [186, 187, 188], and thus structures formed by ER and MR fluids composed of spherical field-responsive colloids under different conditions have been the topic of many studies (see Ref. [189] for a recent review). Field-responsive shape-anisotropic particles, specifically rod-shaped particles, have been shown to form stronger ER [190, 191, 192, 193, 194] and MR [195, 196, 197, 198, 199] fluids as well as to provide better stability against sedimentation and easy re-dispersion [194, 195, 196, 197, 199]. Hence, the focus of many recent studies has been to tune the properties of ER and MR fluids by designing anisotropic particles [189] although the study of rotation and assembly of anisotropic field-responsive particles and the structures they form, is nascent [2]. Studies have been reported wherein electric/magnetic fields have been used to assemble "shape" [200, 201, 202, 203, 204, 205, 206] "chemically" [207, 208, 209, 210, 211, 204] and "both shape and chemically" [206] anisotropic field-responsive particles. The studies with shape anisotropic particles have considered rods [212, 213, 198, 199], ellipsoids [202, 214], peanuts [201, 215], cubes [200], hexnut and boomerang shapes [203], chiral plates [216], toroids [204], blocks [205] and triangles [206] wherein the particles form either chains or dense clusters under an applied magnetic field.

Both spherical and anisotropic (rod-shaped) particles used in MR fluids form chains under an applied magnetic field at low concentrations. Widening of these chains in a direction orthogonal to the applied field (column formation) occurs at higher concentrations [199]. The formation of columns has been reported as the reason for enhanced ER and MR performance for whisker-shaped [193] and rod-shaped [198] particles respectively. A simple shape that can potentially promote such chain widening and formation of branched networks at low particle concentrations is an H shape (Figure 6.1). When mixed with MR spheres, one might envision that each vertical arm of the H could be integrated into separate linear chains, with the horizontal arm of the H acting to bridge the chains. Thus more broadly, H shapes can be visualized as microparticle analogues to cross-linkers in polymer chemistry. They could be used to vary network topology and the resulting

mechanics in MR suspensions.

Two distinct motions occur during the assembly of anisotropic field-responsive particles: rotation and translation [217]. These motions are associated with characteristic time scales: a rotational time scale given by the time required for a single isolated anisotropic particle to rotate into an equilibrium orientation, and the translational time scale for center of mass movement driven by particle-particle interaction given by the time required for particles to form assembled structures with neighboring particles. It is clear from Figure 6.1 that the network topology would depend on the equilibrium orientation of H-shaped particles. Hence, a clear understanding of the equilibrium orientation attained by anisotropic particles is essential for further studies on their assembly.

There has been a longstanding interest in orienting anisotropic field-responsive biological entities. The equilibrium orientation of cells has been of interest for studies that focus on their directed motion [218, 219] or to create engineered heart tissue with preferential orientation [220]. Furthermore, living species such as magnetotactic bacteria are known to swim along magnetic field lines [221, 222] by arranging intracellular organelles containing magnetic crystals called magnetosomes into chains which align in the direction of the field lines [222]. The living entities considered in the aforementioned studies can be modeled as ellipsoidal or rod-like particles. As opposed to rods or ellipsoids which orient along their primary axis under a uniform magnetic field [212, 214, 217, 219, 220, 222, 223], the equilibrium orientation of more complicated shapes is non-trivial and depends on the geometric parameters defining the shape. In the current study, we use low concentrations of H-shaped particles, at which they translate into contact with each other only after attaining their equilibrium orientation. Thus, we can isolate and study their preferred orientation as a function of geometric shape parameters (Figure 6.1).

In this work, we study the dependence of the equilibrium orientation of non-Brownian H-shaped magnetic hydrogels on geometric parameters using both numerical techniques and experiments. We further simplify the system by considering particles which are confined to rotate in plane. Experimentally, a quasi-2D suspension is realized by fabricating large dense particles which readily sediment to the bottom of the observation chamber. Applying the magnetic field tangent to the focal plane allows us to monitor accurately particle rotation. We begin by describing the Finite Element Integration (FEI) technique, followed by presenting the FEI predictions in the form of a phase diagram through which we show that the rotation of H-shaped particles can be tuned by geometric parameters in a non-trivial manner. The predictions are then validated by experiments using magnetic hydrogels synthesized using stop-flow lithography (SFL) [30]. SFL is a versatile technique which has been used to generate cell-encapsulated hydrogels [177], ceramic microcomponents [178], curved 3-D particles [224] and barcoded particles for biomolecular analysis [97]. The flow in a deformed PDMS channel has also been studied previously [225] and gives insights into the stop times required for the synthesis.

We use the results obtained from the rotation study to design experiments to test the ability of H-shaped particles to assemble into wide (orthogonal to the field) chains. We performed assembly experiments using a mixture of rods and H-shaped particles at a low total surface coverage. We investigate the effect of varying the fraction of H-shaped particles on orthogonal chain growth. Finally, we show that chain growth orthogonal to the field can occur via two modes: branching and meandering, and quantify branching.

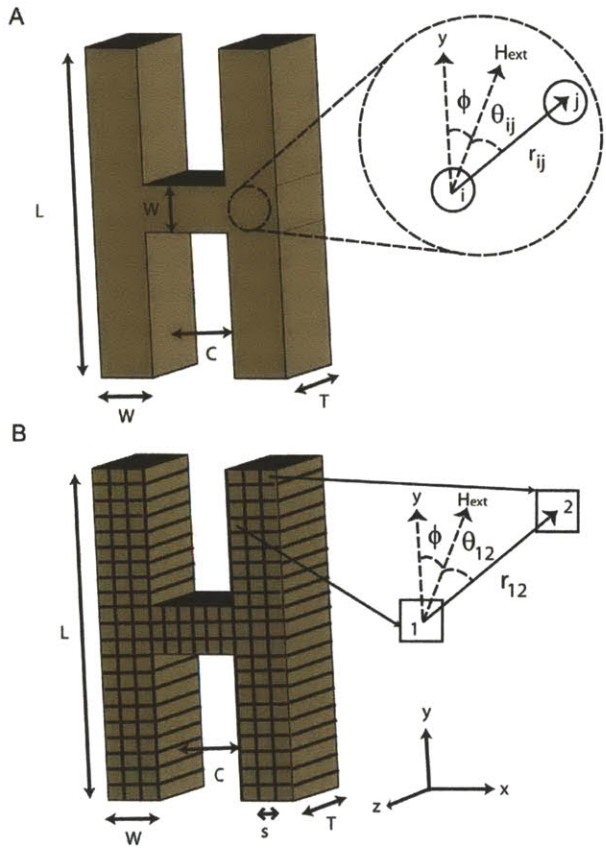

Fig. 6.1: *A) Schematic for a 2D extruded H-shaped particle. The particles are made up of a homogeneous distribution of magnetic beads as represented by i and j. The angle made by the vector joining the center of the beads i and j with the magnetic field vector is given by* θ_{ij} *B) H shapes are divided into cuboidal meshes of size s along both the x and y axis and T along the z axis for evaluating the energy using FEI. FEI involves summing the interaction energies between all the mesh elements. The angle (orientation) made by the magnetic field with the y axis is denoted by* ϕ *where* ϕ *can take values from* 0^0 *to* 90^0.

6.3 Theory and Modeling

In this study, we use non-Brownian 2D extruded H-shaped magnetic hydrogels with encapsulated nanometer sized beads (Figure 6.1). The H-shaped particles are comprised of two vertical rods of length and breadth L and W, respectively, connected to each other by a horizontal rod of length and breadth C and W, respectively. At the nanoparticle loadings used in the experiments, the mean nanoparticle separation is much smaller than the microparticle feature sizes. Hence, we can assume a homogeneous distribution of beads in our H-shaped hydrogels. We simplify our system further by modeling our 2D extruded particles as quasi-2D particles of thickness T where T is small compared to the other geometric parameters of the H shape (Figure 6.1). It can be shown that the orientation with minimum energy for a quasi-2D particle would be the same as for our 2D extruded particles (see Appendix). We divide the H-shaped magnetic hydrogel into cuboidal meshes of size s along both the x and y axis and T along the z axis, having a constant magnetization M. We treat the mesh elements as point dipoles placed at the centers of the meshes (Figure 6.1B). The energy of interaction between mesh elements $(1,2)$ is then given by

$$U_{12} = \frac{\mu_o}{4\pi} \frac{\boldsymbol{m}_1 \cdot \boldsymbol{m}_2 - 3(\hat{\boldsymbol{r}}_{12} \cdot \boldsymbol{m}_1)(\hat{\boldsymbol{r}}_{12} \cdot \boldsymbol{m}_2)}{r_{12}^3} \tag{6.1}$$

where μ_o is the permeability of free space, $\boldsymbol{r}_{12}$ is the vector connecting the centers of mesh elements 1 and 2, $\boldsymbol{m}_1$ and $\boldsymbol{m}_2$ are the dipole moments of mesh elements 1 and 2 respectively and $\hat{\boldsymbol{r}}_{12}$ is the unit vector in the r_{12} direction. The magnitude of the dipole moment of each mesh element is given by

$$m = VM \tag{6.2}$$

where M is the volumetric magnetization of the hydrogel and V is the volume of the mesh element. The magnetization of the hydrogel (M) depends on the weight fraction of beads encapsulated in the hydrogel and can be determined experimentally. The saturation magnetization of the hydrogel is equal to the product of the weight fraction of beads encapsulated in the hydrogel and the saturation magnetization of the beads. The direction of the dipole moment of a mesh element is the same as that of the magnetic field $\boldsymbol{H}$ acting on the hydrogel. We further assume that the dipole moment of a mesh element is not influenced by the dipole field of surrounding mesh elements for low magnetic fields [226]. Thus, the magnetic field experienced by mesh element 1 is given by

$$\boldsymbol{H}_1 = \boldsymbol{H}_{ext} \tag{6.3}$$

where $\boldsymbol{H}_{ext}$ is the external magnetic field applied. The dipolar interaction energy between mesh elements using the above approximations is given by

$$U_{12}(r_{12}, \theta_{12}) = \frac{m^2 \mu_o}{4\pi} \left(\frac{1 - 3cos^2\theta_{12}}{r_{12}^3} \right) \tag{6.4}$$

The energy of a quasi-2D shape of thickness T is given by the sum of the interactions between all the mesh elements in the hydrogel. The nondimensionalized energy obtained using Equations 6.2 and 6.4 is given by

$$E_\phi = \frac{U_\phi}{\frac{M^2T^2L\mu_o}{8\pi}} = \kappa^4 \sum_{\Omega} \frac{(\frac{x_2-x_1}{L})^2(1-3sin^2\phi) + (\frac{y_2-y_1}{L})^2(1-3cos^2\phi) - 6(\frac{x_2-x_1}{L})(\frac{y_2-y_1}{L})sin\phi cos\phi}{[(\frac{x_2-x_1}{L})^2 + (\frac{y_2-y_1}{L})^2]^{5/2}} \quad (6.5)$$

where (x_1, y_1) and (x_2, y_2) are the centers of the mesh elements and $\kappa = s/L$ is the nondimensionalized mesh size. Finite Element Integration (FEI) involves summing the interaction energy between each of the mesh elements as shown in Equation 6.5.

We varied ϕ from 0^0 to 90^0 and evaluated the energy using FEI for typical H shapes as shown in Figure 6.2. We found that the minimum energy was for 0^0 (vertical, looks like an H aligned in the direction of the magnetic field), 90^0 (horizontal, looks like an I aligned in the direction of the magnetic field) or that all ϕ were of the same energy (Figure 6.2). Hence, in our larger sweep of parameter space we compared the energies in the 0^0 (E_0) and 90^0 (E_{90}) orientation to determine the preferred orientation (when $E_0 \neq E_{90}$) or the phase boundary (defined by $E_0 = E_{90}$).

The energy given by Equation 6.5 diverges as $O(1/\kappa)$ in the limit of $\kappa \to 0$ (compare with rod, Appendix) since in a 2D lattice the number of terms in the summation grows like $1/\kappa^2$ (nearest neighbors) and $1/r^3 \sim 1/\kappa^3$. The beads encapsulated in a magnetic hydrogel have a physical volume with a diameter d. Comparing our model with the magnetic hydrogel, d sets a physical minimum for the mesh size and hence rectifies the divergence seen in the model. Furthermore, we use non-Brownian H-shaped particles in our study so that the magnetic energy is the only important energy scale. We showed that $E \times \kappa$ converges, for two values of W/L and three values of C/L in both the 0^0 (Appendix) and 90^0 orientation.

In order to make our calculations independent of the mesh size, we scaled E_0 and E_{90} by the energy of a square and plotted the scaled difference to construct the phase diagram shown in Figure 6.3. A square-shaped particle has no preferred orientation, i.e. has the same energy in all orientations (Figure 6.2), and hence can be used to scale both E_0 and E_{90}. We also performed off-lattice Monte-Carlo (MC) simulations for our particles and compared the results with the predictions by FEI (Appendix).

6.4 Finite Element Integration (FEI)

We use the FEI method to evaluate the energy of an H-shaped particle in different orientations. The energy diverges as $O(1/\kappa)$ in the limit of $\kappa \to 0$. The product of the energy with κ converges and the decrease in this product is less than 10% as we decrease κ from 0.010 to 0.007 (see Appendix). Furthermore, the computation time increases as $1/\kappa^4$. Therefore, for numerical convenience we elected to use a κ of 0.007 (with a reasonable computation time of $\sim$ 30 minutes) to evaluate the energy of an H-shaped particle in any orientation. We demonstrated that the phase boundary is invariant to the choice of κ by varying κ over an order of magnitude from 0.0167 to 0.0017 (see Appendix). The interaction energies between all the mesh elements were summed using MATLAB.

6.5 Experimental Section

6.5.1 Materials

All particles used in this work were synthesized from 35 % poly(ethylene glycol) (700) diacrylate (PEG-DA, Sigma Aldrich), 5 % Darocur 1173, and 60 % 800 nm magnetic bead solution (Seradyn Inc., carboxylate-modified, 5 % solids).

6.5.2 Stop Flow Lithography

Photomasks of H shapes with desired geometric lengths were designed using AutoCAD 2005 and printed using a high resolution printer at Fine Line Imaging (Colorado Springs, CO). The mask was inserted into the field stop of the microscope and UV light flashed through it using a Lumen 200 (Prior). A filter set that allowed wide UV excitation (11000v2: UV, Chroma) was used to filter out light of undesired wavelengths. Microfluidic devices, made of PDMS, as described in a previous work [30], were used for the synthesis of magnetic hydrogels. The devices used were rectangular channels of height 30 μm with two inlets. The width in the inlet and polymerization region of the channels was 50 μm and 300 μm respectively. The two streams (see Appendix) were flowed in and SFL was used to synthesize H-shaped particles of desired size using appropriate photomasks and stop, polymerization and flow times of 400 ms, 75 ms and 700 ms respectively. The dimensions of the magnetic hydrogels synthesized are given in Table 6.1.

6.5.3 Particle Recovery and Characterization

Each batch consisted of 1000 particles synthesized using SFL and suspended in deionized water with 0.005% (v/v) Tergitol NP-10 (Sigma-Aldrich) and collected in an Eppendorf tube. The particles were washed 5 times using a vacuum manifold with MultiScreen filter plates (Millipore) with pore diameter of 1.2 μm. The cleaned particles were suspended in 300 μl solution in an Eppendorf tube and stored for use in rotation experiments. Magnetic hydrogels having a solids loading of 3 % (same composition as the ones used in this work), synthesized using SFL, have been previously characterized using alternating gradient magnetometry (AGM, MicroMag 2900) [227]. The AGM magnetization curves for both the Seradyn beads and the magnetic hydrogels have been reported in the supporting information of a prior publication by our group [227]. The saturation magnetization and mass susceptibility obtained from the AGM curves are 28 emu/g and 0.981 cm^3/g, respectively for the beads and 3 emu/g and 0.105 cm^3/g for the magnetic hydrogels.

6.5.4 Rotation Experiments

Rotation experiments were performed in PDMS reservoirs with length, width and height of 5 mm each. The reservoirs were made by cutting out square reservoirs of side 5 mm from a 5 mm tall PDMS slab. These structures were placed on a PDMS coated glass slide and then bonded by curing overnight at 60 ^{0}C in an oven. 75 μl of solution with particles was introduced into the reservoir from the Eppendorf tubes in which particles were stored after recovery. The number of particles introduced into the reservoir was tuned in order to obtain a surface coverage, $S \sim 1$ %, where S is defined as the ratio of the sum of the cross-sectional areas of the particles to the area of the reservoir. A S value ~ 1 % is low enough to avoid multi-body interactions. The particles were allowed to sediment for 1 minute after which the reservoir was placed on a micro-plate shaker (VWR) at 650

rpm for 20 seconds to randomize the initial orientation of deposited particles. The reservoir with a random orientation of particles was placed on a microscope and an initial image was taken using a 5× objective and a digital camera (Nikon, D-200). A uniform horizontal magnetic field of 0.005 T was applied using a custom built electromagnet (see Appendix) for varying amounts of time depending on the particles studied and final images were obtained. For particles that rotated, the magnetic field was kept switched on until all particles had rotated to an equilibrium orientation, which varied between 5 seconds to 3 minutes. For 60 μm squares ($W/L = 0.5$, $C/L = 0$), the magnetic field was kept on for 2 hours. For all other cases, the magnetic field was kept on for 30 minutes. We measured the magnetic field in the region of interest using a Gauss/Teslameter Model FW Bell 5060 from Sypris Test and Measurement and found that the magnetic field varied by < 2 % over our imaging area. We also did not observe any large scale movement of particles towards any wall of the reservoir, confirming a uniform magnetic field.

6.5.5 Assembly Experiments

Assembly experiments were performed in a PDMS reservoir similar to the one used for the rotation experiments. 75 μl of solution with particles was introduced into the reservoir from the Eppendorf tubes in which particles were stored after recovery so as to obtain a surface coverage, $S \sim 4.5$ - 5 %. The particles were allowed to sediment for 1 minute before placing the reservoir on a micro-plate shaker (VWR) at 650 rpm for 10 seconds to randomize the initial orientation of deposited particles. The reservoir was then placed on a microscope and a uniform horizontal magnetic field of 0.005 T was applied using a custom built electromagnet (see Appendix) for 30 minutes to obtain the final images for further analysis.

6.5.6 Image Analysis

The orientation (angle) of particles with respect to the direction of the magnetic field, was found using Image J. The orientation of all the particles in the final image for each of the given values of W/L and C/L shown in Table 6.1 was recorded and the deviation of the angles from the equilibrium value predicted using FEI, was evaluated.

6.6 Results and Discussion

6.6.1 Rotation Study

H-shaped particles used in this work (Figure 6.1) can be described by 2 dimensionless groups: W/L and C/L. Furthermore, $C/L = 0$ describes a subgroup of particles which resemble rods of different aspect ratio determined by W/L. Within the rod class is a square which occurs for $W/L = 0.5$. The difference in the energy between the two states (E_0 and E_{90}) scaled by the energy of the square configuration for different values of W/L and C/L is plotted in Figure 6.3. One might expect a square-shaped particle to have a preferred orientation along its longest axis (diagonal). Interestingly, both the FEI technique (Figure 6.2) and MC simulations predicted no preferred orientation, i.e. all orientations have the same energy. When $W/L \to 0$ we have two thin vertical rods of equal length connected by a thin horizontal rod. The two orientations for a thin H would have the same energy when the length of the horizontal connector is twice the length of the vertical rods, i.e. $C/L = 2$. We cannot use FEI to get predictions for the energies in the two

orientations for $W/L = 0$ and $C/L = 2$. However, FEI does predict that in the limit $W/L \to 0$, the two orientations have the same energy for $C/L \to 2$. We plotted $W/L = 0$ and $C/L = 2$ as part of the phase boundary as shown in Figure 6.3.

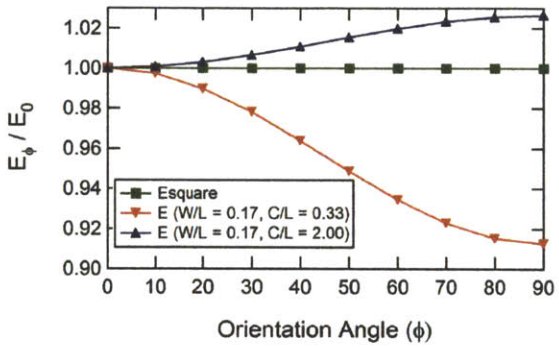

Fig. 6.2: *Energy at different orientations, evaluated using FEI, non-dimensionalized by the energy in the 0^0 orientation for 3 representative shapes. The energy of a square (particle with all sides of equal length) is independent of orientation.*

It can be seen from Figure 6.3 that the vertical orientation is preferred at low values of W/L and C/L and the horizontal orientation is preferred at higher values of W/L and C/L. For values of $W/L < 0.5$ we observe that on increasing C/L at a given value of W/L, the preferred orientation changes from the vertical to the horizontal orientation via a phase boundary (shown by the solid black line in Figure 6.3). We also observe that on increasing C/L at a given value of W/L, the difference in energy increases until a certain value of C/L and then decreases, i.e. the vertical orientation becomes more favored than the horizontal orientation followed by the reverse (Figure 6.3). This phenomenon leads to a re-entrant region at values of $0.5 < W/L < 0.6$, since $W/L = 0.5$ and $C/L = 0$ is a square (has no preferred orientation) and at values of $W/L > 0.5$ and $C/L = 0$, the preferred orientation is horizontal as shown in Figure 6.3. At values of $W/L > 0.6$, the horizontal orientation is the preferred orientation for all values of C/L, since the initial ($C/L = 0$) difference in energy between the two orientations is too large to be compensated by the initial preferrence for the vertical state on increasing C/L (Figure 6.3). MC simulations which predict similar trends as FEI (see Appendix) were not able to resolve the re-entrant region in the phase diagram due to the small energy differences between the two orientations. MC simulations also failed to predict an exact phase boundary. However, the phase boundary predicted by FEI lies in the unresolved region predicted by MC simulations (Appendix).

Experimentally, we investigated a square particle with side 60 μm first, followed by H shapes with different values of W/L and C/L, in the vertical region, horizontal region and near the phase boundary as shown in Figure 6.4. Both the FEI technique and MC simulations predicted no preferred orientation for square-shaped particles which is counterintuitive. Hence, we investigated square-shaped particles thoroughly. We studied $\sim$ 100 square particles over 16 sets of experiments, keeping the magnetic field switched on for 2 hours in each experiment. We took images at multiple time points (0 minutes, 30 minutes, 1 hour and 2 hours) and measured the orientation angle at all

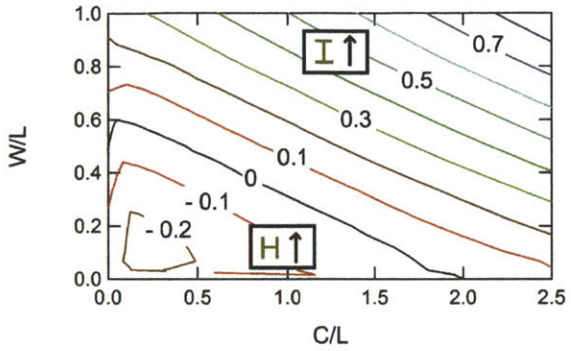

Fig. 6.3: *Contour plot for* $(E_0 - E_{90})$ / E_{square} *as a function of* W/L *and* C/L. *The insets show the preferred orientation of the H-shaped particle on applying a uniform magnetic field. The phase boundary is marked by the solid black line. It can be seen that at values of* $0.5 < W/L < 0.6$, *the preferred orientation changes from* 90^0 *to* 0^0 *and back to* 90^0. *This preference for the* 0^0 *orientation on increasing* C/L *from 0 up to a certain value of* C/L *followed by a preference for the* 90^0 *orientation on increasing* C/L *further is seen at all values of* W/L.

4 times for all particles (see Figure 6.5 for one such experiment). The change in orientation from the initial orientation of the particles was statistically insignificant using a 95% confidence interval, at all times. This suggests that square-shaped particles have the same energy in all configurations validating predictions by the FEI technique and MC simulations.

For H-shaped particles, i.e. for values of W/L and C/L shown in Figure 6.4, we used more than 50 particles to calculate the statistics for re-orientation of particles. The mean and standard deviation of the final configurations (after rotation) of the particles for different values of W/L and C/L at which experiments were conducted are reported in Table 6.1. We observed a distribution of angles as opposed to a single equilibrium orientation for our non-Brownian particles which could be attributed to a number of reasons such as friction between the particles and the reservoir bottom, or experimental limitations in measuring the orientation angles accurately. We also calculated the z statistic for the deviation from the equilibrium value predicted by FEI. In most cases, the deviations were not significant using a 95% confidence interval. The sets of experiments where the deviation was statistically significant have been marked in italics in Table 6.1. We marked the sets of experiments where we could not resolve (less than 75% of the particles were within 1^0 of any mean value, i.e. the histograms did not show a clear peak) an equilibrium orientation, in bold in Table 6.1.

We have shown results from one experiment each at a given value of $W/L = 0.17$ and 4 different values of $C/L = 0$, 0.33, 1.67 and 2.5 in Figure 6.6 as an illustrative example. It can be seen from Figure 6.6 that the preferred orientation changes from vertical to horizontal as C/L increases from 0 to 2.5. Furthermore, at a value of $C/L = 1.67$ (close to the phase boundary), there is no preferred orientation and the magnetic hydrogels do not realign upon switching on the magnetic field. The histograms in Figure 6.6 show a clear peak around an orientation of 0^0 for C/L values of 0 and 0.33 and 90^0 for C/L value of 2.5. However, at a value of $C/L = 1.67$, we see a uniform distribution of

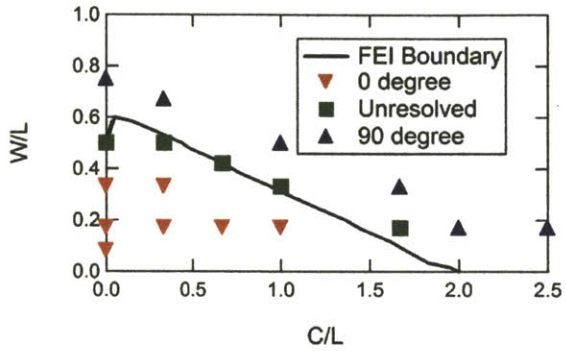

Fig. 6.4: *Comparison between experimental results and predictions by FEI. Experimental results are presented using symbols. The solid black line represents the phase boundary predicted using FEI. It can be seen that experimental results are in good agreement with predictions by FEI.*

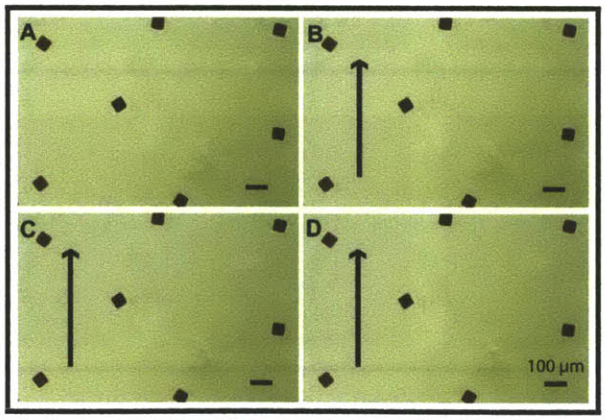

Fig. 6.5: *Images for square-shaped particles A) before, B) 30 minutes, C) 1 hour and D) 2 hours after switching on the magnetic field of 0.005 T. The arrows show the direction of the applied field. On switching on the magnetic field, no rotation was observed for these particles within experimental limitations.*

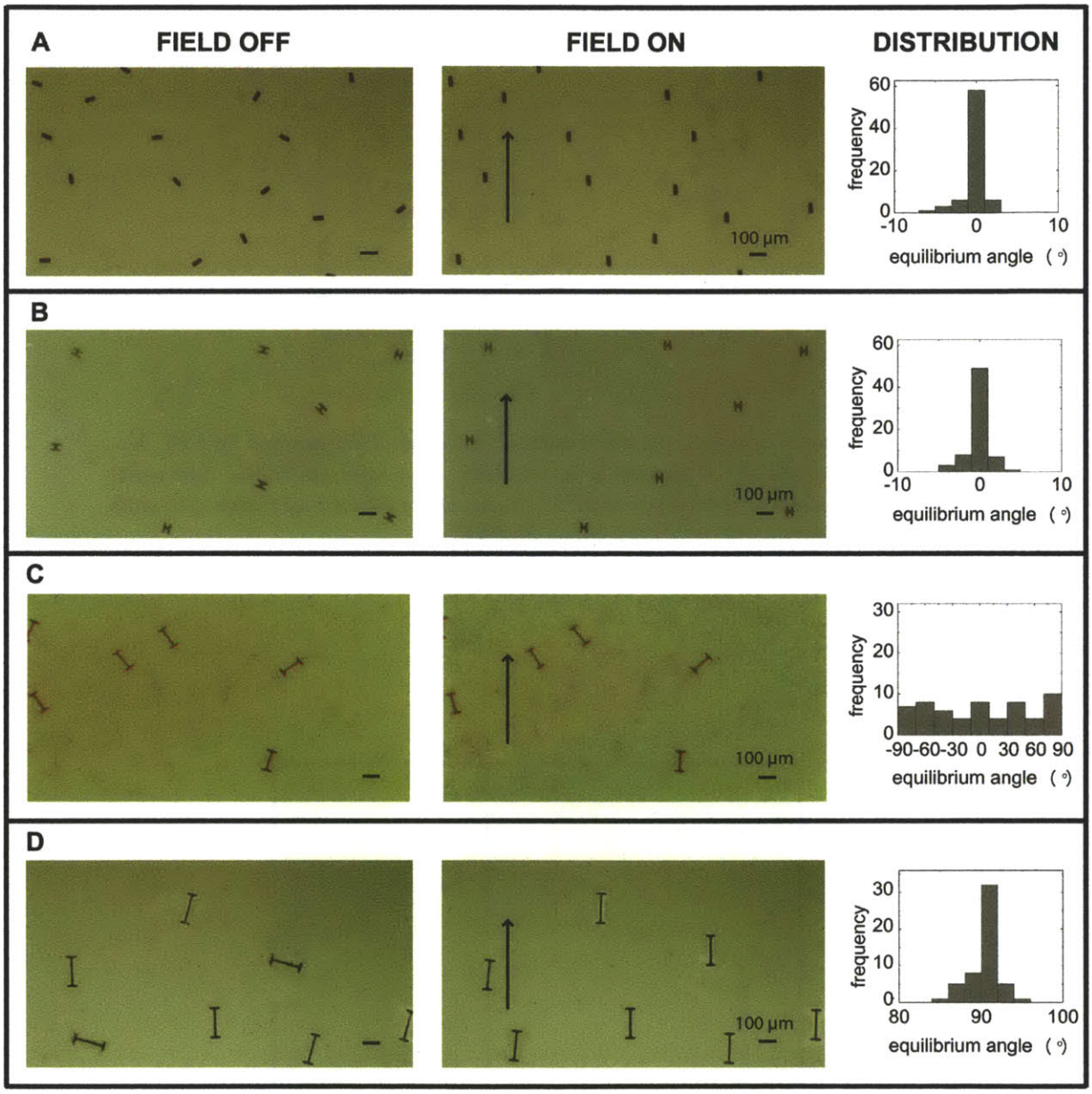

Fig. 6.6: *Initial (before switching on the magnetic field of 0.005 T) and final images of magnetic particles with W/L = 0.17 and C/L values of A) 0, B) 0.33, C) 1.67 and D) 2.5. The arrows in the images in A-D show the direction of the applied magnetic field. The histograms in A, B and D reveal the tight distribution of orientation around 0^0 for C/L = 0 and 0.33 and around 90^0 for C/L = 2.5. For C/L = 1.67, there is a uniform distribution of orientations from -90^0 to 90^0 within experimental limitations as can be seen in the histogram in C.*

Table 6.1: *Summary of all experiments carried out at different values of W/L and C/L for particles with L = 60 μm. The particles have a thickness of 25 μm. The results presented in bold black are unresolved by experimentation whereas the ones presented in italics are resolved but the deviations from the mean equilibrium angle are statistically significant using a 95 % confidence interval. Experimental results are defined as resolved if more than 75 % of the particles lie within 1^0 of the mean predicted by FEI.*

Shape	W (μm)	C (μm)	W/L	C/L	No. of Particles	Equil. Configuration	FEI Prediction
Rod	5	0	0.08	0	80	0.29+/-1.78	0
Rod	10	0	0.17	0	74	-0.28+/-1.30	0
H	10	20	0.17	0.33	68	-0.06+/-1.10	0
H	10	40	0.17	0.67	53	-0.79+/-3.58	0
H	10	60	0.17	1	57	-0.25+/-2.73	0
H	**10**	**100**	**0.17**	**1.67**	**59**	**2.27+/-55.26**	**90**
H	10	120	0.17	2	58	87.14+/-7.56	90
H	10	150	0.17	2.5	52	89.62+/-1.70	90
Rod	20	0	0.33	0	59	-0.46+/-3.28	0
H	20	20	0.33	0.33	59	0.41+/-3.62	0
H	**20**	**60**	**0.33**	**1**	**54**	**2.45+/-47.68**	**Unresolved**
H	20	100	0.33	1.67	51	89.68+/-2.62	90
H	**25**	**40**	**0.42**	**0.67**	**60**	**-11.27+/-53.60**	**Unresolved**
Square	**30**	**0**	**0.5**	**0**	**102**	**-40.09+/-21.81**	**Unresolved**
H	**30**	**20**	**0.5**	**0.33**	**52**	**-9.84+/-42.14**	**Unresolved**
H	30	60	0.5	1	52	89.64+/-2.79	90
H	*40*	*20*	*0.67*	*0.33*	*51*	*91.18+/-2.74*	*90*
Rod	45	0	0.75	0	59	89.55+/-3.28	90

orientations from -90^0 to 90^0, within experimental limitations, suggesting no re-orientation. The above trend on increasing C/L, i.e. preferred vertical orientation, followed by no re-orientation, followed by preferred horizontal orientation was observed for $W/L = 0.33$ as well as can be seen in Figure 6.4.

The experimental results show that there is a region around the phase boundary predicted by FEI wherein the energy difference between the two orientations is too small to be resolved by experiments (Figure 6.4) and a uniform distribution of angles within experimental limitations instead of a clear peak is obtained. Herein lays the strength of the FEI method as it can predict the equilibrium orientation of H-shaped particles in experimentally unresolvable regions of the phase space. Overall, the experimental results are a good match to predictions by FEI, as shown in Figure 6.4. Hence, the phase diagram shown in Figure 6.3 can be used to predict the equilibrium orientation of H-shaped particles of different geometric dimensions.

6.6.2 Assembly Study

Based on the results from the rotation study, we designed experiments to test the ability of H-shaped particles to assemble into wide (orthogonal to the field) chains. We used a mixture of rods and H-shaped particles in the assembly studies. In general, the properties of the final assembly of a mixture of rods and H-shaped particles should depend on: i) the total surface coverage of particles (S), ii) the geometric parameters defining the shape, and iii) the fraction of H-shaped particles in the mixture. In this study, we used moderate surface coverage $S = 4.75$ +/- 0.25 %. At this surface coverage, the assembly of anisotropic magnetic particles involves two distinct motions: rotation followed by translation, as shown in Figure 6.7. Hence, H-shaped particles need to be chosen judiciously so as to orient into desired equilibrium configurations, preceding translation. The H shapes used in the assembly have $C/L = 0.33$ and $W/L = 0.17$ ($T = 25$ μm and $L = 60$ μm). These particles rotate into an equilibrium orientation with the two vertical arms aligned along the magnetic field as shown in Figure 6.7B. This configuration, as opposed to its orthogonal configuration, would have a higher propensity to induce chain widening and branching during particle assembly. Figure 6.7C shows the assembled structures formed after translation. The rod shapes used in this work are similar to a vertical arm of an H shape, with $C/L = 0$ and $W/L = 0.08$ ($T = 25$ μm and $L = 60$ μm). In this study, we focus on the effect of varying the fraction of H-shaped particles on the final assembly.

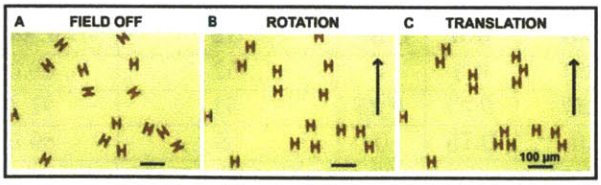

Fig. 6.7: *H-shaped magnetic particles A) before, B) 1 minute after and C) 10 minutes after applying a uniform magnetic field of 0.005 T. The particles first rotate to attain their equilibrium orientation followed by translation to form assembled structures. The arrows show the direction of the applied magnetic field.*

Table 6.2: *Average cluster size, number of branching events and branching events per surface coverage of H-shaped particles for different fractions of H-shaped particles averaged over 3 sets of experiments for each case.*

H frac.	Avg. Cluster Sz. (c_{av})	# Br. Evts. (BE)	Br. Evts. / Surf. Covrg. H shapes (BE / S_H)
0	5.9 +/- 0.3	4.0 +/- 1.0	nd
0.5	4.9 +/- 0.3	6.3 +/- 2.3	2.7 +/- 1.0
1	4.6 +/- 0.3	10 +/- 2.0	2.2 +/- 0.5

We performed 3 replicate experiments at 3 different fractions of H-shaped particles: 0 (deposit of only rod-shaped particles), 0.5 (50 % mixture of rods and H-shaped particles) and 1 (deposit of only H-shaped particles). Representative images are shown in Figure 6.8. We defined a parameter called cluster width (w), as the number of distinct lines parallel to the applied field that can be drawn through a cluster, passing through a rod-shaped particle or at least one vertical arm of an H-shaped particle, as depicted in Figure 6.9. It is worth noting that the minimum w for a collection of H-shaped particles is 2. We present the cluster width distribution normalized by the total number of clusters for the 3 fractions of H-shaped particles in the insets of Figure 6.8. The cluster width distributions show that clusters widen with increasing fraction of H-shaped particles. In order to investigate if this widening of clusters could be attributed to differences in the cluster size, we evaluated the site-weighted average cluster size [228] using:

$$c_{av} = \frac{\sum_{c=1}^{c=\infty} c^2 n(c)}{\sum_{c=1}^{c=\infty} cn(c)} \tag{6.6}$$

where c is the cluster size and $n(c)$ is the number of clusters of cluster size c. A randomly chosen particle would on average belong to a cluster of size c_{av}. It can be seen from Table 6.2 that c_{av} is fairly uniform for the 3 fractions of H-shaped particles used. In fact, c_{av} is highest for a suspension of purely rod-shaped particles. Hence, the wider cluster size distribution observed on increasing the fraction of H-shaped particles is indeed suggestive of the ability of H-shaped particles to induce chain widening in assembly. Furthermore, a fairly uniform c_{av} combined with a wider cluster size distribution suggests shorter, fatter clusters as opposed to thinner, chain-like clusters.

We realized that widening of chains orthogonal to the field occurs due to the ability of H-shaped particles to connect to other particles on either of their vertical arms. This can happen via two different modes: i) branching and ii) meandering, as shown in Figure 6.9. Branched chains are formed when two distinct particles are attached to the vertical arms of an H-shaped particle on the top or on the bottom as shown in Figure 6.9A. Chain widening in the absence of branching gives rise to meandering structures as show in Figure 6.9B. We quantified branching by counting the number of branching events (BE), i.e. the number of distinct H-shaped particles attached to two particles either on the top or on the bottom. For instance, we can observe 2 BE in Figure 6.9A. BE and branching events per surface coverage of H-shaped particles (BE/S_H) for the 3 fractions of H-shaped particles are reported in Table 6.2. We can see that BE increases on increasing the fraction of H-shaped particles in the mixture. However, BE/S_H is fairly constant. These results suggest that part of the chain widening observed on increasing the fraction of H-shaped particles can be attributed to branching.

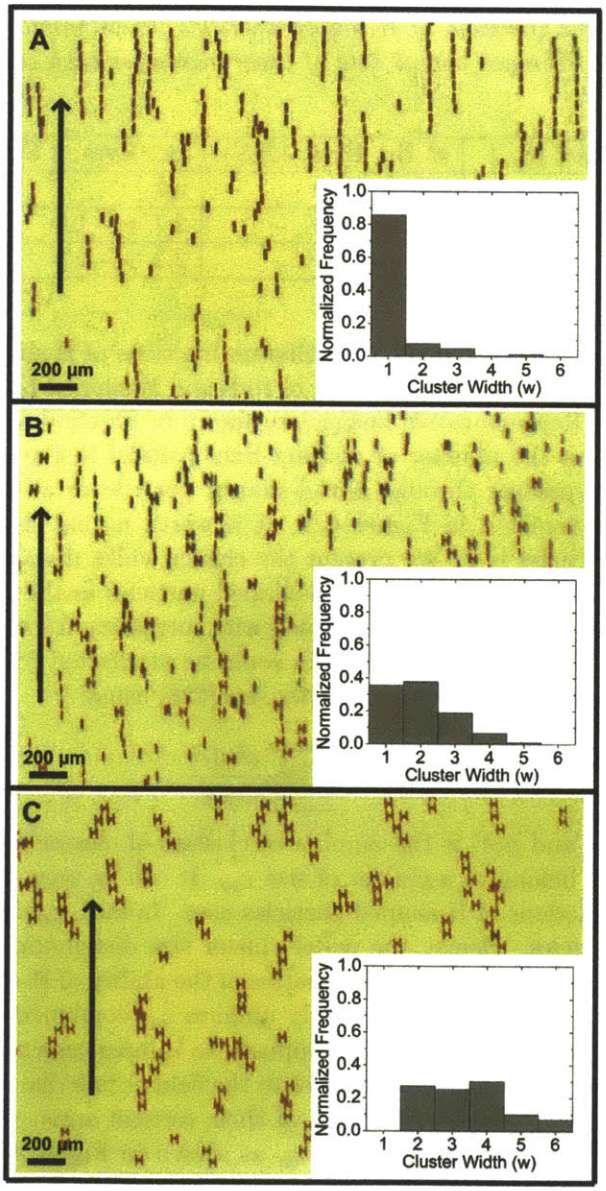

Fig. 6.8: *Final assembly images of A) rods, B) 50 % mixture of rods and H-shaped particles and C) H-shaped particles, in a uniform magnetic field. The arrows show the direction of the applied magnetic field. The inset plots show the corresponding cluster width histograms. Clusters grow wider with increasing fraction of H-shaped particles.*

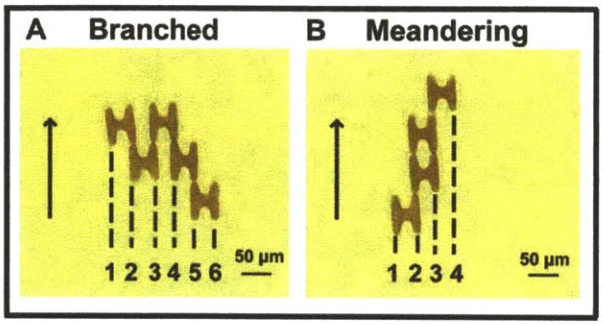

Fig. 6.9: *Two different modes of chain growth orthogonal to the applied magnetic field. A) Branched chain of cluster width 6, formed, in this case by two H-shaped particles connecting on the top side of an H-shaped particle and B) meandering chain of cluster width 4, formed by only one H-shaped particle connecting on one side of an H-shaped particle. The arrows show the direction of the magnetic field.*

6.7 Conclusion

In conclusion we have demonstrated the synthesis of anisotropic H-shaped hydrogels and the dependence of their equilibrium orientation on geometric shape parameters (W/L and C/L). We developed a framework (FEI) for the theoretical prediction of the equilibrium orientation of H-shaped particles and presented the results in the form of a phase diagram. The predicted phase diagram was validated with experiments. Finally, we demonstrated the the ability of H-shaped particles, chosen judiciously from the phase diagram, to induce chain growth orthogonal to the applied field and to form branched structures. FEI can be modified readily to be used for predicting the equilibrium orientation of more complex 2D extruded shapes. Since the assembly of field-responsive particles at low concentrations is a sequential process of rotation followed by translation, the ability to predict the equilibrium orientation of complex 2D extruded particles would help in designing particles for assembly. More broadly, we believe that this work will provide a comprehensive framework to design and investigate microparticles for reverse engineering of target structures through directed assembly [2, 189].

Acknowledgments

The material is based on work supported by the Singapore-MIT Alliance (SMA-2, CPE Program) and NSF grant DMR-1006147. The authors thank Dr. D. Trahan and Dr. M. Helgeson for useful discussions. We also thank Murat Ocalan from the Hatsopoulos Microfluidics Laboratory at MIT for letting us borrow his custom built electromagnet set-up and for useful discussions.

CHAPTER 7

Outlook

The primary goal of this thesis was threefold: i) understanding the flow conditions in stop-flow lithography (SFL), ii) establishing SFL as a versatile microparticle synthesis platform both in the kind of oligomeric fluids that can be used as well as the polymerization conditions, and iii) developing a framework for understanding the field-directed assembly of anisotropic magnetic microparticles.

7.1 Understanding Flow in Stop-Flow Lithography (SFL)

In Chapter 1 we studied the temporal response of an initially deflected PDMS channel. We presented a comprehensive analysis of the temporally complex squeeze flow which occurs in a relaxing PDMS channel. We obtained an analytical zeroth-order solution and compared it to both the numerically obtained full solution and trends observed in experiments. We showed that at small deformations the zeroth-order solution is a good match to the full solution. Further, it explains both qualitative and quantitative trends seen in experiments. This analysis lends insight into many microfluidic processes which exploit channel deformation or, conversely, try to mitigate it.

7.2 SFL for Complex Particle Synthesis

In Chapters 3, 4 and 5 we demonstrated the versatility of SFL as a microparticle synthesis platform. We used oligomeric solutions of different chemistries and properties to synthesize both soft and

hard particles using SFL. Furthermore, we modified the solutions flown through the microchannels to synthesize 3D particles with curvature in the direction orthogonal to the projected UV light demonstrating the ability to generate particles with complex morphologies, using SFL.

7.2.1 SFL for the Synthesis of Cell-Laden Microgel Particles

In Chapter 3, we demonstrated the ability to flow oligomeric solution with cells suspended in it through microchannels and ploymerize cell-laden microgels with good cell viability. Cell suspenions had not been used in SFL prior to this work. We synthesized cell-laden microgels of different 2D shapes which can potentially, be used for assembly into tissue engineered constructs. The high-throughput generation of cell-laden microgels using SFL, can be used for a variety of diagnostic tools in drug delivery and DNA sequencing.

Future Work

The cell-viability obtained in this work can be improved upon, if necessary, for different biomedical applications by using oligomeric solutions and photoinitiators which are less cytotoxic. The concentration of the oligomeric solution and photoinitiators can also be reduced to enhance cell viability. However, a reduction in either of the two would result in a higher polymerization time which could lead to damage of our standard polymeric photomasks. In order to use higher polymerization times without damaging masks, glass or chrome masks can be used. In this work we used NIH - 3T3 mouse fibroblast cells which are a pretty robust cell line. We can investigate the encapsulation of other, more sensitive cell lines using SFL by optimizing oligomeric solutions and photoinitiators. Finally, SFL can be used to synthesize Janus and multi-chemistry particles with a single or multiple cell lines. These particles can then be harvested for multi-cell drug assays or to study the effect of cell environment on nutrient up take. Such parallel assays can reduce the cost and time involved significantly.

7.2.2 SFL for the Synthesis of Ceramic Microcomponents

In Chapter 4, we demonstrated the ability to flow shear thinning silica loaded oligomeric solutions through microchannels and obtain polymeric microcomponents of various shapes. We showed that by index matching our colloidal silica suspensions we could polymerize microcomponents without loss in resolution by minimizing scattering of light. These polymeric microcomponents were converted to porous and dense silica components by sintering for different lengths of time. The porous silica microcomponents were converted to porous silicon microcomponents using magnesiothermic reduction. The colloidal microcomponents synthesized using SFL may be used as novel granular media for fundamental studies of flow, packing, and compaction behavior. SFL allows us to tune the granular shapes over a broader range with relative ease. Furthermore, one can generate granular building blocks with increasing complexity by coflowing multiple suspensions varying in composition or concentration. Finally, the ability to convert these colloidal microcomponents to functional structures by sintering or novel chemical conversion broadens the range of applications they can be used for. As an example, porous silicon microcomponents may find potential applications as gas sensors or in MEMS devices.

Future Work

In this work, we stopped short of harvesting and utilizing the microcomponents synthesized using SFL, for applications. The ability to use the synthesized microgears, in MEMS devices would be an interesting step forward. Another possible future work could involve the tuning of the internal composition of the microcomponents to study their sensitivity to, and subsequent use as capture or purification agents for different gases.

7.2.3 SFL for the Synthesis of 3D Microparticles with Curvature

In Chapter 5, we presented the use of SFL to generate microparticles of modified shape. We tuned the curvature (concavity/convexity) orthogonal to the UV light, to generate a new class of microparticles. We added complexity to these particles by synthesizing Janus, patched and capped polymeric particles. Finally, we classified these particles using 5 anisotropy axis and differentiated them from particles that could be synthesized using standard photolithography and SFL. Curvature can be used to tune the assembly of particles giving rise to macrostructures suitable for applications in biology, for instance, for the generation of scaffolds of desired curvature for directing cell internal organization. Furthermore, particles with curvature can be used to model the wealth of microscale shapes in nature, be it bacteria, platelets, or erythrocytes.

7.3 Framework for the Field-Directed Assembly of Anisotropic Magnetic Hydrogels

In the previous section, we demonstrated the ability to use diverse oligomeric solutions and synthesize particles for various applications, using SFL. In this section, we presented the use of this knowledge to synthesize and study the assembly of non-Brownian rod and H-shaped hydrogels with encapsulated magnetic beads.

7.3.1 Rotation and Assembly of Anisotropic Magnetic Particles

In Chapter 6, we developed a framework to study the equilibrium orientation of magnetic hydrogels synthesized using SFL. The assembly of anisotropic particles at low surface coverages involves two time steps: i) rotation and ii) translation. Hence, the assembled structures formed by anisotrpic magnetic particles on applying a uniform magnetic field would depend on the initial orientation attained by them. In this chapter, we presented a Finite Element Integration (FEI) method to identify the preferred orientation (relative to the applied field) at different values of the geometric parameters defining an H shape. We chose H shapes since, they should have a high propensity to form branched structures which is interesting from both a fundamental as well as a technological standpoint. Furthermore, we presented assembly results for a mixture of rod and H-shaped particles at a low total particle surface coverage. We used the phase diagram to design H-shaped particles which would have a high propensity to assemble into branched structures. We then demonstrated chain widening and branching orthogonal to the applied field induced by the chosen H shapes, in their assembly, due to their intrinsic shape. This work can potentially be used to design magnetorheological (MR) fluids with improved properties and in generating macrostructures with complex morphologies for material synthesis.

7.3.2 Future Work

The framework presented in this section can be used to study the assembly of quasi-2D, non-Brownian magnetic particles of any shape. Some potential branched shapes that can be studied are X-shaped, Y-shaped and star-shaped particles. The FEI technique can be easily adapted to study the dependence of the equilibrium orientation of any quasi-2D shape on its intrinsic geometric parameters. The results of the predictions by FEI can be used to judiciously design particles for further assembly into desired macrostructures. Furthermore, the assembly of particles of different shapes can be studied and compared at different concentrations. This would allow us to identify parameters like percolation threshold and hence the networking efficiency of different particles.

7.4 Overall Impact

Overall, this thesis presents a complete story beginning with the understanding of a key process, for a particle synthesis technique (SFL), followed by demonstrating the strengths/versatility of the technique by synthesizing particles with different chemistries and morphologies using the technique and finally the use of the particles synthesized with the technique for a non-trivial application (field-directed assembly of anisotropic particles). This research will contribute to further exploring the potential of SFL for complex particle synthesis, and their use in various applications primarily self-assembly.

Appendix A

H-shaped Magnetic Particles

A.1 Comparison of energy between a 2D extruded and a quasi-2D shape

The magnetic field is applied in a direction orthogonal to the thickness of the 2D extruded particle. Let us assume that the extrusion (thickness) is in the z direction and hence the magnetic field is on the x-y plane. We simplify the problem further by assuming the magnetic field is along the x axis. We choose a bead on the bottom most plane, i.e. z = 0 and denote it by P_1. We choose another bead on plane z = 0 and denote it by P_2. We choose a third bead on some plane z = n directly above P_2 and denote it by P_n. The interaction energy between P_1 and P_n is given by

$$U_{1n}(r_{1n},\theta_{1n})\frac{4\pi}{m^2\mu_o} = \frac{1-3cos^2\theta_{1n}}{r_{1n}^3} = \frac{1-3(\frac{L_r}{L_0})^2cos^2\theta}{L_0^3} \tag{A.1}$$

where L_r and L_0 are the length of the vectors joining P_1 and P_2 and P_1 and P_n respectively. θ is the angle between the magnetic field and the vector joining P_1 to P_2. The total energy of the 2D extruded particle due to the interaction of P_1 with all beads at different values of z stacked above P_2 can be obtained by integrating the expression in Equation A.1 given by

$$U_1(\theta)\frac{4\pi}{m^2\mu_o} = \int_0^H \frac{1-3(\frac{L_r^2}{L_r^2+z^2})cos^2\theta}{(L_r^2+z^2)^{\frac{3}{2}}}dz \tag{A.2}$$

where H is the height of the extruded particle. We can evaluate the energy given in Equation A.2 numerically using a discrete sum given by the expression

$$U_1(\theta)\frac{4\pi}{m^2\mu_o} = \sum_{z=0}^{N} \frac{1-3(\frac{L_r^2}{L_r^2+L_z^2})cos^2\theta}{(L_r^2+L_z^2)^{\frac{3}{2}}} \tag{A.3}$$

where L_z is the distance between planes z=0 and z=n and N is the total number of layers. We plotted U_1 with θ for two different values of L_r for three different cases of $L_r << L_N$, $L_r = L_N$ and $L_r >> L_N$ and found that in all cases the shape of the curve is the same as would be if only the interaction between P_1 with single particles at distance L_r in the x-y plane was considered. This suggests that the presence of beads along the z direction, i.e. thickness of the particle would not affect the analysis for the orientation with minimum energy performed using a single layer of beads along the x-y axis. Hence, it is sufficient to consider quasi-2D particles to predict the orientation with minimum energy for our 2D extruded particles.

A.2 Analysis of a quasi-1D rod

A quasi-1D rod with a homogeneous distribution of beads in it, having a thickness and width of T and W respectively where T and W are small compared to the legnth L of the rod, can be modeled as a series of rectangular cuboid meshes of constant magnetization (M), with a width and thickness given by W and T respectively and the length given by mesh size s. The nondimensionalized energy for a quasi-1D rod can obtained using Equations 6.2 and 6.4 (Chapter 6) and is given by

$$E_\phi = \frac{U_\phi}{\frac{M^2W^2T^2\mu_o}{8\pi L}} = \kappa^2(1-3cos^2\phi)\sum_{i\neq j}^{\zeta}\frac{1}{(\frac{r_{ij}}{L})^3}. \tag{A.4}$$

where M is the volumetric magnetization of the magnetic hydrogel, $\kappa = s/L$ is the nondimensionalized mesh size and $\zeta = L/s$ is the number of mesh elements. FEI involves using the above equation, i.e. summing the interaction energy between all the mesh elements. The energy given in Equation A.4 diverges as $O(1/\kappa^2)$ in the limit of $\kappa \to 0$ since the number of terms in the summation grows like $1/\kappa$ (nearest neighbors) and $1/r^3 \sim 1/\kappa^3$.

A.3 Microfluidic Devices and Photopolymerization Setup

Rectangular channels of height 30 μm with two inlets of width 50 μm and polymerization region of width 300 μm were fabricated by pouring polydimethylsiloxane (PDMS, Sylgard 184, Dow Corning) on a silicon wafer containing positive-relief channels patterned in SU-8 photoresist (Microchem). The PDMS devices were sealed to a glass slide spin-coated with PDMS to ensure that all four walls of the channel were PDMS. The devices were mounted on an inverted microscope (Axiovert 200, Zeiss), and the hydrogels were visualized using a CMOS camera (DMK 41BUC02, The Imagingsource).

A.4 Stop Flow Lithography

Two streams (magnetic fluid and co-stream) (Figure A.1) were introduced into the microfluidic device using a pressure pulse. The co-stream was comprised of 35 % poly(ethylene glycol) (700)

diacrylate (PEG-DA, Sigma Aldrich), 5 % Darocur 1173, 25 % poly(ethylene glycol) (200) (PEG, Sigma Aldrich) and 35 % TET (1x Tris-EDTA with 0.05 % Tween-20 (Sigma-Aldrich)). The flow was stopped and particles were synthesized in the co-stream to determine the focal plane for generating particles with good resolution. Once the focal plane was determined, the co-stream was thinned by decreasing the pressure difference across that stream in the flow direction. Magnetic hydrogels were then synthesized in the magnetic fluid stream by flashing UV light through the photomask using stop, polymerization and flow times of 400 ms, 75 ms and 700 ms respectively and collected in the reservoir cut out at the end of the microfluidic device. The magnetic hydrogels were synthesized in a 30 μm tall channel resulting in a particle thickness of 25 μm.

A.5 Particle Analysis

We investigated the homogeneity of the distribution of Seradyn beads in our magnetic microparticles by evaluating the intensity profile of a single particle using Image J as shown in Figure A.2. The statistical properties of the intensity distribution are reported in Table A.1. The intensity profile is fairly uniform as can be seen from Figure A.2 and Table A.1 suggesting a homogeneous distribution of beads in the microparticle at the relevant length scales in the problem.

A.6 Mesh Size Dependence of the Phase Boundary

We plotted the phase boundary predicted by FEl at different mesh sizes spanning an order of magnitude (κ = 0.0017 - 0.0167). The variation in the predicted phase boundary at different mesh sizes is insignificant as shown in Figure A.3. We did not use $\kappa > 0.0167$ since we wanted to investigate the phase boundary at small values of C/L and W/L in order to observe the re-entrant behavior which would necessitate $\kappa < C/L$ and $\kappa < W/L$.

A.7 Monte-Carlo Simulations

We performed off-lattice MC simulations using MATLAB to determine the energy in two orientations (0^0 and 90^0) for the thin 2D extruded H-shaped hydrogels (Figure 6.1A, Chapter 6) at different values of W/L and C/L. The non-dimensional lengths in the problem are

$$\alpha = L/d, \quad \beta = W/d, \quad \gamma = C/d, \tag{A.5}$$

where d is the bead diameter. The cut-off distance to ensure no overlap between beads is taken to be the bead diameter. Typical values for the non-dimensional lengths in our problem are: $\alpha = 75$, $0 < \beta < 187.5$ and $0 < \gamma < 75$. We selected a square box of non-dimensional side 187.5 centered at the origin as our simulation region. H shapes with boundaries defined by different values of α, β and γ were placed within the box. In order to evaluate the energy in the 0^0 configuration, we selected two random points within the square box using the random number generator in MATLAB and if the two points were within the H shape and did not overlap, we evaluated the nondimensionalized energy (E_{ij}) using

$$E_{ij}(r_{ij}, \theta_{ij}) = U_{ij}(r_{ij}, \theta_{ij}) \frac{4\pi d^3}{m^2 \mu_o} = \frac{1 - 3cos^2\theta_{ij}}{(r_{ij}/d)^3} \tag{A.6}$$

Table A.1: *Statistical properties of the intensity distribution in arbitrary units (A.U.) in a square-shaped magnetic microparticle. The standard deviation is < 25 % of the mean.*

Mean	St. Dev.	Min.	Max.	Median	Skew	Kurtosis
55.49	13.92	43	122	51	2.72	7.57

where m is the magnitude of the dipole moment of a single bead. If any of the two aforementioned criteria were not satisfied, the energy = 0. We repeated the above steps 1.2 billion times and took the average of all the energy calculations in each step to obtain a mean nondimensionalized energy (E) value. The standard errors on the mean were evaluated using 100 sample means to obtain error bars on the mean (Figure A.4A). For evaluating the energy in the 90^0 orientation, we rotated the random points by 90^0. We evaluated the energy using Equation A.6 if the rotated points lay within the boundary of the H shape and if the two points did not overlap. The boundary of the H shape was not rotated, i.e. remained the same as for the 0^0 orientation. The rest of the procedure remained the same as for the evaluation of the energy in the 0^0 orientation. The dependence of the difference in the non-dimensionalized energies (ΔE) on C/L for $W/L = 0.17$ is reported in Figure A.4B. The error bars in Figure A.4B were evaluated from the standard errors by taking the maximum and minimum possible difference between the evaluated means in the two configurations using a 90 % confidence interval. The values of C/L for which the error bars in Figure A.4B overlap with $\Delta E = 0$ are shapes for which MC simulations failed to resolve the energy difference and hence the preferred orientation. The results of the MC simulations for different values of W/L and C/L are shown in Figure A.5.

A.8 Comparison Between FEI and MC Simulations

It can be seen from Figure A.5 that the phase boundary predicted by FEI lies in the unresolved region predicted by the MC simulations. Furthermore, it can be seen from Figure A.4B that on increasing C/L at a given value of W/L there is initially a preferrence for the vertical orientation followed by a preferrence for the horizontal orientation. This phenomenon is also observed when we evaluate the energies uisng the FEI technique (Figure 6.3, Chapter 6). We also compared the values of the energy in the vertical and horizontal configuration predicted by MC and FEI simulations for two values of W/L and three values of C/L and found the ratio to be ~ 0.68, i.e. the energy values obtained using the two techniques were of the same order of magnitude.

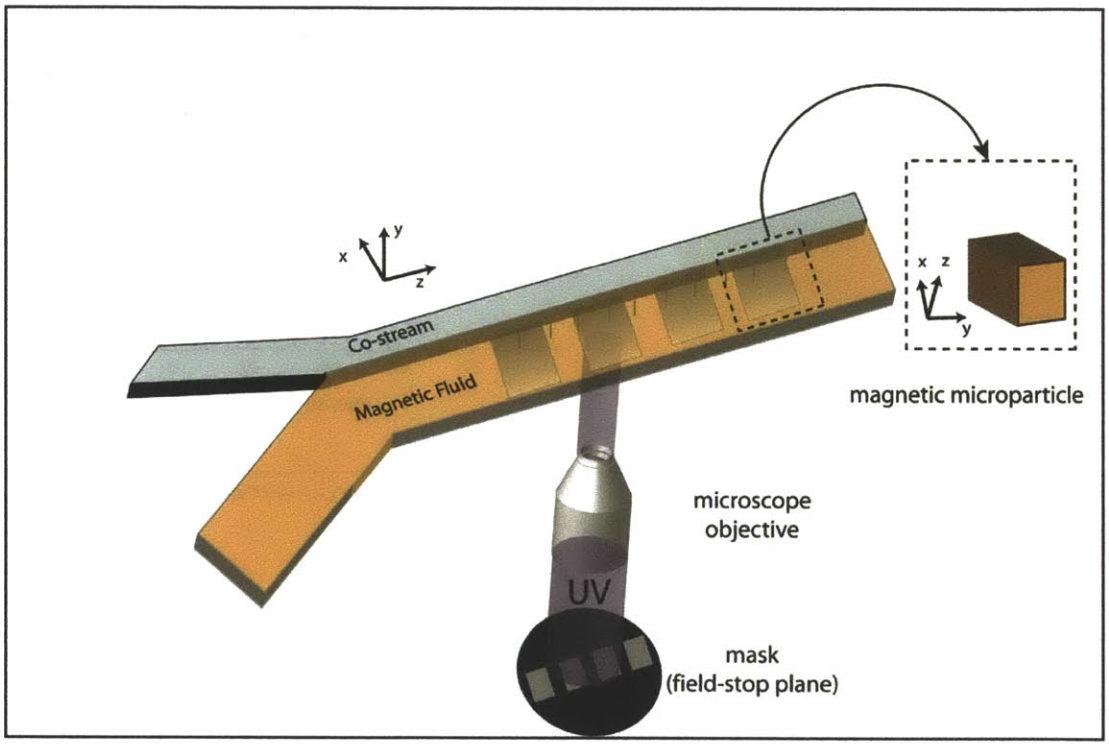

Fig. A.1: *Schematic for the synthesis of magnetic particles. Two streams one with the magnetic beads suspended in it called the magnetic fluid and the other a mixture of PEG-DA and Darocur-1173 called the co-stream was flown simultaneously through the channel. The focal plane for the synthesis of particles with good resolution was determined by polymerizing in the co-stream and observing the particles formed. Once the focal plane was determined, the co-stream was thinned by decreasing the pressure difference across the stream in the flow direction and particles were polymerized by flashing UV light in the magnetic fluid.*

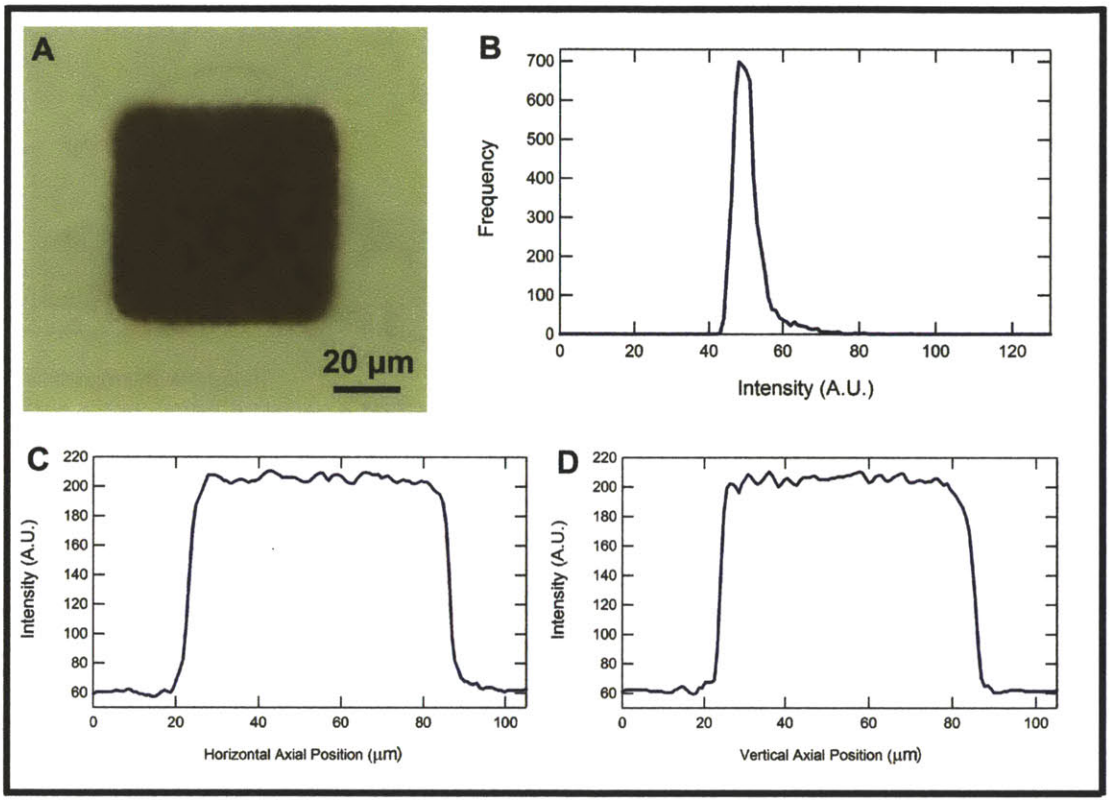

Fig. A.2: *(A) Image of a square-shaped magnetic hydrogel with magnetic beads encapsulated in it. B) Intensity distribution in arbitrary units (A.U.) through our particle. Intensity in arbitrary units along C) the horizontal axis and D) the vertical axis through the center of the particle plotted against the axial position. The intensity profile is fairly uniform suggesting a homogeneous distribution of beads in the microparticle at the relevant length scales in the problem.*

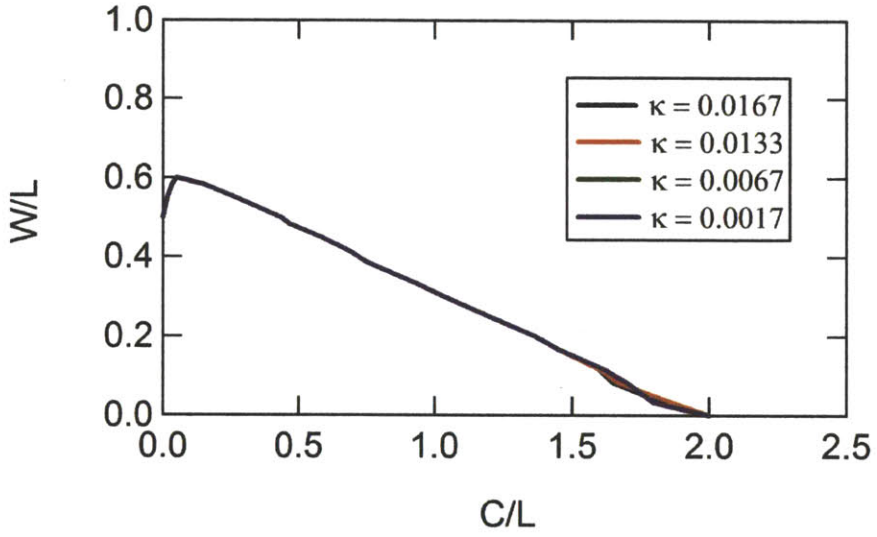

Fig. A.3: *The phase boundary predicted by FEI at different values of* κ *ranging from 0.0167 to 0.0017. The variation in the predicted phase boundaries at different values of* κ *is insignificant.*

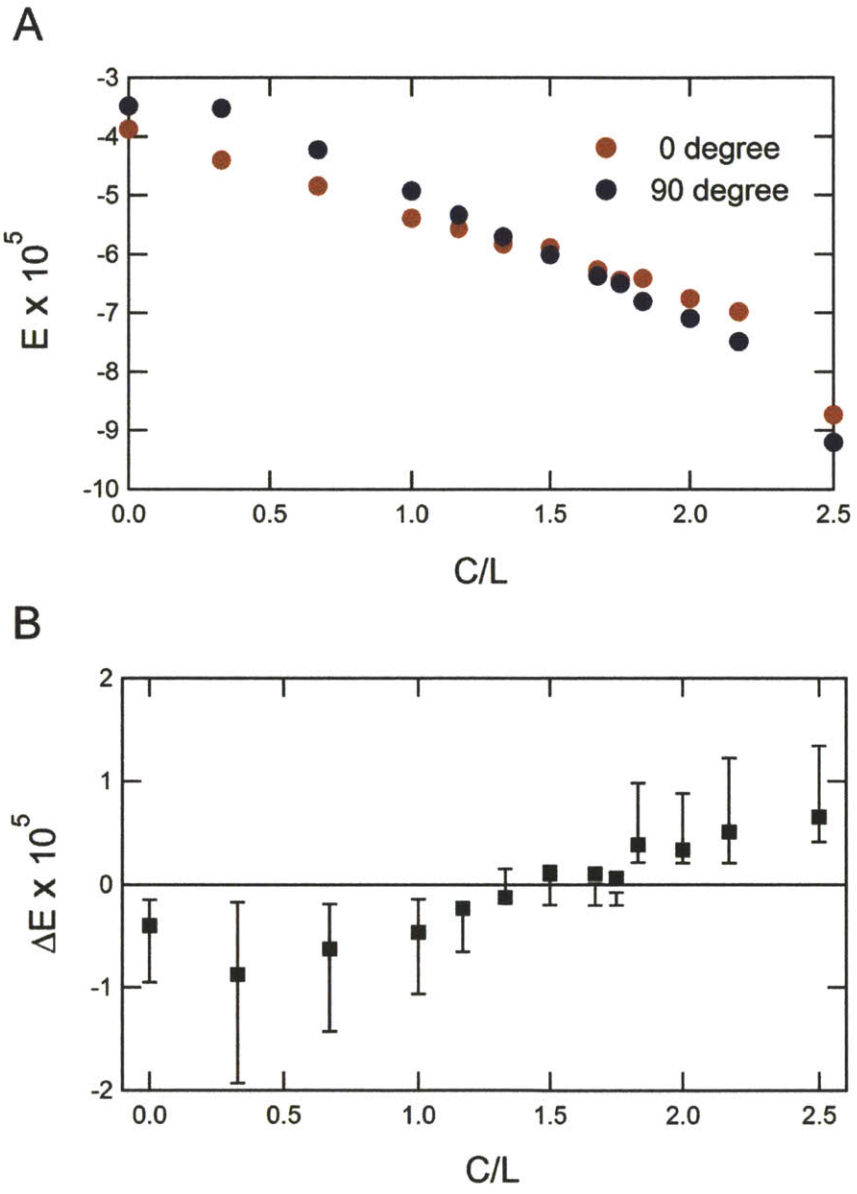

Fig. A.4: *A) Nondimensional energies for two different configurations of* 0^0 *and* 90^0 *and B) Difference in energy between the two configurations at different values of* C/L *for* $W/L = 0.17$. *The error bars in A), generated using the standard errors for a 90 % confidence interval around the mean energy are as big as the size of the circles. The error bars in B) are the maximum and minimum possible deviations in the energy difference using the same 90 % confidence interval. The values of* C/L *for which the error bars in B) overlap with* $\Delta E = 0$ *are shapes wherein the energy difference between the two configurations is too small to be able to be resolved with 90 % confidence.*

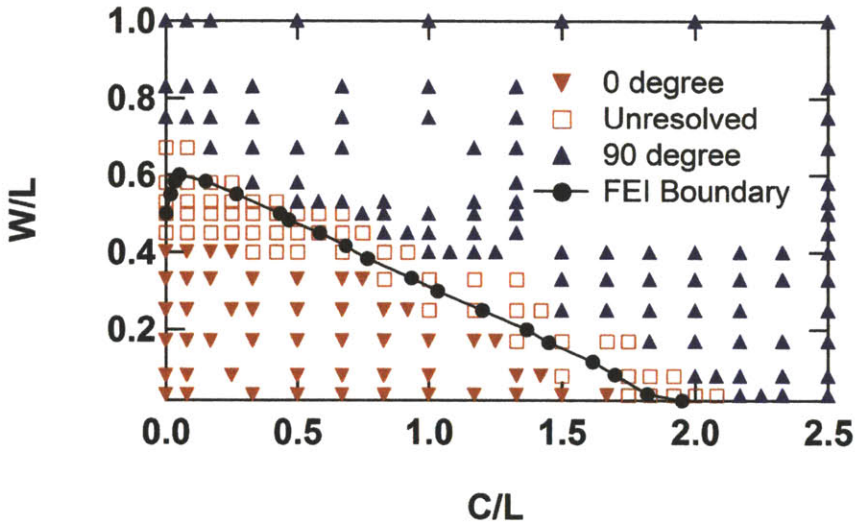

Fig. A.5: *Comparison between the predictions by the FEI and MC simulation techniques. The lower energy orientation predicted by the MC simulations is denoted by the inverted and straight triangles for the* 0^0 *and the* 90^0 *orientations respectively. The square boxes denote values of the geometric parameters* $(W/L$ *and* $C/L)$ *for which the lower energy configuration could not be resolved by the MC simulation. The phase boundary predicted by FEI is marked by the solid black line. It can be seen that the phase boundary predicted by the FEI numerical technique lies in the unresolved region predicted by the MC simulation.*

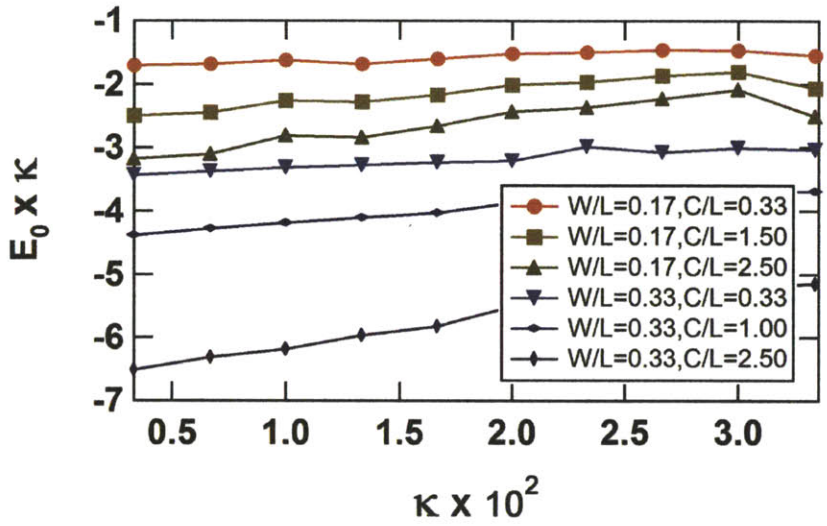

Fig. A.6: *Energy values in the* 0^0 *orientation* (E_0) *obtained using FEI, multiplied with* κ *plotted against the nondimensionalized mesh size* (κ) *for two different values of* W/L *and three different values of* C/L. *The product converges for these six representative shapes i.e. the change in the product on varying* κ *from 0.007 to 0.003 is less than 10 %.*

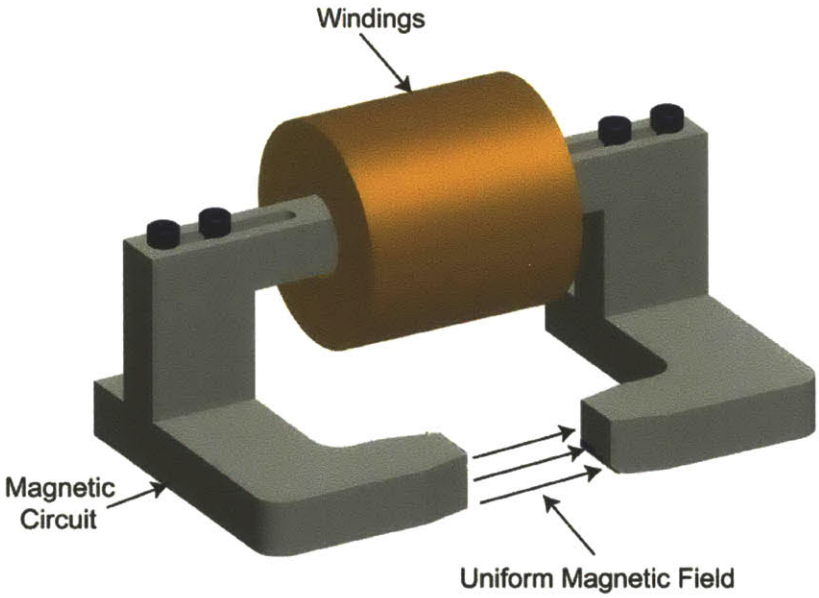

Fig. A.7: *The custom built electromagnetic set-up used in our experiments. The windings are connected to an external power source. The current flowing through the windings can be varied to control the strength of the uniform magnetic field generated The image has been adapted from the paper presented by Murat et al., at the 12th International Conference on Electrorheological Fluids and Magnetorheological Suspensions, Philadelphia, 2010.*

Bibliography

[1] Pickering, S. U. *J. Chem. Soc.* **1907**, *91*, 2001.

[2] Glotzer, S. C.; Solomon, M. J. *Nat. Mater.* **2007**, *6*, 557.

[3] Leunissen, M. E.; Christova, C. G.; Hynninen, A. P.; Royall, C. P.; Campbell, A. I.; Imhof, A.; Dijkstra, M.; van Roij, R.; van Blaaderen, A. *Nature* **2005**, *437*, 235.

[4] Bartlett, P. A.; Campbell, A. I. *Phys. Rev. Lett.* **2005**, *95*, 128302.

[5] Maskaly, G. R.; Garcia, E. R.; Carter, W. C.; Chiang, Y. M. *Phys. Rev. E* **2006**, *73*, 014402.

[6] Shevchenko, E. V.; Talapin, D. V.; Kotov, N. A.; O'Brien, S.; Murray, C. B. *Nature* **2006**, *439*, 55.

[7] Hynninen, A. P.; Christova, C. G.; van Roij, R.; van Blaaderen, A.; Dijkstra, M. *Phys. Rev. Lett.* **2006**, *96*, 138308.

[8] Zhang, Z. L.; Glotzer, S. C. *Nano Lett.* **2004**, *4*, 1407.

[9] Iacovella, C. R.; Horsch, M. A.; Zhang, Z.; Glotzer, S. C. *Langmuir* **2005**, *21*, 9488.

[10] van Workum, K.; Douglas, J. F. *Phys. Rev. E* **2006**, *73*, 031502.

[11] John, B. S.; Stroock, A.; Escobedo, F. A. *J. Chem. Phys.* **2004**, *120*, 9383.

[12] Sun, Y. G.; Xia, Y. N. *Science* **2002**, *298*, 2176.

[13] Gou, L. F.; Murphy, C. J. *Nano Lett.* **2003**, *3*, 231.

[14] Ahmadi, T. S.; Wang, Z. L.; Green, T. C.; Henglein, A.; El-Sayed, M. A. *Science* **1996**, *272*, 1924.

[15] Malikova, N.; Pastoriza-Santos, I.; Schierhorn, M.; Kotov, N. A.; Liz-Marzan, L. M. *Langmuir* **2002**, *18*, 3694.

[16] Greyson, E. C.; Barton, J. E.; Odom, T. W. *Small* **2006**, *2*, 368.

[17] Jin, R. C.; Cao, Y. W.; Mirkin, C. A.; Kelly, K. L.; Schatz, G. C.; Zheng, J. G. *Science* **2001**, *294*, 1901.

[18] Shankar, S. S.; Rai, A.; Ankamwar, B.; Singh, A.; Ahmad, A.; Sastry, M. *Nat. Mater.* **2004**, *3*, 482.

[19] Cayre, O. J.; Paunov, V. N.; Velev, O. D. *J. Mater. Chem.* **2003**, *13*, 2445.

[20] Hong, L.; Cacciuto, A.; Luijten, E.; Granick, S. *Nano Lett.* **2006**, *6*, 2510.

[21] Love, J. C.; Gates, B. D.; Wolfe, D. B.; Paul, K. E.; Whitesides, G. M. *Nano Lett.* **2002**, *2*, 891.

[22] Jackson, A. M.; Stellacci, F. *Nat. Mater.* **2004**, *3*, 330.

[23] Manna, L.; Scher, E. C.; Alivisatos, A. P. *J. Am. Chem. Soc.* **2000**, *122*, 12700.

[24] Chen, S. H.; Wang, Z. L.; Ballato, J.; Foulger, S. H.; Carroll, D. L. *J. Am. Chem. Soc.* **2003**, *125*, 16186.

[25] Lee, S. M.; Jun, Y.; Cho, S. N.; Cheon, J. *J. Am. Chem. Soc.* **2002**, *124*, 11244.

[26] Zhang, G.; Wang, D. Y.; Mohwald, H. *Angew. Chem. Int. Ed.* **2005**, *44*, 7767.

[27] Zhang, Z. L.; Keys, A. S.; Chen, T.; Glotzer, S. C. *Langmuir* **2005**, *21*, 11547.

[28] Jana, N. R.; Gearheart, L.; Murphy, C. J. *J. Phys. Chem. B* **2001**, *105*, 4065.

[29] Roh, K. H.; Martin, D. C.; Lahann, J. *Nat. Mater.* **2005**, *4*, 759.

[30] Dendukuri, D.; Pregibon, D. C.; Collins, J.; Hatton, T. A.; Doyle, P. S. *Nat. Mater.* **2006**, *5*, 365.

[31] Manoharan, V. N.; Elsesser, M. T.; Pine, D. J. *Science* **2003**, *301*, 483.

[32] Yin, Y. D.; Lu, Y.; Gates, B.; Xia, Y. N. *J. Am. Chem. Soc.* **2001**, *123*, 8718.

[33] Rolland, J. P.; Maynor, B. W.; Euliss, L. E.; Exner, A. E.; Denison, G. M.; DeSimone, J. M. *J. Am. Chem. Soc.* **2005**, *127*, 10096.

[34] Hernandez, C. J.; Mason, T. G. *J. Phys. Chem. C* **2007**, *111*, 4477.

[35] Bansal, V.; Sanyal, A.; Rautaray, D.; Ahmad, A.; Sastry, M. *Adv. Mater.* **2005**, *17*, 889.

[36] Brown, S.; Sarikaya, M.; Johnson, E. *J. Mol. Biol.* **2000**, *299*, 725.

[37] Sugiura, S.; Nakajima, M.; Itou, H.; Seki, M. *Macromol. Rapid Com.* **2001**, *22*, 773.

[38] Nisisako, T.; Torii, T.; Higuchi, T. *Chem. Eng. J.* **2004**, *101*, 23.

[39] Dendukuri, D.; Tsoi, K.; Hatton, T. A.; Doyle, P. S. *Langmuir* **2005**, *21*, 2113.

[40] Xu, S.; Nie, Z.; Seo, M.; Lewis, P.; Kumacheva, E.; Stone, H. A.; Garstecki, P.; Weibel, D. B.; Gitlin, I.; Whitesides, G. M. *Angew. Chem. Int. Ed.* **2005**, *44*, 724.

[41] Jeong, W. J.; Kim, J. Y.; Choo, J.; Lee, E. K.; Han, C. S.; Beebe, D. J.; Seong, G. H.; Sang, H. L. *Langmuir* **2005**, *21*, 3738.

[42] Nisisako, T.; Torii, T.; Takahashi, T.; Takizawa, Y. *Adv. Mater.* **2006**, *18*, 1152.

[43] Utada, A. S.; Lorenceaui, E.; Linki, D. R.; Weitz, D. A. *Science* **2005**, *308*, 537.

[44] Lorenceau, E.; Utada, A.; Linki, D. R.; Weitz, D. A. *Langmuir* **2005**, *21*, 9183.

[45] Takeuchi, S.; Garstecki, P.; Weibel, D. B.; Whitesides, G. M. *Adv. Mater.* **2005**, *17*, 1067.

[46] Nisisako, T.; Pkushima, S.; Torii, T. *Soft Mater* **2005**, *1*, 13.

[47] Steinbacher, J. L.; Moy, R. W. Y.; Price, K. E.; Buffy, J. J.; McQuade, D. T. *J. Am. Chem. Soc.* **2006**, *128*, 9442.

[48] Dendukuri, D.; Gu, S. S.; Pregibon, D. C.; Hatton, T. A.; Doyle, P. S. *Lab Chip* **2007**, *7*, 818.

[49] Lotters, J. C.; Olthuis, W.; Veltink, P. H.; Bergveld, P. *J. Micromech. and Microeng.* **1997**, *7*, 145.

[50] Gervais, T.; El-Ali, J.; Gunther, A.; Jensen, K. F. *Lab Chip* **2006**, *6*, 500.

[51] Unger, M. A.; Chou, H. P.; Thorsen, T.; Scherer, A.; Quake, S. R. *Science* **2000**, *288*, 113.

[52] Chronis, N.; Liu, G. L.; Jeong, K. H.; Lee, L. P. *Optics Express* **2003**, *11*, 2370.

[53] Popel, A. S.; Johnson, J. C. *Annu. Rev. Fluid Mech.* **2005**, *37*, 43.

[54] Grotberg, J. B.; Jensen, O. E. *Annu. Rev. Fluid Mech.* **2004**, *36*, 121.

[55] Womersley, J. R. *Phys. Med. Biol.* **1957**, *2*, 178.

[56] Delamarche, E.; Schmid, H.; Michel, B.; Biebuyck, H. *Adv. Mater.* **1997**, *9*, 741.

[57] Manz, A.; Graber, N.; Widmer, H. M. *Sensors Actuators B-Chemical* **1990**, *1*, 244.

[58] Lu, H.; Koo, L. Y.; Wang, W. M.; Lauffenburger, D. A.; Griffith, L. G.; Jensen, K. F. *Anal. Chem.* **2004**, *76*, 5257.

[59] Murthy, S. K.; Sin, A.; Tompkins, R. G.; Toner, M. *Langmuir* **2004**, *20*, 11649.

[60] Wofsy, C.; Goldstein, B. *Biophys. J.* **2002**, *82*, 1743.

[61] Furuki, M.; Kameoka, J.; Craighead, H. G.; Isaacson, M. S. *Sensors and Actuators B-Chemical* **2001**, *79*, 63.

[62] Dendukuri, D.; Doyle, P. S. *Adv. Mater.* **2009**, *21*, 1.

[63] Deen, W. M. **1998**, 114.

[64] Stone, H. A.; Stroock, A. D.; Ajdari, A. *Annu. Rev. Fluid Mech.* **2004**, *36*, 381.

[65] Fütterer, C.; Minc, N.; Bormuth, V.; Codarbox, J. H.; Laval, P.; Rossier, J.; Viovy, J. L. *Lab Chip* **2004**, *4*, 351.

[66] Langer, R.; Vacanti, J. P. *Science* **1993**, *260*, 920.

[67] Liu, V. A.; Bhatia, S. N. *Biomed. Microdevices* **2002**, *4*, 257.

[68] Khademhosseini, A.; Langer, R. *Biomaterials* **2007**, *28*, 5087.

[69] Peppas, N. A.; Hilt, J. Z.; Khademhosseini, A.; Langer, R. *Adv. Matter.* **2006**, *18*, 1345.

[70] Khademhosseini, A.; Langer, R.; Borenstein, J. P.; Vacanti, J. P. *Proc. Natl. Acad. Sci, U.S.A* **2006**, *103*, 2480.

[71] McGuigan, A. P.; Sefton, M. V. *Proc. Natl. Acad. Sci, U.S.A* **2006**, *103*, 11461.

[72] Burnham, M. R.; Turner, J. N.; Szarowski, D.; Martin, D. L. *Biomaterials* **2006**, *27*, 5883.

[73] Koh, W. G.; Revzin, A.; Simonian, A.; Reeves, T.; Pishko, M. *Biomed. Microdevices* **2003**, *5*, 11.

[74] Albrecht, D. R.; Underhill, G. H.; Wassermann, T. B.; Sah, R. L.; Bhatia, S. N. *Nat. Methods* **2006**, *3*, 369.

[75] Underhill, G. H.; Chen, A. A.; Albrecht, D. R.; Bhatia, S. N. *Biomaterials* **2007**, *28*, 256.

[76] Tsangl, V. L.; Chen, A. A.; Cho, L. M.; Jadin, K. D.; Sah, R. L.; DeLong, S.; West, J. L.; Bhatia, S. N. *FASEB J.* **2007**, *21*, 790.

[77] Vozzi, G.; Flaim, C.; Ahluwalia, A.; Bhatia, S. N. *Biomaterials* **2003**, *24*, 2533.

[78] Cheung, Y. K.; Gillette, B. M.; Zhong, M.; Ramcharan, S.; Sia, S. K. *Lab Chip* **2007**, *7*, 574.

[79] Veerabadran, N. G.; Goli, P. L.; Stewart-Clark, S. S.; Lvov, Y. M.; Mills, D. K. *Macromol. Biosci.* **2007**, *7*, 877.

[80] Serp, D.; Cantana, E.; Heinzen, C.; von Stockar, U.; Marison, I. W. *Biotechnol. Bioeng.* **2000**, *70*, 41.

[81] Cheong, S. H.; Park, J. K.; Kim, B. S.; Chang, H. N. *Biotechnol. Tech.* **1993**, *7*, 879.

[82] Inloes, D. S.; Smith, W. J.; Taylor, D. P.; Cohen, S. N.; Michaels, A. S.; Robertson, C. R. *Appl. Environ. Microbiol.* **1983**, *46*, 264.

[83] Orive, G.; Gascón, A. R.; Hernández, R. M.; Igartua, M.; Pedraz, J. L. *Trends Pharmacol. Sci.* **2003**, *24*, 207.

[84] Lanza, R. P.; Hayes, J. L.; Chick, W. L. *Nat. Biotechnol.* **1996**, *14*, 1107.

[85] Franzesi, G. T.; Ni, B.; Ling, Y.; Khademhosseini, A. *J. Am. Chem. Soc.* **2006**, *128*, 15064.

[86] Yeh, J.; Ling, Y.; Karp, J. M.; Grantz, J.; Chandawarkar, A.; Eng, G.; 3rd, J. B.; Langer, R.; Pedraz, J. L. *Biomaterials* **2006**, *27*, 5391.

[87] Riley, S. L.; Dutt, S.; Torre, R. D. L.; Chen, A. C.; Ratcliffe, A. *J. Mater. Sci.: Mater. Med.* **2001**, *12*, 983.

[88] Mann, B. K.; Gobin, A. S.; Tsai, A. T.; Schmedlen, R. H.; West, J. L. *Biomaterials* **2001**, *22*, 3045.

[89] Burdick, J. A.; Anseth, K. S. *Biomaterials* **2002**, *23*, 4315.

[90] Nuttelman, C. R.; Tripodi, M. C.; Anseth, K. S. *J. Biomed. Mater. Res., Part A* **2004**, *68*, 773.

[91] Anseth, K. S.; Burdick, J. A. *MRS Bull.* **2002**, *27*, 130.

[92] West, J. L.; Hubbell, J. A. *Biomaterials* **1995**, *16*, 1153.

[93] Revzin, A.; Russell, R. J.; Yadavalli, V. K.; Koh, W. G.; Deister, C.; Hile, D. D.; Mellott, M. B.; Pishko, M. V. *Langmuir* **2001**, *17*, 5440.

[94] Hahn, M. S.; Taite, L. J.; Moon, J. J.; Rowland, M. C.; Ruffino, K. A.; West, J. L. *Biomaterials* **2006**, *27*, 2519.

[95] Williams, C. G.; Malik, A. N.; Kim, T. K.; Manson, P. N.; Elisseeff, J. H. *Biomaterials* **2005**, *26*, 1211.

[96] Dendukuri, D.; Hatton, T. A.; Doyle, P. S. *Langmuir* **2007**, *23*, 4669.

[97] Pregibon, D. C.; Toner, M.; Doyle, P. S. *Science* **2007**, *315*, 1393.

[98] Bryant, S. J.; Nuttelman, C. R.; Anseth, K. S. *J. Biomater. Sci., Polym. Ed.* **2000**, *11*, 439.

[99] White, T. J.; Liechty, W. B.; Guymon, C. A. *J. Polym. Sci., Part A: Polym. Chem.* **2007**, *45*, 4062.

[100] Smeds, K. A.; Pfister-Serres, A.; Miki, D.; Dastgheib, K.; Inoue, M.; Hatchell, D. L.; Grinstaff, M. W. *J. Biomed. Mater. Res.* **2001**, *54*, 115.

[101] Burdick, J. A.; Chung, C.; Jia, X.; Randolph, M. A.; Langer, R. *Biomacromolecules* **2005**, *6*, 386.

[102] Khademhosseini, A.; Bettinger, C.; Karp, J. M.; Yeh, J.; Ling, Y.; Borenstein, J.; Fukuda, J.; Langer, R. *J. Biomater. Sci., Polym. Ed.* **2006**, *17*, 1221.

[103] Bruining, M. J.; Edelbroek-Hoogendoorn, P. S.; Blaauwgeers, H. G.; Mooy, C. M.; Hendrikse, F. H.; Koole, L. H. *J. Biomed. Mater. Res.* **1999**, *47*, 189.

[104] Milam, V. T.; Hiddessen, A. L.; Crocker, J. C.; Graves, D. J.; Hammer, D. A. *Langmuir* **2003**, *19*, 10317.

[105] Soto, C. M.; Srinivasan, A.; Ratna, B. R. *J. Am. Chem. Soc.* **2002**, *124*, 8508.

[106] Valignat, M. P.; Theodoly, O.; Crocker, J. C.; Russel, W. B.; Chaikin, P. M. *Proc. Natl. Acad. Sci., U.S.A* **2005**, *102*, 4225.

[107] Terfort, A.; Bowden, N.; Whitesides, G. M. *Nature* **1997**, *386*, 162.

[108] Bowden, N.; Terfort, A.; Carbeck, J.; Whitesides, G. M. *Science* **1997**, *276*, 233.

[109] Lewis, J. A. *J. Am. Ceram. Soc.* **2000**, *83*, 2341.

[110] Lukasiewicz, S. J. *J. Am. Ceram. Soc.* **1989**, *72*, 617.

[111] Chen, Y.; Au, J.; Kazlas, P.; Ritenour, A.; Gates, H.; McCreary, M. *Nature* **2003**, *423*, 136.

[112] Collins, F. S.; McKusick, V. A. *JAMA J. Am. Med. Assoc.* **2001**, *285*, 540.

[113] York, P.; Marshall, P. V. *Powder Technol.* **1993**, *74*, 171.

[114] Cryer, S. A. *AIChE J.* **1999**, *45*, 2069.

[115] Darelius, A.; Rasmuson, A.; Bjorn, I. N.; Folestad, S. *Powder Technol.* **2005**, *160*, 209.

[116] Stroock, A.; Dertinger, S. K. W.; Ajdari, A.; Mezic, I.; Stone, H. A.; Whitesides, G. M. *Science* **2002**, *295*, 647.

[117] Mundinger, D.; Beach, R.; Benett, W.; Solarz, R.; Krupke, W.; Staver, R.; Tuckerman, D. *Appl. Phys. Lett.* **1988**, *53*, 1030.

[118] Gratson, G. M.; Garcia-Santamaria, F.; Lousse, V.; Xu, M.; Fan, S.; Lewis, J. A.; Braun, P. V. *Adv. Mater.* **1996**, *8*, 461.

[119] Lehmann, O.; Stuke, M. *Science* **1995**, *270*, 1644.

[120] Schuster, R.; Kirchner, V.; Allongue, P.; Ertle, G. *Science* **2000**, *289*, 98.

[121] Desbiens, J. P.; Masson, P. *Sens. Actuators A* **2007**, *136*, 554.

[122] Klajn, R.; Bishop, K. J. M.; Fialkowski, M.; Paszewski, M.; Campbell, C. J.; Gray, T. P.; Grzybowski, B. A. *Science* **2007**, *316*, 261.

[123] Becker, E. W.; Ehrfeld, W.; Hagmann, P.; Maner, A.; Munchmeyer, D. *Microelectron. Eng.* **1986**, *4*, 35.

[124] Hruby, J. *MRS Bull.* **2001**, *26*, 337.

[125] Rao, R. B.; Krafcik, K. L.; Morales, A. M.; Lewis, J. A. *Adv. Mater.* **2005**, *17*, 289.

[126] Liu, Z. Y.; Loh, N. H.; Tor, S. B.; Khor, K. A.; Murakoshi, Y.; Maeda, R.; Shimizu, T. *J. Mater. Process Technol.* **2002**, *127*, 165.

[127] Campbell, C. J.; Smoukov, S. K.; Bishop, K. J. M.; Baker, E.; Grzybowski, B. A. *Adv. Mater.* **2006**, *18*, 2004.

[128] Provin, C.; Monneret, S.; Gall, H. L.; Corbell, S. *Adv. Mater.* **2003**, *15*, 994.

[129] Conrad, P. G.; Nishimura, P. T.; Aherne, D.; Schwartz, B. J.; Wu, D.; Fang, N.; Zhang, X.; Roberts, M. J.; Shea, K. J. *Adv. Mater.* **2003**, *15*, 1541.

[130] Benavides, G. L.; Bieg, L. F.; Saavedra, M. P.; Bryce, E. A. *Microsyst. Technol.* **2002**, *8*, 395.

[131] Seo, M.; Nie, Z.; Xu, S.; Mok, M.; Lewis, P. C.; Graham, R.; Kumacheva, E. *Langmuir* **2005**, *21*, 11614.

[132] Roh, K. H.; Martin, D. C.; Lahan, J. *Nat. Mater.* **2006**, *4*, 759.

[133] Geest, B. D.; Urbanski, J. P.; Thorsen, T.; Demeester, J.; Smedt, S. C. D. *Langmuir* **2005**, *21*, 10275.

[134] Shepherd, R. F.; Conrad, J. C.; Rhodes, S. K.; Link, D. R.; Marquez, M.; Weitz, D. A.; Lewis, J. A. *Langmuir* **2006**, *22*, 8618.

[135] Umbanhowar, P. B.; Prasad, V.; Weitz, D. A. *Langmuir* **2000**, *16*, 347.

[136] Thorsen, T.; Roberts, R. W.; Arnold, F. H.; Quake, S. R. *Phys. Rev. Lett.* **2001**, *86*, 4163.

[137] Sung, K. E.; Vanapalli, S. A.; Mukhija, D.; McKay, H. A.; Millunchick, J. M.; Burns, M. A.; Solomon, M. J. *J. Am. Chem. Soc.* **2008**, *130*, 1335.

[138] Love, C. J.; Wolfe, D. B.; Jacobs, H. O.; Whitesides, G. M. *Langmuir* **2001**, *17*, 6005.

[139] Jang, J.; Dendukuri, D.; Hatton, T. A.; Thomas, E. L.; Doyle, P. S. *Angew. Chem. Int. Ed.* **2007**, *46*, 9027.

[140] Smay, J. E.; Gratson, G. M.; Shepherd, R. F.; Cesarani, J.; Lewis, J. A. *Adv. Mater.* **2002**, *14*, 1279.

[141] Verhaegh, N. A. M.; van Blaaderen, A. *Langmuir* **1994**, *10*, 1427.

[142] Zhao, X. M.; Xia, Y.; Whitesides, G. M. *J. Mater. Chem.* **1997**, *7*, 1069.

[143] Efimenko, K.; Wallace, W. E.; Genzer, J. *J. Colloid Interface Sci.* **2002**, *254*, 306.

[144] Bao, Z.; Weatherspoon, M. R.; Shian, S.; Cai, Y.; Graham, P. D.; Allan, S. M.; Ahmad, G.; Dickerson, M. B.; Church, B. C.; Kang, Z.; Abernathy, H. W.; Summers, C. J.; Liu, M.; Sandhage, K. H. *Nature* **2007**, *446*, 172.

[145] Balagurov, L. A.; Leiferov, B. M.; Petrova, E. A.; Orlov, A. F.; Panasenko, E. M. *J. Appl. Phys.* **1996**, *79*, 7143.

[146] Donev, A.; Cisse, I.; Sachs, D.; Variana, E. A.; Stillinger, F. H.; Connelly, R.; Torquato, S.; Chaikin, P. M. *Science* **2004**, *303*, 990.

[147] Nie, Z.; Li, W.; Seo, M.; Xu, S. Q.; Kumacheva, E. *J. Am. Chem. Soc.* **2006**, *128*, 9408.

[148] Glotzer, S. C. *Science* **2004**, *306*, 419.

[149] Gelloz, B.; Kojima, A.; Koshida, N. *Appl. Phys. Lett.* **2005**, *87*, 031107.

[150] Tas, N.; Sonnenberg, T.; Jansen, H.; Legtenberg, R.; Elwenspoek, M. *J. Micromech. Microeng.* **1996**, *6*, 385.

[151] Lu, Y.; Yin, Y.; Xia, Y. *Adv. Mater.* **2001**, *13*, 415.

[152] Beebe, D. J.; Moore, J. S.; Bauer, J. M.; Yu, Q.; Liu, R. H.; Devadoss, C.; Jo, B. H. *Nature (London)* **2000**, *404*, 588.

[153] Langer, R.; Tirell, D. A. *Nature (London)* **2004**, *428*, 487.

[154] Champion, J. A.; Katare, Y. K.; Mitragotri, S. *Proc. Natl. Acad. Sci. U.S.A.* **2007**, *104*, 11901.

[155] Chen, T.; Zhang, Z.; Glotzer, S. C. *Proc. Natl. Acad. Sci. U.S.A.* **2007**, *104*, 717.

[156] Middleton, G. V. *J. Sediment. Petrol.* **1967**, *327*, 229.

[157] Xia, Y.; Gates, B.; Yin, Y.; Lu, Y. *Adv. Mater.* **2000**, *12*, 693.

[158] Théry, M.; Racine, V.; Piel, M.; Pépin, A.; Dimitrov, A.; Chen, Y.; Sibarita, J. B.; Bornensi, M. *Proc. Natl. Acad. Sci. U.S.A.* **2006**, *103*, 19771.

[159] Graziano, A.; d'Aquino, R.; Gabriella, M.; Angelis, C. D.; Laino, G.; Piattelli, A.; Pacifici, M.; Rosa, A. D.; Papaccio, G. *PLoS ONE* **2007**, *6*, e496.

[160] Champion, J. A.; Mitragotri, S. *Proc. Natl. Acad. Sci. U.S.A.* **2006**, *103*, 4930.

[161] Koepke, P.; Hess, M. *Appl. Opt.* **1988**, *27*, 2422.

[162] Macke, A. *Appl. Opt.* **1993**, *32*, 2780.

[163] *USA Patent* 20070154500.

[164] Mason, T. G.; Ganeshan, K.; vanZanten, J. H.; Wirtz, D.; Kuo, S. C. *Phys. Rev. Lett.* **1997**, *79*, 3282.

[165] van-der Kooij, F. M.; Kassapidou, K.; Lekkerkerker, H. N. W. *Nature (London)* **2000**, *406*, 868.

[166] Badaire, S.; Cottin-Bizonne, C.; Woody, J. W.; Yang, A.; Stroock, A. *J. Am. Chem. Soc.* **2007**, *129*, 40.

[167] Yang, S. M.; Kim, S. H.; Lim, J. M.; Yi, G. R. *J. Mater. Chem.* **2008**, *18*, 2177.

[168] Kim, S. H.; Jeon, S. J.; Yang, S. M. *J. Am. Chem. Soc.* **2008**, *130*, 6040.

[169] Kim, S. H.; Jeon, S. J.; Yi, G. R.; Heo, C. J.; Choi, J. H.; Yang, S. M. *Adv. Mater.* **2008**, *20*, 1649.

[170] Manoharan, V. N.; Pine, D. J. *Mater. Res. Soc. Bull.* **2004**, *29*, 91.

[171] Brown, A. B. D.; Smith, C. G.; Rennie, A. R. *Phys. Rev. E* **2000**, *62*, 951.

[172] Jiang, P.; Bertone, J. F.; Colvin, V. L. *Science* **2001**, *291*, 453.

[173] Sugiura, S.; Nakajima, M.; Tong, J.; Nabetani, H.; Seki, M. *J. Colloid Interface Sci.* **2000**, *227*, 95.

[174] Jeong, W.; Km, J.; Kim, S.; Lee, S.; Mensing, G.; Beebe, D. J. *Lab Chip* **2004**, *4*, 576.

[175] Subramaniam, A. B.; Abkarian, M.; Stone, H. A. *Nat. Mater.* **2005**, *4*, 553.

[176] Nisisako, T.; Torii, T. *Adv. Mater.* **2007**, *19*, 1489.

[177] Panda, P.; Ali, S.; Lo, E.; Chung, B. G.; Hatton, T. A.; Khademhosseini, A.; Doyle, P. S. *Lab Chip* **2008**, *8*, 1056.

[178] Shepherd, R.; Panda, P.; Bao, Z.; Sandhage, K. H.; Hatton, T. A.; Lewis, J. A.; Doyle, P. S. *Adv. Mater.* **2008**, *20*, 4734.

[179] Jeon, S.; Malyarchuk, V.; Rogers, J. A.; Wiederrecht, G. P. *Opt. Express* **2006**, *14*, 2300.

[180] Jang, J. H.; Ullal, C. K.; Kooi, S. E.; Koh, C. Y.; Thomas, E. L. *Nano Lett.* **2007**, *7*, 647.

[181] Decuzzi, P.; Ferrari, M. *Biomaterials* **2006**, *27*, 5307.

[182] Jillavenkatesa, A.; Dapkunas, S. J.; Lum, L. S. H. *Particle Size Characterization; Technical Report 960; National Institute of Standards and Technology (NIST); U.S Government Printing Office: Washington, DC* **2001**,

[183] Yoon, S. K.; Mitchell, M.; Choban, E. R.; Kenis, P. J. A. *Lab Chip* **2005**, *5*, 1259.

[184] Yamaguchi, Y.; Honda, T.; Briones, M. P.; Yamashita, K.; Miyazaki, M.; Nakamura, H.; Maeda, H. *Chem. Eng. Technol.* **2007**, *30*, 379.

[185] Weisstein, E. W. *"Chebyshev Polynomial of the First Kind" can be found under http://mathworld.wolfram.com/ChebyshevPolynomialoftheFirstKind.html* **2008**,

[186] Rabinow, J. *AIEE Trans.* **1948**, *67*, 1308–1315.

[187] Ginder, J. M. *Encyclopedia of Applied Physics* **1996**, *16*, 487–503.

[188] Klingenberg, D. J. *AIChE Journal* **2001**, *47*, 246–249.

[189] Grzelczak, M.; Vermant, J.; Furst, E. M.; Liz-Marzán, L. M. *ACS Nano* **2010**, *4*, 3591–3605.

[190] Kanu, R. C.; Shaw, M. T. *Int. J. Mod. Phys. B* **1996**, *10*, 2925–2932.

[191] Kanu, R. C.; Shaw, M. T. *J. Rheol.* **1998**, *42*, 657–670.

[192] Watanabe, T.; Aoshima, M.; Satoh, A. *J. Colloid Interface Sci.* **2006**, *302*, 347–355.

[193] Tsuda, K.; Takeda, Y.; Ogura, H.; Otsubo, Y. *Colloids Surf. A* **2007**, *299*, 262–267.

[194] Yin, J.; Zhao, X.; Xia, X.; Xiang, L.; Qiao, Y. *Polymer* **2008**, *49*, 4413–4419.

[195] Bell, R. C.; Miller, E. D.; Karli, J. O.; Vavreck, A. N.; Zimmerman, D. T. *Int. J. Mod. Phys. B* **2008**, *21*, 5018–5025.

[196] Bell, R. C.; Karli, J. O.; Vavreck, A. N.; Zimmerman, D. T.; Ngatu, G. T.; Wereley, N. M. *Smart Mater. Struc* **2008**, *17*, 015028.

[197] Ngatu, G. T.; Wereley, N. M.; Karli, J. O.; Bell, R. C. *Smart Mater. Struc* **2008**, *17*, 045022.

[198] de Vicente, J.; Segovia-Gutiérrez, J. P.; A-Reyes, E.; Vereda, F.; H-Álvarez, R. *J. Chem. Phys.* **2009**, *131*, 194902.

[199] de Vicente, J.; Vereda, F.; S-Gutiérrez, J. P.; del P Morales, M.; H-Álvarez, R. *J. Rheol.* **2010**, *54*, 1337–1362.

[200] Ahniyaz, A.; Sakamoto, Y.; Bergstrom, L. *Proc. Natl. Acad. Sci. U. S. A.* **2007**, *104*, 17570–17574.

[201] Lee, S.; Song, Y.; Hosein, I. D.; Liddell, C. M. *J. Mater. Chem.* **2009**, *19*, 350–355.

[202] Ding, T.; Song, K.; Clays, K.; Tung, C. H. *Adv. Mater.* **2009**, *21*, 1936–1940.

[203] Herlihy, K. P.; Nunes, J.; DeSimone, J. M. *Langmuir* **2008**, *24*, 8421–8426.

[204] Isojima, T.; Suh, S. K.; Sande, J. B. V.; Hatton, T. A. *Langmuir* **2009**, *25*, 8292–8298.

[205] Nunes, J.; Herlihy, K. P.; Mair, L.; Superfine, R.; DeSimone, J. M. *Nano Lett.* **2010**, *10*, 1113–1119.

[206] Choi, S. Q.; Jang, S. G.; Pascall, A. J.; Dimitriou, M. D.; Kang, T.; Hawker, C. J.; Squires, T. M. *Adv. Mater.* **2011**, *23*, 2348–2352.

[207] Ge, J.; Hu, Y.; Zhang, T.; Yin, Y. *J. Am. Chem. Soc.* **2007**, *129*, 8974–8975.

[208] Dyab, A. K. F.; Ozmen, M.; Ersoz, M.; Paunov, V. N. *J. Mater. Chem.* **2009**, *19*, 3475–3481.

[209] Yuet, K. P.; Hwang, D. K.; Haghgooie, R.; Doyle, P. S. *Langmuir* **2010**, *26*, 4281–4287.

[210] Gangwal, S.; Cayre, O. J.; Velev, O. D. *Langmuir* **2008**, *24*, 13312–13320.

[211] Gangwal, S.; Pawar, A.; Kretzschmar, I.; Velev, O. D. *Soft Matter* **2010**, *6*, 1413–1418.

[212] Singh, H.; Laibinis, P.; Hatton, T. A. *Langmuir* **2005**, *21*, 11500–11509.

[213] Edwards, B.; Mayer, T. S.; Bhiladvala, R. B. *Nano Lett.* **2006**, *6*, 626–632.

[214] Tierno, P.; Claret, J.; Saguès, F. *Phys. Rev. E* **2009**, *79*, 021501.

[215] Lee, S.; Liddell, C. M. *Small* **2009**, *5*, 1957–1962.

[216] Grzybowski, B.; Whitesides, G. M. *Science* **2002**, *296*, 718–721.

[217] Qi, Y.; Wen, W. *J. Phys. D* **2002**, *35*, 2231–2235.

[218] Teixeira-Pinto, A. A.; Nejelski, L. L.; Cutler, J. L.; Heller, J. H. *Exp. Cell Research* **1960**, *20*, 548–564.

[219] Saito, M.; Schwan, H. P.; Schwarz, G. *J. Biophys.* **1966**, *6*, 313–327.

[220] Yang, M.; Lim, C. C.; Liao, R.; Zhang, X. *J. Microelectromech. Syst.* **2006**, *15*, 1483–1491.

[221] Blakemore, R. P. *Science* **1975**, *190*, 377–379.

[222] Bazylinski, D. A.; Frankel, R. B. *Nature Rev. Microbiol.* **2004**, *2*, 217–230.

[223] Shine, A. D.; Armstrong, R. C. *Rheol. Acta* **1987**, *26*, 152–161.

[224] Panda, P.; Yuet, K. P.; Hatton, T. A.; Doyle, P. S. *Langmuir* **2009**, *25*, 5986.

[225] Panda, P.; Yuet, K. P.; Hatton, T. A.; Doyle, P. S. *New J. Phys.* **2009**, *11*, 115001.

[226] Mohebi, M.; Jamasbi, N.; Liu, J. *Phys. Rev. E* **1996**, *54*, 5407–5413.

[227] Bong, K. W.; Chapin, S. C.; Doyle, P. S. *Langmuir* **2010**, *26*, 8008–8014.

[228] Zallen, R. *The Physics of Amorphous Solids*; John Wiley and Sons, Inc., 1983.